Technical University of Denmark

DTU

Atomic Layer Deposited Catalysts for Fuel Cell Applications

Johansson, Anne-Charlotte Elisabeth Birgitta; Christensen, Leif H. ; Thomsen, Erik Vilain

Link back to DTU Orbit

DTU Library
Technical Information Center of Denmark

PhD Thesis

Atomic Layer Deposited Catalysts for Fuel Cell Applications

Anne-Charlotte Johansson

MEMS-AppliedSensors

Department of Micro- and Nanotechnology

Technical University of Denmark

October 2013

Atomic Layer Deposited Catalysts for Fuel Cell Applications

Anne-Charlotte Johansson

There is only one thing that makes a dream impossible to achieve: the fear of failure.

The Alchemist by Paulo Coelho

Abstract

The micro direct methanol fuel cell (μDMFC) has been proposed as a candidate to power portable applications. The device can operate at room temperature on inexpensive, energy-dense methanol fuel, and it can be easily "recharged" by fuel refilling. Microfabrication techniques could be one route for the realization of such tiny devices. It is a mature technology, suitable for mass production, where versatile structuring is available at the micro and nano regime.

Carbon black supported catalysts synthesized by wet chemistry methods are not readily applicable for standard microfabrication techniques. Atomic layer deposition (ALD), on the other hand, is a highly suitable and still relatively unexplored approach for the synthesis of noble metal catalysts. It is a vapor phase growth method, primarily used to deposit thin films. ALD is based on self-limiting chemical reactions of alternately injected precursors on the sample surface. Its unique growth characteristic enables conformal and uniform films of controlled thickness and composition. In certain conditions ALD commences by island growth, resulting in discrete nanoparticle formation, which is generally preferred for catalytic applications.

Pt-Ru is the best catalyst toward the methanol oxidation reaction (MOR). In the work described in this PhD dissertation, two series of Pt-Ru ALD catalysts supported on nitrogen-doped multi-walled carbon nanotubes (N-CNTs) have been evaluated toward the CO oxidation and MOR at room temperature in a three-electrode electrochemical cell. The first series was comprised of Pt-Ru ALD catalysts of various Ru compositions, between 0 and 100 at.%. For the compositions investigated, the best catalyst had a Ru composition of 29 at.%. In the second series Ru-decorated Pt catalysts of various Ru loadings, i.e., various Ru ALD cycles (1, 2, 5, 10 and 20), were investigated. The Pt nanoparticles decorated with 2 Ru ALD cycles exhibited highest catalytic activity, which also outperformed the best catalyst of the first series.

In addition, a Si-based fuel cell design with ALD catalysts is presented, and its anode was evaluated toward the MOR.

Resumé

Mikro direkte metanol brændselsceller (µDMFC) er blevet foreslåede som en mulig kandidat til at forsyne bærbare applikationer med energi. Enheden kan operere ved stuetemperatur ved brug af metanol der er et billigt og energirigt brændstof, og den kan nemt "genoplades" ved brændstofpåfyldning. En mulig vej til realisering af sådanne små enheder er anvendelse af mikrofabrikationsteknikker. Det er en modern teknologi, der er egnet til masseproduktion, hvor alsidig strukturering er tilgængelig på mikro- og nanoskala.

Carbon black baserede katalysatorer, syntetiseret ved brug af vådkemiske metoder, er ikke umiddelbart anvendelige i forbindelse med standard mikrofabrikationsteknikker. Atomar lag udfældning (ALD) er på den anden side en meget egnet og stadig relativt uudforsket fremgangsmåde til syntese af ædelmetalkatalysatorer. Det er en damp vækstfase metode, der primært anvendes til at deponere tynde film. ALD er baseret på selvbegrænsende kemiske reaktioner af skiftevis injiceret precursors på prøvens overflade. Dens unikke vækst karakteristisk giver konforme og ensartede filmtykkelser og sammensætning. Under visse ALD betingelser forekommer der ø-vækst, hvilket resulterer i dannelse af diskrete nanopartikler, der generelt er foretrukne til katalytiske anvendelser.

Pt-Ru er den bedste katalysator i forbindelse med methanol oxidationssreaktionen (MOR). I denne ph.d.-afhandling er to serier af Pt-Ru ALD katalysatorer, understøttet på kvælstof-dopede multi-væggede carbon nanorør (N-CNTs), blevet evalueret mod CO oxidation og MOR ved stuetemperatur i en tre-elektrode elektrokemisk celle. Den første serie bestod af Pt-Ru ALD katalysatorer af forskellige Ru sammensætninger, mellem 0 og 100 atomar%. For de undersøgte sammensætninger havde den bedste katalysator en Ru sammensætning på 29 atomar%. I den anden serie af Ru-dekorerede Pt nanopartikler anvendtes forskellige Ru sammensætninger, dvs. forskellige Ru ALD cykler (1, 2, 5, 10 og 20). Pt nanopartikler dekoreret med 2 Ru ALD cyklusser udviste den højeste katalytiske aktivitet, og var bedre end den bedste katalysator fra den første række.

Desuden blev der fremstillet et Si-baseret brændselscelledesign med ALD katalysatorer, og anoden blev evalueret mod MOR.

Preface

This PhD dissertation is submitted in partial fulfillment of the requirements for obtaining the PhD degree from the Technical University of Denmark (DTU). It describes the work carried out at the Center for Nano- and Microtechnology at the Danish Technological Institute (DTI) from July 2010 to June 2013. The project has been supervised by PhD Leif H. Christensen, Director of the center at DTI, and Professor Erik V. Thomsen from the Department of Micro- and Nanotechnology at DTU (DTU Nanotech). It was funded by the European Community's Seventh Framework Programme (FP7/2007-2013) under grant agreement number ENHANCE-238409.

First of all, I would like to thank the European Community for the funding, as well as the coordinators and partners. It was a great pleasure to be an ENHANCE fellow. Furthermore, Leif H. Christensen is much appreciated for letting me join the Center for Nano- and Microtechnology and using the lab facilities. He has built up a great center. Erik V. Thomsen is thanked for all valuable feedback and support, and that combined with his positive attitude makes him a great supervisor.

I would like to thank everybody at the Center for Nano- and Microtechnology for being great colleagues and for making every day at work most enjoyable. Those who have been involved in my project are now being specially acknowledged.

Thanks to everybody in the MicroPower project, and especially Jan Hales, Christian Kallesøe and Torsten Lund-Olesen, who were the main persons working on the project when I began at DTI.

Ren Bin Yang had a one year post doc position at DTI, also within the ENHANCE project. I would like to express my sincere thanks to him for all the fun work with ALD and fruitful discussions, as well as for proof-reading the thesis. He is also thanked for showing me around when I visited his home town Kuala Lumpur.

Peter Lund had previously worked at IRD Fuel Cells and brought a lot of knowledge into the center. He is acknowledged for helping me with my electrochemical set-up, and for showing interest in my experiments and progress.

Malmö, July 2013

Anne-Charlotte Johansson

Contents

Chapter 1

Introduction

This PhD project is a contribution to a larger project, called MicroPower, which targeted to develop a micro direct methanol fuel cell (μDMFC) for hearing aid systems. The partners of the MicroPower project were the Center for Nano- and Microtechnology at Danish Technological Institute (DTI), the Department of Micro- and Nanotechnology at Technical University of Denmark (DTU Nanotech), the Department of Chemistry at Århus University (iNANO) and Widex A/S. MicroPower was funded by the Danish National Advanced Technology Foundation. Two fabrication routes were investigated in the project. The first approach was to use conventional components and techniques. The second approach was the application of microfabrication.

Electrocatalysts are essential components in a fuel cell. They are typically synthesized by wet chemistry methods. In this PhD project atomic layer deposition (ALD) was investigated as an alternative and highly suitable synthesis approach for use in a Si-based DMFC. Catalysts were deposited onto nitrogen-doped multi-walled carbon nanotubes (N-CNTs) by ALD, and their catalytic activities were evaluated toward CO oxidation and methanol oxidation reaction (MOR). ALD catalysts were further tested in a novel Si-based DMFC anode, which was prepared using standard microfabrication techniques. In addition, as a side project, Pt was deposited onto two types of cathodes for low temperature (<500 ℃) micro solid oxide fuel cells (μSOFC) by ALD, with the aim of reducing the electrode polarization resistance. The cathodes were fabricated by the Department of Energy and Conversion at DTU.

This chapter introduces ALD, DMFCs and SOFCs, and for each fuel cell type the potential use of ALD is explained. This introduction lays the foundation of the work in the thesis. The chapter concludes with a thesis outline.
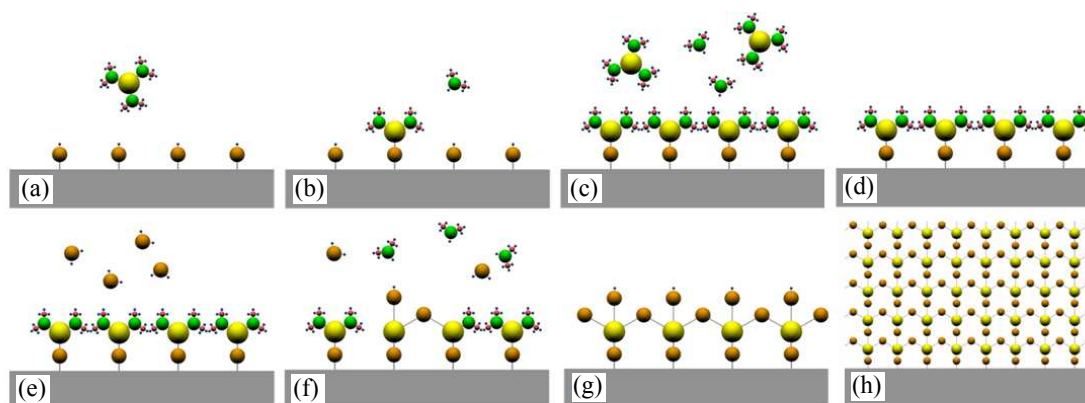
FIGURE 1.1: Illustration of one ALD reaction cycle. (a) Pulse of precursor 1. (b) Reaction at the sample surface. (c) The reaction is self-limiting. (d) Excess precursors and by-products are purged by inert gas. (e) Pulse of precursor 2, e.g., O_2 or H_2O. (f) Reaction at the sample surface. (g) Inert gas purging of excess precursors and by-products. (h) By repeating steps (a)-(g) the ALD film grows layer by layer. Schematic adapted from [2].

1.1 Atomic layer deposition (ALD)

Atomic layer deposition (ALD) is a vapor phase, growth technique, primarily used to deposit thin films. The strength of the method lies in its unique growth process. Typically, two or more highly reactive precursors are pulsed into a reaction chamber sequentially, where they react separately, irreversibly and in a self-limiting manner at the surface without decomposition. The thickness of the film is controlled at the sub-nanometer level by the number of ALD cycles applied.

An example of the reactions occurring during one ALD cycle is illustrated in Fig. 1.1. The ALD cycle starts with the pulsing of precursor 1, Fig. 1.1a, typically a metal reactant, followed by gas-solid reactions (chemisorption) onto the substrate, Fig. 1.1b. The surface is saturated, Fig. 1.1c, and the excess precursors and by-products are removed by inert gas purging, Fig. 1.1d. The second precursor is introduced, Fig. 1.1e, which is typically a non-metal reactant, to react with the ligands of precursor 1, Fig. 1.1f. Again unused precursors and by-products are removed by inert gas purging, Fig. 1.1g. By repeating steps a-g the ALD film grows in a layer-by-layer fashion, Fig. 1.1h. The thickness after one ALD cycle is ideally one monolayer, but in practice it is less due to steric effects. These reactions follow an exchange-type growth mechanism. ALD of Al_2O_3, which is an ALD model system, follows this reaction scheme [1].

There are different growth modes for ALD, illustrated in Fig. 1.2, where growth rate is plotted as a function of deposition temperature. The ALD window is the deposition temperature range where the growth rate is more or less constant. When the growth temperature is too low, precursor condensation or low reactivity of the precursors would
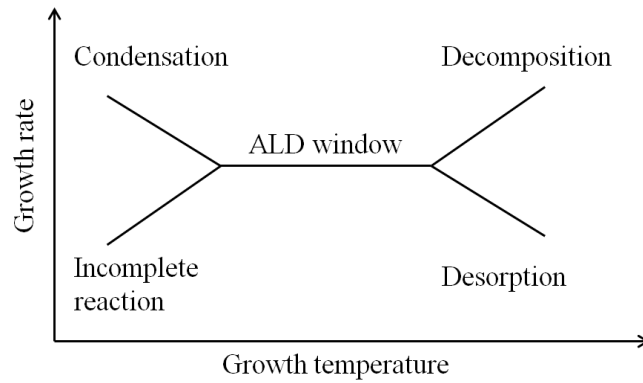
FIGURE 1.2: Illustration of the ALD window, where growth rate is independent of the temperature.
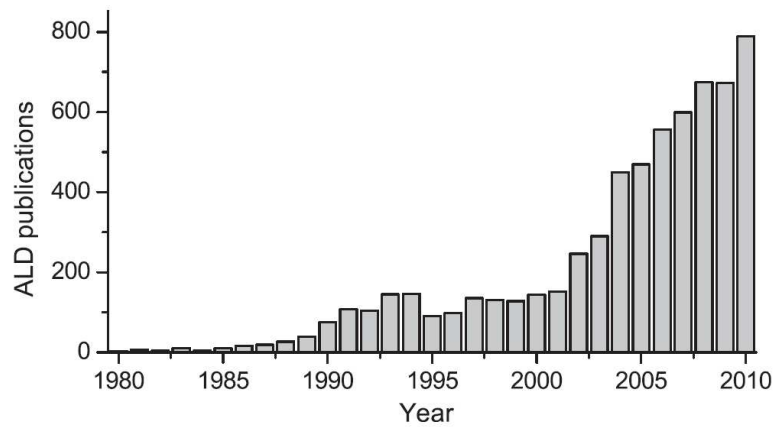
FIGURE 1.3: The number of scientific publications on ALD published per year from 1980 to 2010. Plot taken from [6].

occur. At temperatures above the ALD window, precursor decomposition or precursor desorption might be observed.

Generally, as a result of the self-limiting characteristic, ALD films are conformal, even on high aspect-ratio structures [3]. This is the main feature that distinguishes ALD from other thin film deposition methods. ALD films are typically also of high quality, e.g., pinhole-free, due to the layer-by-layer growth mechanism. In many cases, ALD processes have a relatively low growth temperature with a wide temperature window as the reactions do not rely on decomposition of precursors (like in chemical vapor deposition). High uniformity over large areas, good reproducibility, low vacuum requirements and lack of sensitivity to excess precursors also make ALD suitable for batch production. Due to the digital nature of film growth, i.e., thickness controlled by number of ALD cycles, creating multilayers, mixed, graded or doped layers are also easily achievable, making ALD a flexible deposition technique [4, 5].

One of the most severe limitation of ALD has been the low deposition rate. This is a

problem when thick films need to be grown. However, with the down-scaling of micro-electronic devices and the gradual maturity of thin film applications in nanotechnology research, the time taken to deposit very thin layers have become quite practical. With the recent advances in high speed spatial ALD, even thick films are now obtainable with reasonable processing time [7].

Another major drawback in ALD is the limited choices of available processes for materials (mostly oxides). In the recent decades quite a number of researchers have been developing new precursors and processes to fill the gaps. There is now a good number of ALD processes for metals, nitrides and chalcogenide material systems to choose from [6].

ALD was developed in the 1970s by T. Suntola and coworkers in order to meet the needs of the industry for dense and pinhole-free films in thin film electroluminescent (TFEL) displays. ALD was used in the production already in the early 1980s, but the big breakthrough for the ALD technology came in the beginning of the 21st century. The continuous down-scaling of microelectronic devices was the reason for the growing interest in ALD. The first microelectronic application was in dynamic random-access memory (DRAM) capacitors, where ALD of Al_2O_3 was used as an insulating layer. One of the largest publicities around ALD came when Intel announced that ALD of HfO_2 will be used in the manufacturing of complementary metal-oxide-semiconductor (CMOS) transistors [8]. The diagram in Fig. 1.3 shows the number of ALD publications per year from 1980 to 2010, revealing increasing interests for ALD in many areas of nanotechnology research [9].

1.2   The proton exchange membrane fuel cell (PEMFC)

The proton exchange membrane fuel cell (PEMFC) is distinguished by the use of a polymer electrolyte membrane. The best fuel cell performance is obtained using hydrogen as the fuel, but hydrogen is not easy to handle, store and transport. Methanol can also be used directly as a fuel. Methanol is readily available and is a low-cost liquid fuel. It has a higher energy density compared to hydrogen and is liquid at room temperature [10]. Unfortunately, the direct methanol fuel cell (DMFC) has several downsides, such as methanol crossover from the anode to the cathode and sluggish electrode kinetics, especially the anode, which will be addressed in the next section.
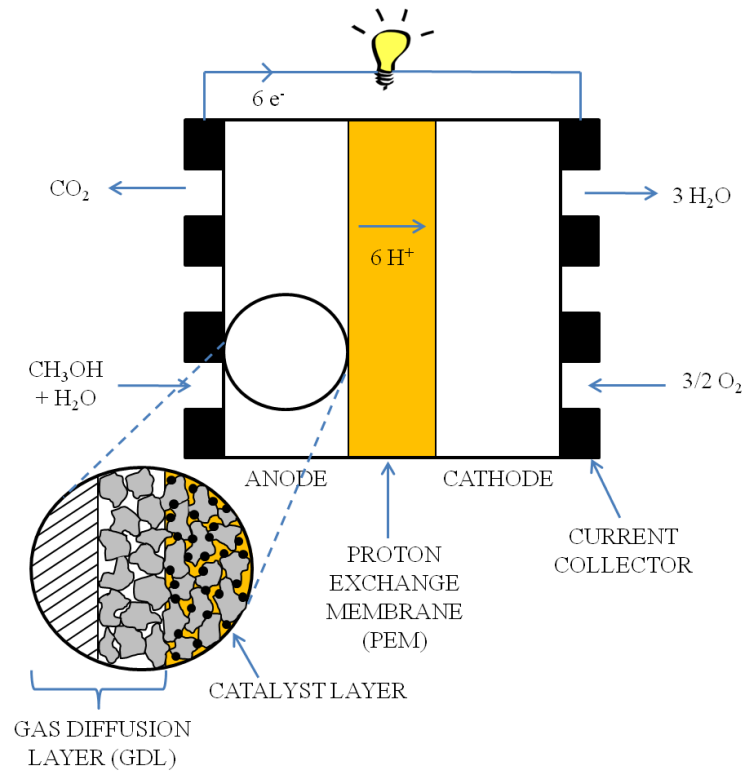
FIGURE 1.4: Schematic of a DMFC.

1.2.1 The direct methanol fuel cell (DMFC)

The principle of the DMFC is shown in Fig. 1.4. The membrane electrode assembly (MEA), the key part of the fuel cell, consists of the anode and cathode, separated by the proton exchange membrane (PEM), and is sandwiched between the current collectors. The anode, as well as the cathode, are made up of the gas diffusion layer and the catalyst layer.

The methanol-water mix enters at the anode, diffuses through the gas diffusion layer (GDL) and is oxidized in the catalyst layer to form protons, electrons and carbon dioxide as the by-product. The complete methanol oxidation reaction (MOR) to carbon dioxide is (1.1):

$$CH_3OH + H_2O \rightarrow 6H^+ + 6e^- + CO_2 \qquad (1.1)$$
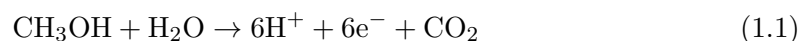
It is a complex reaction, involving six protons and six electrons. The standard electrode potential is 0.016 V, but the overpotential is considerably higher.

The protons are transported through the membrane and the electrons are forced through an external circuit via the current collectors. At the cathode side oxygen is reduced to form water together with the protons and the electrons [10]:

$$3/2O_2 + 6H^+ + 6e^- \rightarrow 3H_2O \tag{1.2}$$

1.2.1.1 The membrane electrode assembly (MEA) in a conventional fuel cell

Proton exchange membrane (PEM)   The proton exchange membrane should have high proton conductivity and be electronically insulating. It must also be able to separate the fuel and the oxidant. However, methanol cross-over is a serious issue in DMFCs, lowering the cell voltage and reducing fuel utilization.

Most commonly used membrane materials today are different sulfonated polymers such as e.g., Nafion (DuPont). Nafion was invented in the 1960s and is still the most well-known membrane in use today. It is comprised of a hydrophobic polytetrafluoroethylene (PTFE) backbone onto which side chains are added, ending with sulfonic acid groups (HSO_3^-). Since sulfonic acid groups are highly hydrophilic, water is adsorbed and protons are conducted within these regions [10].

Catalyst layer   The catalyst layer is made up of nanoparticulate catalysts supported on a large surface area, electronically conductive carbon material. Moreover, Nafion ionomer and PTFE are added in order to control the proton conductivity and hydrophobicity of the layer, respectively. These two components also function as a binder.

The main processes occurring in the catalyst layer include mass transport, interfacial reactions at the electrochemically active sites, proton transport in the electrolyte phase and electron conduction in the electronic phase. There is a three-phase interface between the reactants, electrolyte and electrode, illustrated in Fig. 1.5 for the oxygen reduction. These interfaces are crucial for high utilization of the expensive noble metals.

Important properties of the catalyst layer to be optimized are the reactant diffusivity, ionic and electrical conductivity and the level of hydrophobicity [10].

The state-of-the-art catalysts for the methanol oxidation and oxygen reduction reaction are Pt-Ru and Pt, respectively [11, 12]. These catalysts are typically synthesized by wet chemistry methods [13]. Carbon black, e.g., Vulcan XC-72 and Ketjen Black, is commonly used as the support material for the catalysts in many studies and commercial
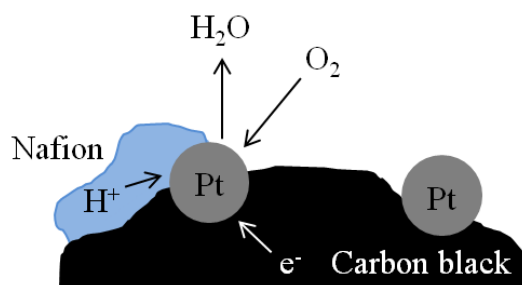
FIGURE 1.5: Illustration of the three-phase contact necessary for electrochemical reaction at the cathode.

applications [14]. Carbon black is cheap, but it suffers from several drawbacks, such as corrosion at the cathode. Furthermore, there is a weak interaction between the catalyst and carbon support, resulting in particle agglomeration and dissolution. In addition, carbon black has small pores, in which catalyst particles can be trapped and get isolated from the reactants and Nafion [13, 15, 16]. A multitude of other materials have therefore been investigated [14, 16], e.g., carbon nanotubes (CNTs). CNTs are candidates to replace carbon black in PEMFCs and DMFCs [17], as they exhibit e.g., excellent electrical conductivity [14] and better corrosion resistance [18–20]. CNTs will be discussed in Chapter 4, along with nitrogen-doped CNTs (N-CNTs), which was the carbon support used in this work.

Gas diffusion layer   The gas diffusion layer (GDL) is usually comprised of a macroporous conducting substrate, such as carbon paper or carbon cloth, and on top a microporous layer of carbon or graphite particles and a hydrophopic agent, usually PTFE, which serves as a binder.

The main function of the GDL is to allow the reactants to enter, as well as the by-products to diffuse away from the catalyst layer. The pore size and hydrophobicity should be optimized to achieve excellent gas/liquid management. It also provides mechanical support and enhances the electronic contact between the carbon-supported catalysts and the current collector [10].

1.2.1.2   The MOR mechanism on Pt-Ru alloy electrocatalysts

Pt-Ru has been extensively studied as it is the best catalyst toward the methanol oxidation reaction (MOR) [11]. The mechanism for such system is explained by two widely accepted models, the bifunctional and the ligand models, first formulated by the group of Watanabe-Motoo [21] and Iwasita-Vielstich [22], illustrated in Fig. 1.6a and b, respectively. Pt is active for dissociative adsorption and dehydrogenation of methanol, but it
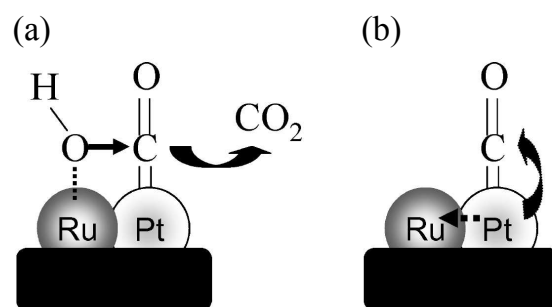
FIGURE 1.6: (a) Illustration of the bifunctional and (b) ligand effect, adapted from [12].

gets poisoned by intermediates, mainly CO as it is the most stable one. For the oxidation of CO molecules, surface-bonded oxygen-containing species are needed. According to the bifunctional mechanism, they are provided by Ru sites at lower potentials than Pt by water dissociation:

$$Ru + H_2O \rightarrow Ru - OH + H^+ + e^- \qquad (1.3)$$
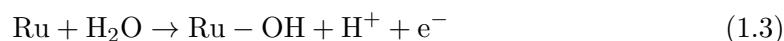
CO can then react with OH:

$$Pt - CO + Ru - OH \rightarrow Pt + Ru + CO_2 + H^+ + e^- \qquad (1.4)$$
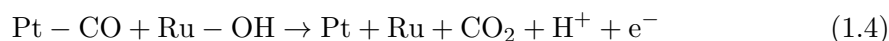
Consequently, the removal of CO is much faster on a Pt-Ru surface than on pure Pt.

The ligand effect is based on the alteration of the electronic structure of Pt. Alloying with Ru produces an increase in Pt d-band vacancies, resulting in a decrease in the Pt-CO bond strength, so that less energy is required to oxidize the surface-bonded CO molecules. This effect is probably of minor importance for the improved performance of the Pt-Ru catalyst [23].

1.2.2 ALD for DMFC applications

ALD is primarily used to deposit thin films. However, in certain circumstances ALD commences by island growth, resulting in discrete nanoparticle formation [34, 35], which is generally preferred for catalytic applications. ALD is a relatively unexplored technique for the synthesis of noble metal catalysts. Over the last few years several Pt and Pt-Ru ALD systems have been evaluated toward electrochemical reactions related to DMFCs, summarized in Table 1.1. Various support materials have been used, including carbon supports (carbon aerogel, graphene and carbon nanotubes), both electronically conducting and insulating oxide supports (silica gel, ZnO nanorods, Al_2O_3 nanospheres

Catalyst	Support	Reaction	Reference
Pt	carbon aerogel	CO ox	[24]
Pt	graphene	CO ox, MOR	[25]
Pt	CNT	ORR	[26]
Pt	silica gel	CO ox	[27]
Pt	ZnO nanorods	MOR	[28]
Pt	$TiSi_2$ nanonet	ORR	[29]
Pt	WC substrate	ORR	[30]
Pt	Ni disk	ORR	[31]
Pt-Ru	Al_2O_3 nanospheres	MOR	[32]
Pt-Ru	FTO glass	CO ox, MOR	[33]

TABLE 1.1: Summary of publications about ALD catalysts for DMFC applications.

and FTO glass), as well as $TiSi_2$ nanonets, WC substrates and Ni disks. Pt and Pt-Ru nucleate as particles onto all above-mentioned materials.

There are only two previous studies dealing with Pt-Ru ALD systems. Jiang et al. [33] reported on the catalytic activity of sputtered Ru films modified with various Pt ALD cycles. The film with the lowest amount of Pt (10 ALD cycles) exhibited the highest MOR activity. In the same paper Pt-Ru ALD films of different compositions were also tested. The film with the highest activity had a stoichiometric Pt:Ru ratio of around 1:1. Christensen et al. [32] deposited Pt-Ru ALD nanoparticles onto alumina nanospheres. The catalysts were comprised of 71 mol% of Ru and had a narrow particle size distribution. They measured the methanol conversion in the temperature range of 190 and 290 ℃ for the ALD deposited catalysts, as well as for a mixture of pure Pt and Ru nanoparticles of similar loading for comparison. The Pt-Ru ALD catalysts showed enhanced methanol conversion, confirming a Pt-Ru bimetallic interaction, which was also suggested by X-ray adsorption spectroscopy.

For ALD onto large quantities of high surface area support materials, special ALD reactors have been developed, i.e., fluidized bed reactors [27, 36, 37] and rotary reactors [38–40]. The up-scaling of the ALD technique has been demonstrated by Zhan et al. [41], who deposited Al_2O_3 particles onto 100 g of single-walled CNTs per batch in a fluidized bed reactor. In the same reactor type, Li et al. [27] deposited well-dispersed Pt nanoparticles onto micron-sized mesoporous silica gel.

1.3 The MicroPower project

There is a growing interest to power portable electronic devices using DMFCs due to the high energy density of methanol and the advantage of instant fuel replenishment (versus

recharging) compared to conventional batteries [42, 43]. The hearing aid is one example of a portable device that could be powered by DMFCs. Hearing aids are essential for a large number of elderly people. For them difficulties arise when an exchange of the small battery in the hearing aid is needed. Methanol-powered hearing aids will be more user-friendly as they allow instant refilling with the fuel cell still attached to the hearing aid. The vision of the MicroPower project was to replace the non-rechargeable zinc-air batteries currently powering hearing aids with DMFCs [44]. The goal was to deliver a power of 2.5 W for 24 h at a voltage above 350 mV on less than 200 µl of methanol. The miniaturization was realized by having a passive supply of reactants, enabling a simple fuel cell system without auxiliary liquid pumps and gas blowers/compressors [45].

Two fuel cell fabrication routes in the MicroPower project have been investigated. The first approach made use of conventional components and techniques described in section 1.2.1.1. The second route for fabrication of such miniature devices was by microfabrication techniques. Compared to the common dry deposition methods such as sputtering and physical vapor deposition (PVD), ALD with its self-limiting character has a lot to offer for catalyst deposition.

Having described the DMFC the attention is now turned toward another type of fuel cell, the solid oxide fuel cell (SOFC).

1.4   SOFC fundamentals

The solid oxide fuel cell (SOFC) is characterized by the use of a solid oxide material as the electrolyte. Fig. 1.7 shows a schematic of a SOFC. The SOFC is comprised of two porous electrodes, separated by a dense, gas-tight electrolyte. The electrodes must conduct electrons and preferably also oxygen ions, whereas the electrolyte should only have high oxygen ion conductivity.

Oxygen gas supplied at the cathode is reduced to oxygen ions. They migrate via the electrolyte to the anode, where the fuel, e.g., H_2 or hydrocarbons, is electrochemically oxidized. This reaction releases electrons, which will travel to the cathode through an external load.

State-of-the-art SOFCs are used for stationary applications in the high power range (several 100 kW to MW) and operate at temperatures from 800 to 1000 ℃. The widespread commercialization of SOFCs has remained elusive, mainly due to the cost and reliability of these devices. Development of intermediate SOFCs, operating at 500-700 ℃, has been one of the main goals in this industry. Cost cutting could be realized as inexpensive metal supports and steel interconnects can be used. Moreover, the life time of the
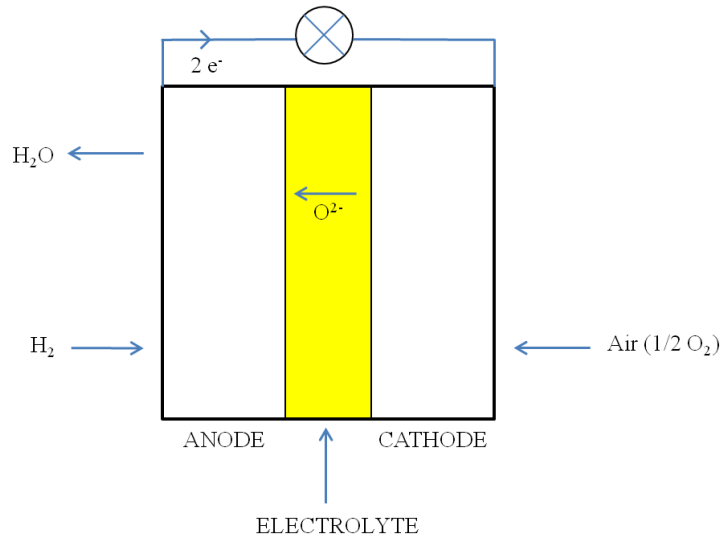
FIGURE 1.7: Schematic of a SOFC, running on H_2.

cell is expected to increase as degradation problems are mitigated. Low-temperature fuel cells operating below 500 ℃ and down to as low as 350 ℃ are promising power sources for portable electronic devices with power requirements of between 1 and 20 W [46, 47]. However, the challenge is in advanced packaging that fulfills complex thermal requirements [47].

1.4.1 ALD for micro SOFC applications

There are accompanying disadvantages with lower operating temperature for SOFCs, such as reduced oxygen ion conductivity. However, it could be compensated by using a thin electrolyte. Ultrathin, pin-hole free films can be deposited by ALD and is therefore an ideal technique for this application [48, 49]. Furthermore, the electrode kinetics are affected. Up to now there is little research about ALD deposited electrode materials. Holme et al. [50] deposited $La_xSr_{1-x}MnO_3$ (LSM) by ALD onto an electrolyte, yttria-stabilized zirconia (YSZ). The cathode was tested at 450 ℃, but unfortunately it exhibited low power density.

Platinum has superior catalytic activity at lower temperatures compared to ceramics [51]. Friedrich B. Prinz' group from Stanford University has investigated ALD of Pt as electrodes in low-temperature SOFCs [51–55]. The research group has shown that by using ALD as the catalyst deposition technique, the amount of expensive catalysts could be reduced significantly compared to using sputtering, while achieving comparable maximum power densities [52].

In most of the aforementioned work Pt is deposited directly onto YSZ. Here the effect of adding a little amount of Pt by ALD onto various ceramic cathodes was investigated.

1.5   Outline

The dissertation is divided into eight chapters and one appendix. In the following an outline of the remainder of the thesis is given.

- **Chapter 2:** Electrochemical Characterization. This chapter describes the electrochemical set-ups and procedures applied in Chapters 4, 5, 6 and 7.

- **Chapter 3:** Atomic Layer Deposition of Platinum and Ruthenium. The Pt and Ru processes have been established and the results are presented in this chapter.

- **Chapter 4:** Pt-Ru Catalysts on N-CNTs by ALD. Nitrogen-doped carbon nanotubes (N-CNTs) are introduced, followed by a nucleation study of Pt and Ru onto the carbon support. The rest of the chapter is dedicated to results about the Pt-Ru/N-CNT catalysts of various compositions.

- **Chapter 5:** Ru-Decorated Pt Catalysts on N-CNTs by ALD. The second catalyst series about Pt nanoparticles decorated with various ALD cycles of Ru. The best catalyst from the two series is compared with a commercial Pt-Ru catalyst (HiSPEC 12100, Johnson Matthey Fuel Cell).

- **Chapter 6:** ALD Catalysts for Si-Based DMFC Applications. A Si-based fuel cell design is presented and the anode with ALD deposited catalysts is evaluated toward the MOR.

- **Chapter 7:** ALD of Pt on Cathodes for Low Temperature SOFCs. Two types of cathodes with added Pt were characterized using electrochemical impedance spectroscopy (EIS).

- **Chapter 8:** Conclusion and Outlook. The most important results are stated with suggestions for future work.

- **Appendix A:** List of Dissemination. Journal publications, talks and posters, as well as all activities within the EU-project ENHANCE are listed here.

Chapter 2

Electrochemical Characterization

For catalyst evaluation electrochemical methods were applied in this PhD project, together with other techniques such as scanning electron microscopy (SEM), transmission electron microscopy (TEM), X-ray photoelectron spectroscopy (XPS) and X-ray diffraction (XRD). This chapter is dedicated only to electrochemical methods. The catalysts for direct methanol fuel cells (DMFCs) were characterized in a three-electrode electrochemical set-up, whereas the solid oxide fuel cell (SOFC) cathodes were characterized using electrochemical impedance spectroscopy (EIS).

2.1 The three-electrode electrochemical set-up

A three-electrode electrochemical set-up was built, Fig. 2.1, consisting of N_2 (99.999%, AGA) and 5% CO in Ar (99%, AGA) gas bottles, mass flow controllers (MFCs), CO sensor and a custom-made glass cell with three electrodes, placed in a fume hood. A potentiostat (Gamry Instruments, Reference 600) was used to control the electrodes, monitored by computer.

A photo of the electrodes inserted in the glass cell is shown in Fig. 2.2. The catalysts to be measured were deposited onto a glassy carbon electrode (PINE Instruments), functioning as the working electrode (WE). A platinum disk was used as the counter electrode (CE) and a K_2SO_4-saturated Hg/Hg_2SO_4 electrode (Radiometer analytical) served as the reference electrode (RE). The potentials in this thesis are quoted in reference to the normal hydrogen electrode (NHE) (unless otherwise stated).

The electrolytes 0.5 M H_2SO_4 and 1.0 M CH_3OH + 0.5 M H_2SO_4 were prepared from 96% H_2SO_4 (Suprapur, Merck), CH_3OH (TraceSELECT, Fluka Analytical) and Millipore water (18 MΩ·cm). All solutions were degassed with N_2 before and during the
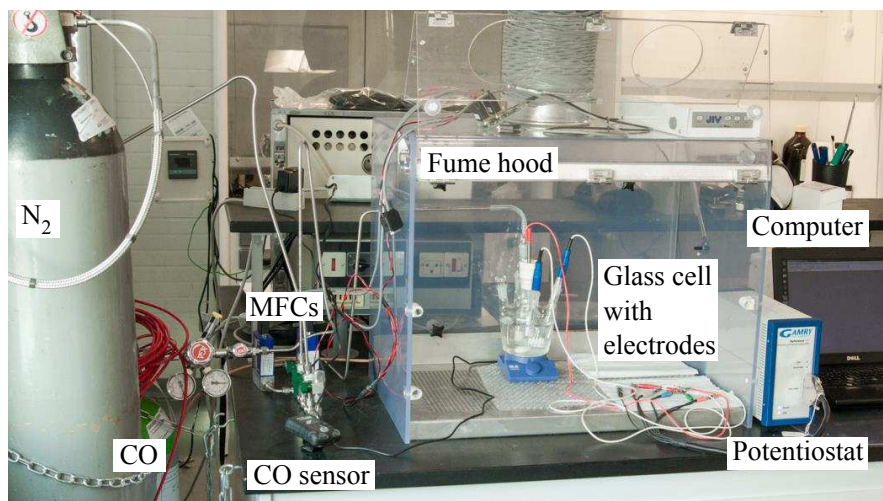
FIGURE 2.1: The three-electrode electrochemical set-up, made-up of N_2 and CO gas bottles, MFCs, CO sensor, custom-made glass cell with electrodes placed in a fume hood, potentiostat and computer.
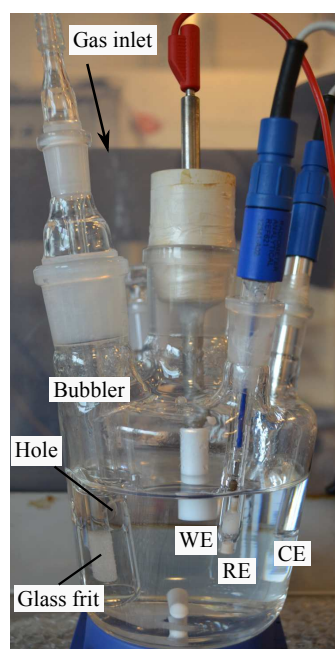
FIGURE 2.2: Custom-made glass cell with working electrode (WE), counter electrode (CE), reference electrode (RE) and bubbler system. The arrow shows the direction of the gas inlet.

measurements in order to exclude reactions with dissolved oxygen. A special bubbling apparatus was designed, see Fig. 2.2, in order to prevent gas bubbles from travelling to the WE, and blocking reaction sites during measurements. N_2 gas was flowed through the central tube with a porous glass frit at the end. This tube was surrounded by another glass tube with three holes, confining the bubbles as they go up to the surface of the electrolyte. In addition, the electrolyte was circulated via the three holes, and the bubbling apparatus was found to be effective in removing dissolved oxygen.

2.2 Cyclic voltammetry

Cyclic voltammetry (CV) is a type of potentiodynamic electrochemical measurement and is generally used to investigate the basic characteristic of the studied system. The potential is swept at a certain scan rate from one potential limit to the other and back. The low potential limit is often the potential for hydrogen evolution whereas the high potential limit is not more than the potential for oxygen evolution. During the sweep, the current at the working electrode is continuously measured. The current is plotted versus the applied potential to give the cyclic voltammogram. There are two types of responses to the applied potential sweep. Capacitive current is due to charging/discharging of the electrochemical double layer capacitance by accumulation/removal of electrical charges on the electrode and in the electrolyte solution near the electrode. The capacitive current is generally zero when the potential is constant. Faradaic current (charge transfer) is related to chemical reactions occurring at the electrode surface.

CV was applied to characterize the catalysts in both 0.5 M H_2SO_4 and 1.0 M CH_3OH + 0.5 M H_2SO_4 solutions.

CV in H_2SO_4

Fig. 2.3a shows a typical cyclic voltammogram of Pt catalysts (HiSPEC 13100, Johnson Matthey Fuel Cells), recorded in 0.5 M H_2SO_4 at a scan rate of 20 mV/s. In the absence of methanol active species, the observed current-potential behavior is only determined by the formation and dissolution of hydrogen ad-layers and oxygen ad-layers on the surface of the catalyst. The plot is divided into three potential regions, labeled I, II and III in the figure. Region I is the so-called hydrogen underpotential deposition (H_{upd}) region. Hydrogen is adsorbed during the cathodic potential sweep near 0 V vs. the reversible hydrogen electrode (RHE), by the charge-transfer reaction step, called the Volmer reaction:

$$H^+ + e^- \rightarrow H_{ads} \tag{2.1}$$

Hydrogen gas is evolved at 0 V vs. RHE via the Tafel, Eq. 2.2, or the Heyrovsky, Eq. 2.3, reaction step [56, 57]:

$$2H_{ads} \rightarrow H_2 \tag{2.2}$$
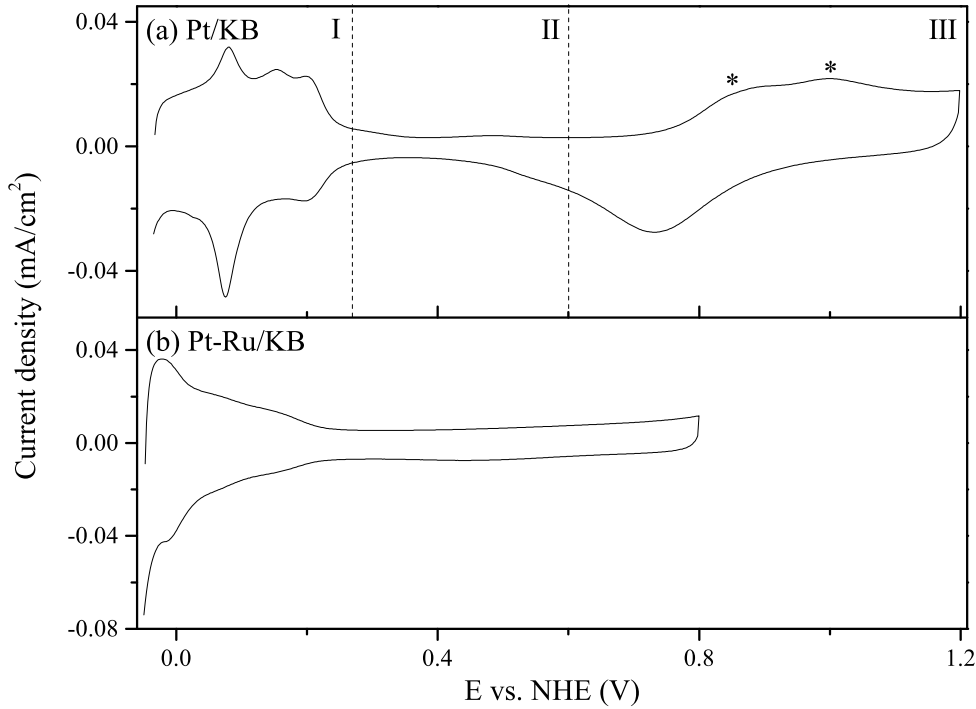
FIGURE 2.3: CVs of (a) Pt/KB (HiSPEC 13100, Johnson Matthey Fuel Cells) and (b) Pt-Ru/KB (HiSPEC 12100, Johnson Matthey Fuel Cells) obtained in 0.5 M H_2SO_4 at a scan rate of 20 mV/s. The CV in (a) is divided into three characteristic regions. I: Hydrogen underpotential deposition region, II: double layer region and III: oxide formation/reduction region.

$$H_{ads} + H^+ + e^- \rightarrow H_2 \tag{2.3}$$

The hydrogen desorption peaks are present in the anodic scan. The well-defined peaks are due to the presence of different Pt crystalline facets [58]. Moreover, the stronger the Pt-H bond the higher in potential the peaks are located.

The double layer charging/discharging region II ranges from around 0.3 to 0.6 V. Region III is the oxidation/reduction region. In the anodic (forward) direction two peaks are observed, each marked by a star. The consecutive reactions that occur are the formation of OH and O on the Pt surface [58], Eq. 2.4 and Eq. 2.5, respectively. Pt catalyzes water dissociation, and an oxide layer is formed:

$$H_2O \rightarrow OH_{ads} + H^+ + e^- \tag{2.4}$$

$$OH_{ads} \rightarrow O_{ads} + H^+ + e^- \tag{2.5}$$
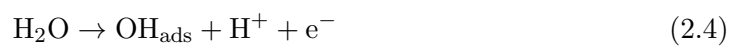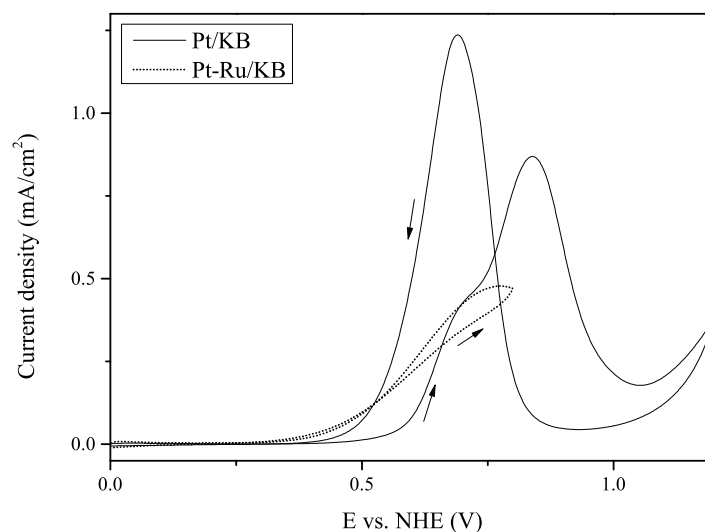
FIGURE 2.4: CVs of (a) Pt/KB and (b) Pt-Ru/KB obtained in 1.0 M CH$_3$OH + 0.5 M H$_2$SO$_4$ at a scan rate of 10 mV/s. 1st cycle is plotted. The arrows mark the potential scan direction.

Beyond these two peaks the oxygen gas evolution starts to dominate (not seen in this CV). In the cathodic direction the measured peak is related to the reduction of the oxide layer.

Let us compare the CV of Pt/KB with the CV of Pt-Ru/KB (HiSPEC 12100, Johnson Matthey Fuel Cells) in Fig. 2.3b, which was also obtained in 0.5 M H$_2$SO$_4$ at 20 mV/s. The peaks in the H$_{upd}$ region are less pronounced for two reasons. Ru is significantly less active than Pt for H adsorption/desorption [59] and Ru oxide formation commences at around 0.2 V [12]. As a consequence of the latter, the double layer region is typically also wider than that for the Pt catalyst.

The onset of Ru dissolution from pure Ru is at 0.9 V vs. RHE, and maybe lower for alloys [60]. Therefore, in order not to avoid surface composition modification of the catalysts, the high potential limit for Pt-Ru was therefore set to 0.8 V.

CV in CH$_3$OH

Fig. 2.4 shows CVs of same catalysts, Pt/KB and Pt-Ru/KB, obtained in methanol-containing electrolyte (1.0 M CH$_3$OH + 0.5 M H$_2$SO$_4$) at 10 mV/s and the 1st cycle is plotted. The arrows mark the scan direction. In Chapter 1 the MOR mechanism was described, and here it is illustrated using the CVs. For the Pt/KB, one peak is measured in the forward and one in the reverse scan. Methanol molecules are not able to displace

adsorbed H atoms, meaning methanol adsorption begins at potentials where enough Pt sites become free from H. For a polycrystalline Pt electrode it is around 0.2 V vs. RHE. Pt is a good catalyst for breaking the C-H bonds. However, the Pt surface gets poisoned by mainly CO, and the presence of oxide species are therefore needed for CO oxidation. On the Pt electrode, sufficient interaction with water is only possible at potentials above 0.4-0.5 V vs. RHE, meaning CO cannot be oxidized below that potential. Upon sweeping to higher potentials more Pt sites get oxidized, resulting in a reduced methanol oxidation rate, giving rise to the peak. At the anodic limit no intermediate species are left on the surface of the catalyst, which is fully oxidized. During the reverse scan the oxide layer must be partially removed before oxidation of new methanol molecules, explaining the observed peak potential shift.

In the case for the Pt-Ru/KB it is clear that the onset potential for methanol oxidation commences at much lower potentials as Ru is oxidized already at 0.2 V, providing oxygenated species for CO oxidation.

The catalysts in this project were evaluated by comparing the anodic sweep of the first cycle.

2.3   Chronoamperometry

The steady state behavior of the catalysts at a specific potential is determined using chronoamperometry [61]. The potential is held at a fix value and the current response is recorded. The chosen potential in this thesis was 0.4 V, which is the potential of technological interest in a fuel cell [12].

2.4   Determination of the electrochemically active surface area (ECSA)

The electrochemically active surface area (ECSA) is needed for the calculation of the specific activity. It can be estimated from the amount of charge it takes to either adsorb or desorb a layer of hydrogen in the H_{upd} region in a CV. The area under either peaks is calculated and corrected for the current associated with the double layer charging/discharging by a straight line [62]. The area is divided by the scan rate to obtain the charge. The ECSA is then estimated by dividing the charge by 210 $\mu C/cm^2$, which is the charge density required to adsorb or desorb a monolayer of hydrogen onto a polycrystalline Pt surface [58].
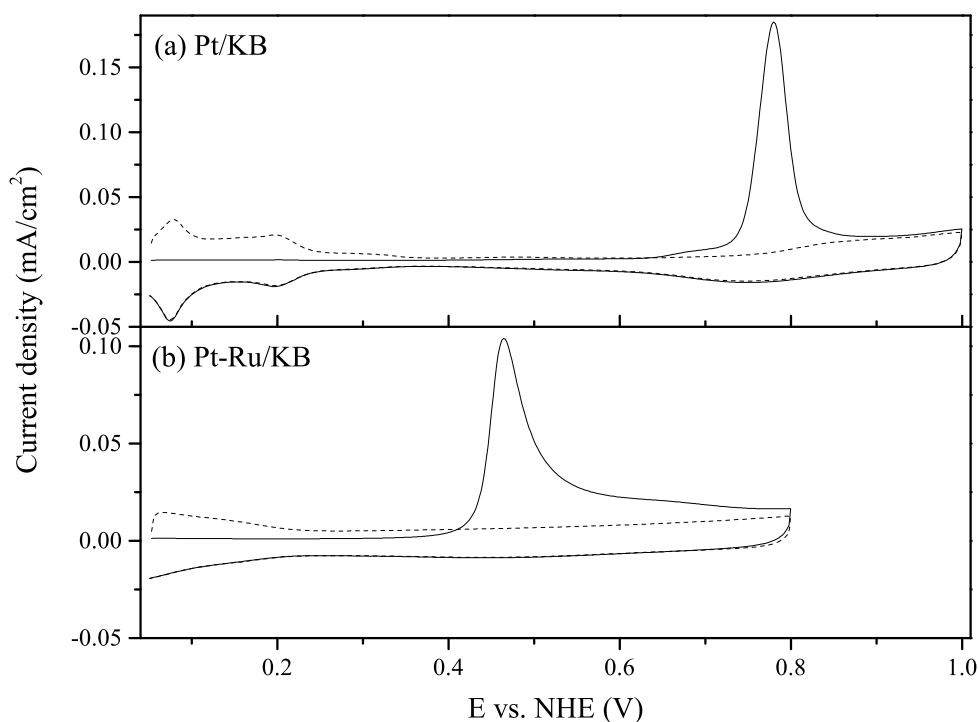
FIGURE 2.5: CO-stripping of (a) Pt/KB and (b) Pt-Ru/KB in 0.5 M H_2SO_4 at 20 mV/s after adsorption of CO at 50 mV. The solid and the dashed lines are the first and the second cycles, respectively.

Determination of the ECSA from the H_{upd} region is not suitable for Pt-Ru catalysts due to the overlap of the H_{upd} region and Ru oxide formation. However, the ECSA can also be estimated from the amount of charge related to the oxidation of a pre-adsorbed monolayer of CO in a stripping. CO is adsorbed onto the catalyst under potential control by bubbling the electrolyte with CO, followed by purging with N_2 to remove any residual CO from the solution before the CO-stripping.

CO-stripping voltammogram for Pt/KB are plotted in Fig. 2.5a and that for Pt-Ru/KB in Fig. 2.5b. The straight and the dashed lines are the first and the second cycles, respectively. The suppression of the pseudo-capacitive current during the first forward sweep indicates that the electrode surface is saturated with CO molecules [60]. The anodic peak corresponds to the irreversible, oxidative stripping of the adsorbed CO monolayer. As discussed in Chapter 1, CO oxidation is shifted to lower potentials for Pt-Ru catalysts, which is also clearly seen by comparing Fig. 2.5a and Fig. 2.5b.

For calculation of the ECSA, the area under the CO oxidation peak is used, with the second cycle as the baseline in order to correct for double layer charging and oxide formation. The current density value is 420 μC/cm^2, which represents the charge density required to oxidize a monolayer of CO from a polycrystalline surface of Pt (assuming

linear CO adsorption configuration [58, 63]). The charge density is twice that for the H adsorption/desorption case since two electrons are involved in the removal of one CO molecule, see Eq. 1.3 and Eq. 1.4, whereas only one electron is involved for each H molecule, see Eq. 2.1.

2.5 Catalyst durability

Degradation of the electrocatalyst and carbon support is one of the main factors that decrease the life time of the fuel cell [20]. It is associated with the loss of ECSA. There are various catalyst degradation processes as a consequence of weak adhesion to the carbon support. The decrease in ECSA may result from the increase in catalyst particle size by Ostwald ripening (catalyst dissolution and redeposition) or Pt agglomeration on the carbon support upon Pt migration. Other degradation mechanisms could be dissolution of catalyst material into the electrolyte or detachment of nanoparticles from the carbon support upon corrosion [20, 64, 65].

2.5.1 Accelerated degradation test

The aim of an accelerated degradation test (ADT) is to simulate the long-term behavior of fuel cell electrocatalysts. This can be performed by cyclic voltammetry. There are two voltage cycling regimes, called lifetime and start-up testing. Hasche et al. [66] performed lifetime testing between 0.5 and 1.0 V vs. RHE at 50 mV/s for 10000 cycles. The second ADT was conducted between 0.5 and 1.5 V vs. RHE at 50 mV/s for 2000 cycles. In this thesis the durability test was performed by scanning between 0.6 and 1.2 V at 50 mV/s for 2000 cycles.

2.6 Set-up for electrochemical impedance spectroscopy (EIS)

Electrochemical impedance spectroscopy (EIS) was performed on various symmetric solid oxide fuel cell (SOFC) cathodes. A schematic of the measurement set-up is shown in Fig. 2.6. The sample was clamped between two alumina holders. For current collection, Pt paste (Ferro GmbH, Germany) painted onto both sides of the symmetric cell, and a Pt mesh on both sides were used. This was placed in an alumina tube, which in turn was placed in a furnace.
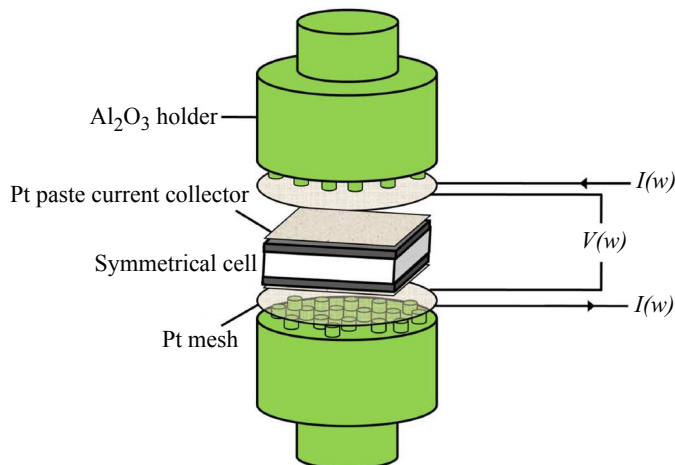
FIGURE 2.6: Schematic of the measurement set-up for EIS, adapted from [67].
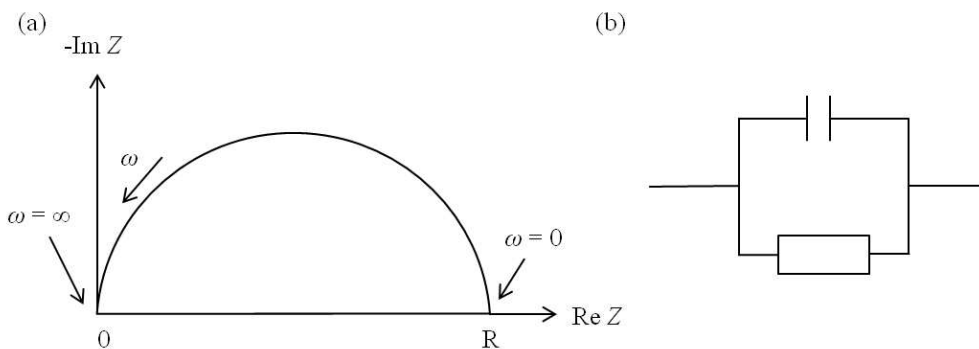
FIGURE 2.7: (a) Example of a Nyquist plot and (b) its equivalent electrical circuit.

2.7 EIS

There are two operating modes in EIS, called potentiostatic and galvanostatic. In potentiostatic mode a low-amplitude, alternating potential is applied to the electrochemical cell and the current response is measured. For galvanostatic mode, the opposite is being done: perturbation is made to the current while the potential is monitored [68]. By applying a small excitation signal the response is pseudo-linear and expressed by a magnitude and a phase shift. The impedance Z can be calculated and plotted in a so-called Nyquist plot, with the real part of the impedance on the x-axis and its imaginary part on the y-axis. An example is shown in Fig. 2.7a. Each point on the complex plane plot is the impedance at one frequency ω.

EIS data is commonly analyzed by fitting it to an equivalent electrical circuit model as each physical process in the electrochemical cell, e.g., electrolyte resistance and polarization resistance, has characteristic impedance behavior and can be considered as an electric component or a simple electrical circuit. The model can be a combination of resistances, capacitances, and/or inductances, as well as a few specialized electrochemical

elements such as Warburg diffusion elements and constant phase elements. It produces the same response as the electrochemical system does when the excitation signal is applied. The Nyquist plot in Fig. 2.7a is described by a resistor and capacitor in parallel, Fig. 2.7b.

Chapter 3

Atomic Layer Deposition of Platinum and Ruthenium

This chapter covers the ALD processes for Pt and Ru. The chosen precursors that were used and the reaction mechanism of Pt and Ru will be discussed, followed by an introduction to the ALD system. The rest of the chapter is about the Pt and Ru ALD processes. A major part of the results has been published in [69]. The study concerns the definition of the ALD window and optimization of the pulse time of the noble metal precursors. The morphology, purity and crystalline phases of the films were characterized. In addition, Pt nucleation onto SiO_2 was investigated.

3.1 Precursors for ALD of Pt and Ru

A successful ALD process relies on the underlying chemistry and the precursors have many requirements - some will be mentioned here. First of all, the precursors must be gaseous or vaporizable at a temperature lower than the deposition temperature. They should also be thermally stable, i.e., do not decompose during storage, at the vaporization temperature nor at the ALD growth temperature or react on itself. They should react, preferable fast, complete and aggressively, in a saturating, irreversible manner with the sites on the surface of the growth substrate. The by-products should be inert. Also sufficient reactivity toward the other precursor is necessary.

ALD processes for platinum and ruthenium were first studied by Aaltonen et al. [70–74]. Since then, other groups have also investigated these processes and they are listed in [6]. In this work trimethyl(methylcyclopentadienyl)platinum (MeCpPtMe$_3$), Fig. 3.1a, and bis(ethylcyclopentadienyl)ruthenium Ru(EtCp)$_2$, Fig. 3.1b, was used as the noble
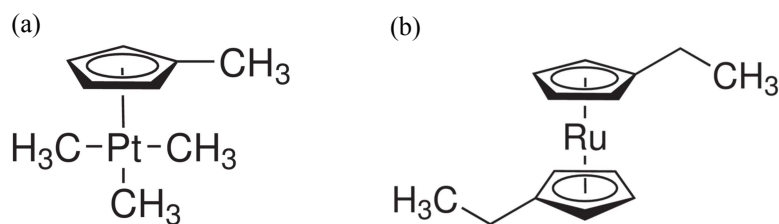
FIGURE 3.1: Molecule structure of (a) trimethyl(methylcyclopentadienyl)platinum (MeCpPtMe$_3$) and (b) bis(ethylcyclopentadienyl)ruthenium (Ru(EtCp)$_2$).

metal source, and oxygen as the reactant in both processes. The metal precursors were commercially available and purchased from Sigma Aldrich. The melting temperature of the Pt and Ru precursors were 30-31 ℃ and 6 ℃, respectively. To facilitate loading into the precursor bottles, the Pt compound was heated a few degrees above its melting temperature to make sure it was in a liquid state. Both compounds were found to be stable enough for handling in air for short durations.

3.1.1 Reaction mechanism in ALD of Pt and Ru

The reaction mechanism in ALD of Pt and Ru differs from the exchange-type approach described in Chapter 1, typically used to explain the reactions during one ALD cycle. Aaltonen et al. studied *in situ* the reaction mechanism in ALD of Pt and Ru using a quartz crystal microbalance (QCM) and quadrupole mass spectroscopy (QMS) [71]. The ligands of the metal precursors were eliminated through combustion-like reactions, indicated by the formation of CO_2 and H_2O reaction by-products. It was measured that they were released during both the metal precursor and O_2 pulses, implying that O_2 is adsorbed onto the Pt surface after oxidation of the hydrocarbon ligands and that O_2 oxidizes the ligands in the following metal pulse.

Kessels et al. [75] used infrared spectroscopy to further study the reaction mechanism of Pt ALD. Apart from CO_2 and H_2O they also detected CH_4 as a reaction by-product in the metal precursor pulse, suggesting that not all ligands were removed by combustion reactions.

In none of the studies the catalytic nature of Pt was taken fully into account. Considering that, Mackus et al. [76] concluded that in addition to the combustion reactions during the Pt precursor pulse, the precursor ligands undergo dehydrogenation on the Pt surface as well as hydrogenation of methyl ligands with hydrogen from the dehydrogenation reactions, forming H_2 and CH_4, respectively.

The reaction mechanism studies mentioned above were performed on noble metal surfaces. The initiation of growth on other types of substrates is discussed in [6] for Ru.
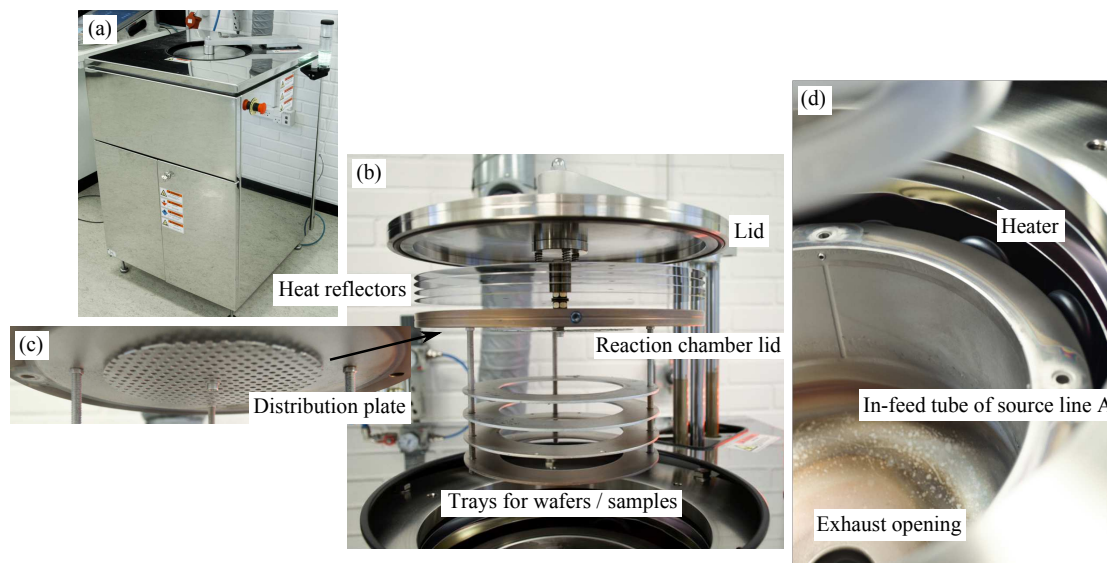
FIGURE 3.2: (a) The ALD reactor (Picosun Sunale R-150). (b) Picture of the top part of the ALD, shot with reactor lid opened, showing the heat reflectors, reaction chamber lid, distribution plate and trays for wafers/samples. (c) Close-up photo of the reaction chamber lid and distribution plate. (d) Photo of the reaction chamber, surrounded by the heater. The in-feed tube of source line A and exhaust opening can also be seen.

Nucleation delays are often observed. This will be discussed in Chapter 4, in connection with the results about ALD catalyst particles on carbon nanotubes.

3.2 ALD reactor

Pt and Ru were deposited using a hot-wall, top-flow ALD reactor from Picosun (Sunale R-150, Fig. 3.2a). Fig. 3.2b is a photo of the top part of the reactor, shot with lid opened. Besides the lid, heat reflectors, reaction chamber lid, precursor distribution plate (Fig. 3.2c) and four trays for four 4" wafers or samples in total can be seen. Fig. 3.2d is a picture of the reaction chamber. It is surrounded by the heater, placed in the intermediate space, separating the reaction chamber wall and outer wall (not to be seen in the photo).

Fig. 3.3 is a schematic of the ALD system. The temperature of the reaction chamber was measured with the thermoelement TE2. Usually during the deposition process the heater temperature, measured by thermoelement TE1, was about 70-110 °C higher than the stabilized reaction chamber temperature. The intermediate space was purged with N_2 and the mass flow rate was set by MFC1. The pressure of the intermediate space, measured by PT1, was typically 5-15 hPa during a deposition process. The pressure was depended on the deposition temperature and gas flow rate going through MFC1,
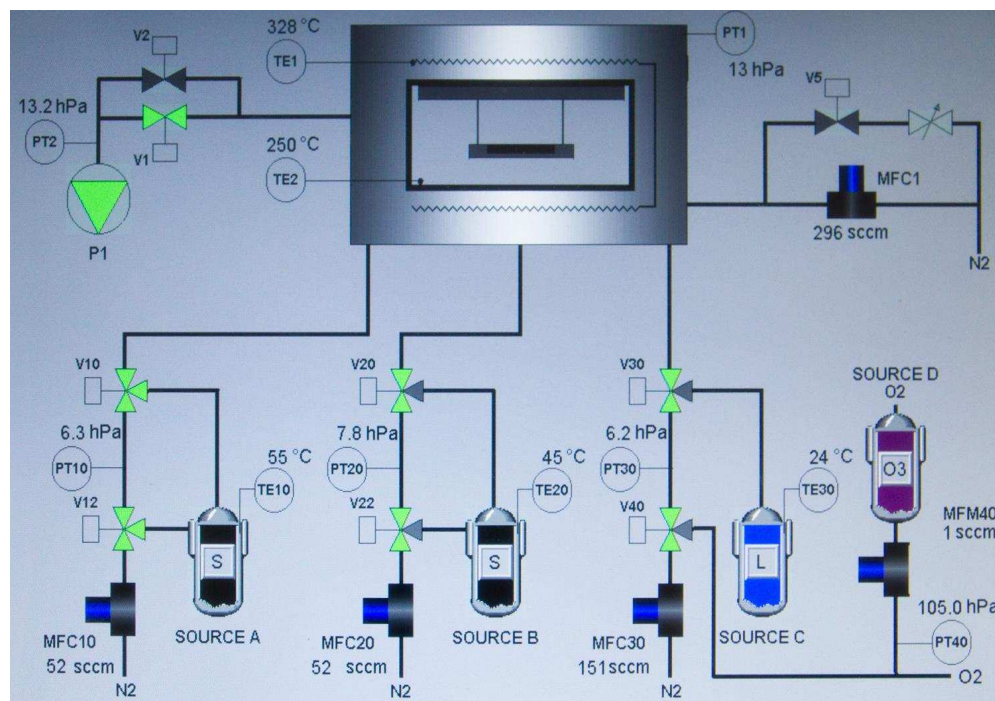
FIGURE 3.3: Schematic of the ALD system.

which was 300 sccm throughout all depositions. There was no pressure transducer in the reaction chamber.

There was room for four precursors in total in the ALD system (source A, B, C and D). In this project three precursors were used in total. The platinum precursor, ruthenium precursor and oxygen gas were supplied from source A, B, and D, respectively. Source A and B were equipped with a Picosolid Booster source system and the temperature of each could be set and measured by the thermoelements TE10 and TE20. For the depositions in this chapter, the temperature of the Pt and Ru precursor was set to 55 ℃ and 80 ℃, respectively.

The precursor gas lines were purged with N_2, functioning as the precursor vapor carrier. The gas flow rate for source A, B and C/D is set by MFC10, MFC20 and MFC30, respectively. The N_2 flow rate was set to 50 sccm for source A and B, and 150 sccm for source C/D for all depositions. The oxygen gas flow rate was controlled by a valve and adjusted to give a pressure of 20 hPa during pulsing, read out by the pressure transducer PT30.

The photo in Fig. 3.3 is captured during the Pt precursor (source A) pulse. The three-way pneumatic valves V12 and V10 were opened, allowing N_2 into the precursor source container and letting out the gas mixture of N_2 and precursor vapor to the reaction chamber. The gas mixture was delivered through the in-feed tube (shown in Fig. 3.2d)
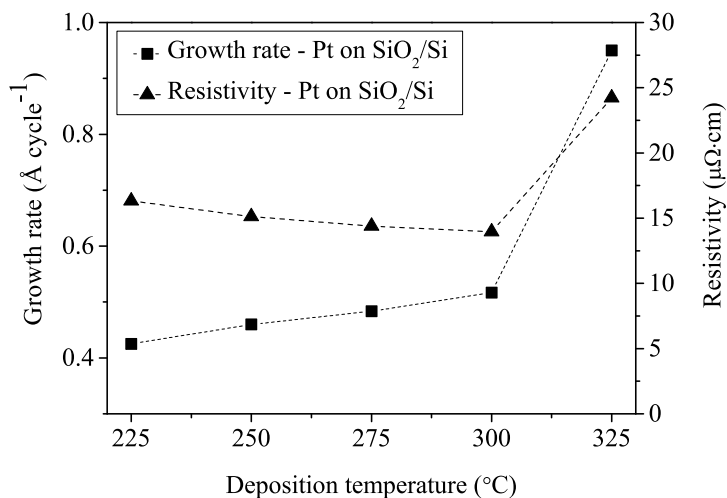
FIGURE 3.4: Growth rate and resistivity as a function of deposition temperature for Pt films (600 cycles) deposited on SiO_2/Si. The MeCpPtMe$_3$ pulse time was 1 s.

and was introduced into the reaction chamber through a hole in the reaction chamber lid above the distribution plate.

3.3   Experimental

The substrates used in this chapter were flat Si(100) with native SiO_2, wet-thermally oxidized Si(100) or Si(100) substrates coated with Al_2O_3 ALD (on top of the native SiO_2).

The purge time after both MeCpPtMe$_3$ and Ru(EtCp)$_2$ pulses was 6 s and the pulse/purge times of O_2 were 5 s/8 s throughout the ALD study.

The thickness of the ALD films was determined from X-ray reflectivity (XRR), measured with a PANalytical X'Pert Pro X-ray diffractometer. The crystalline phases were identified by grazing incidence X-ray diffraction (GIXRD) using the same diffractometer with an angle of incidence of 1°. X-ray photoelectron spectroscopy (XPS), K-Alpha from Thermo Scientific, equipped with a monochromated AlK$_\alpha$ X-ray source with energy of 1486.6 eV and X-ray spot size of 400 µm, was employed to determine the purity of the films. XPS depth profiles of the ALD films were obtained by sputtering with Ar$^+$ ions of 500 eV.
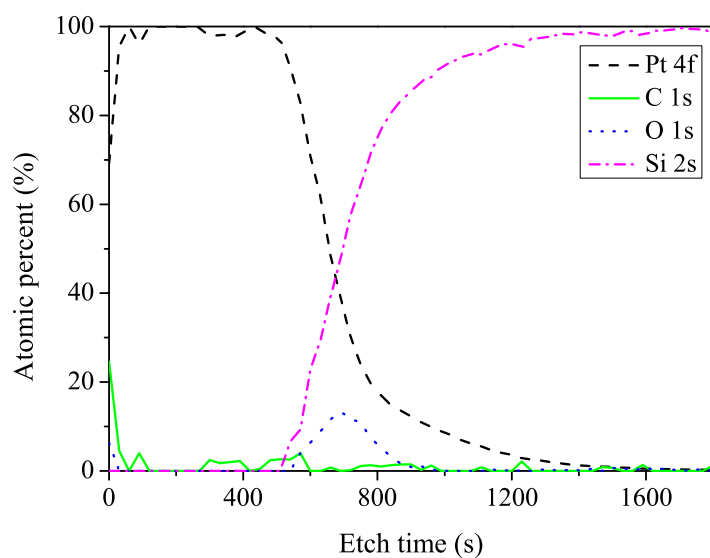
FIGURE 3.5: XPS depth profile of Pt film deposited on Si (300 cycles) at 250 ℃. The MeCpPtMe$_3$ pulse time during deposition was 1 s.
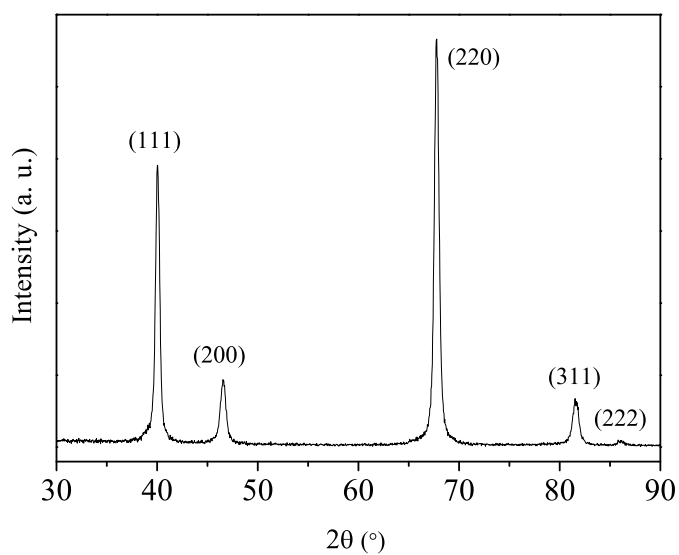
FIGURE 3.6: GIXRD of a Pt film deposited on SiO$_2$/Si at 250 ℃, revealling polycrystalline films. The Pt precursor pulse time during deposition was 1 s.

3.4   Evaluation of the Pt process

The dependence of growth rate and resistivity of Pt films (600 cycles) on deposition temperature is plotted in Fig. 3.4. The Pt films were deposited onto SiO_2/Si and the pulse time for $MeCpPtMe_3$ was 1 s. No Pt was deposited below 225 ℃. The self-limiting behavior was observed from 225 to 300 ℃. The growth rate at 300 ℃ was 0.5 Å/cycle, which is equivalent to previous work [33, 70]. However, at 325 ℃ the growth rate was significantly higher due to thermal decomposition of $MeCpPtMe_3$ [70]. The resistivity was reduced slightly with increasing temperature in the ALD window, from 16 to 14 µΩ·cm [70, 77]. Moreover, the resistivity was considerably higher for the film deposited at 325 ℃, probably caused by incorporation of Pt precursor ligands in the film.

Pt films deposited at 250 ℃ were further characterized using XPS depth profiling and GIXRD. The XPS depth profile in Fig. 3.5 shows the atomic percentages of platinum (Pt 4f), carbon (C 1s), oxygen (O 1s) and silicon (Si 2s) versus etch time for a Pt film (300 cycles) deposited on Si. The carbon and oxygen contaminations on the Pt surface were removed after one Ar^+ sputter cycle of 30 s and not detected in the bulk Pt film. The small oxygen peak at the interface of the Pt film and the Si substrate originated from the native SiO_2. The XPS depth profile shows that the Pt film was pure without incorporation of carbon from ligands or oxygen from partial oxidation of the Pt film. Pt films deposited at 275 and 300 ℃ have also been characterized and both had a composition of 100% of Pt 4f as well.

The GIXRD pattern shown in Fig. 3.6 reveals that the Pt film (600 cycles) deposited on SiO_2/Si was polycrystalline. Pt (111), (200), (220), (311) and (222) diffraction peaks were observed [78].

Fig. 3.7 shows growth rate and resistivity as a function of $MeCpPtMe_3$ pulse times for the Pt films (600 cycles) deposited on SiO_2/Si at 250 ℃. Saturated growth was obtained after 0.5 s. Furthermore, the resistivity was ~15 µΩ·cm for the films deposited with a Pt precursor pulse time of 0.5, 1 and 3 s and only slightly higher for the films grown with a $MeCpPtMe_3$ pulse time of 0.1 and 0.2 s.

Pt nucleation was strongly dependent on the initial substrate [35, 79, 80]. Here the nucleation behavior of Pt deposited onto SiO_2 has been studied. Fig. 3.8 shows the SEM images of Pt on SiO_2 for various ALD cycle numbers (150, 300, 600 and 1000 cycles). Pt ALD began with island growth on SiO_2. After 300 cycles the Pt film was almost continuous. With increasing cycle number the gaps between the islands became bigger and eventually a continuous film was formed.
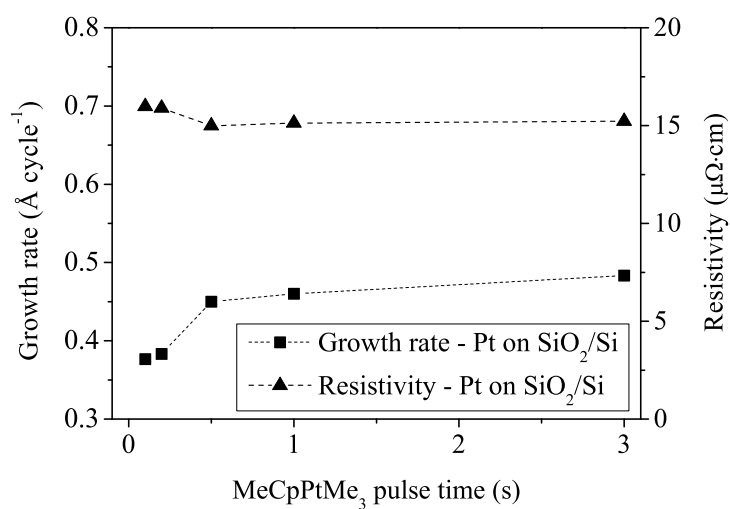
FIGURE 3.7: The dependence of growth rate and resistivity on the MeCpPtMe₃ pulse time for Pt films (600 cycles) deposited on SiO₂/Si at 250 ℃.
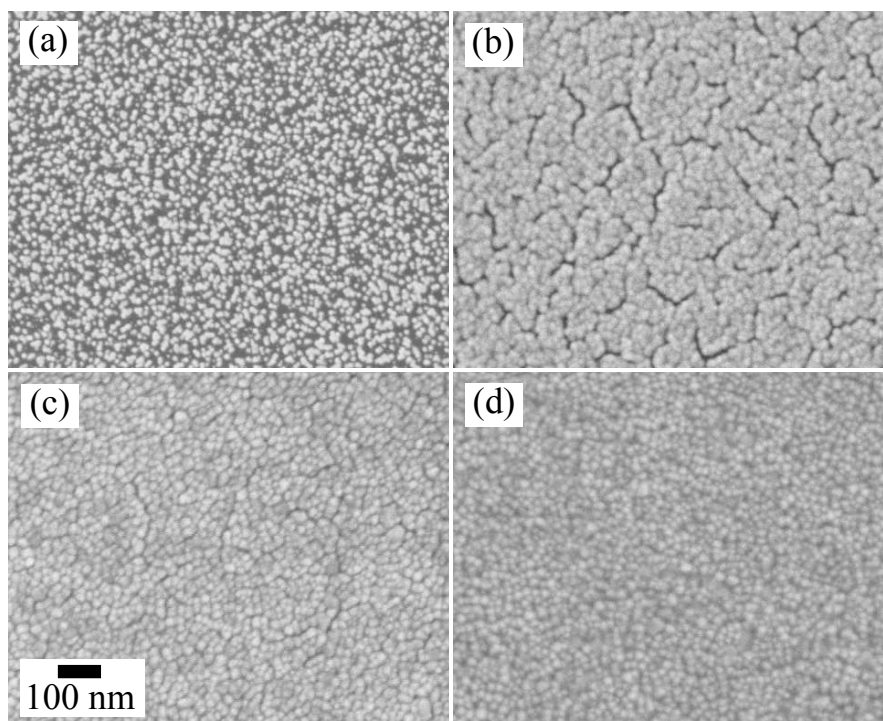
FIGURE 3.8: SEM images of Pt on SiO₂ with various Pt ALD cycle numbers: (a) 150, (b) 300, (c) 600 and (d) 1000 cycles.
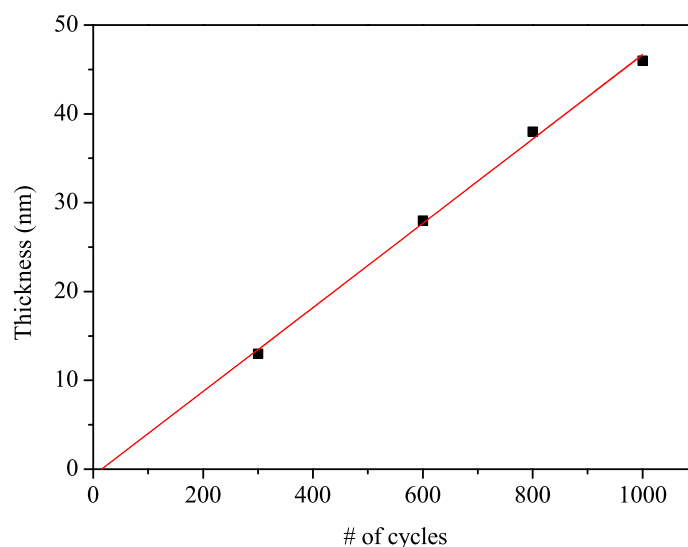
FIGURE 3.9: Thickness as a function of ALD cycle number for Pt deposited onto SiO_2.

The dependence of thickness on the number of Pt ALD cycles are plotted in Fig. 3.9. Linear fitting was applied to the four measurements and the line was then further extrapolated to the x-axis. The plot revealed a nucleation delay of few tens of ALD cycles.

3.5   Evaluation of the Ru process

Growth rate and resistivity of Ru films (1000 cycles) deposited on Al_2O_3/Si as a function of temperature are plotted in Fig. 3.10. The $Ru(EtCp)_2$ pulse time was 3 s. Below 250 ℃ there was no deposition of Ru. Furthermore, the ALD temperature window was not as well defined as for the Pt ALD process. The growth rate at 300 ℃ was 0.5 Å/cycle. However, similar to Pt, the resistivity was low, 15 µΩ·cm for the film deposited at 250 ℃, and it decreased somewhat with increasing deposition temperature, to 13 µΩ·cm at 325 ℃.

Fig. 3.11 shows a SEM image of the Ru film deposited at 250 ℃. The Ru film was further characterized using GIXRD (Fig. 3.12). The Ru (100), (002), (101), (102), (110), (103), (200), (112) and (201) diffraction peaks [81] indicate that the Ru film was polycrystalline. The two peaks at 2θ angle of 54-55° were from the Si substrate.

Fig. 3.13 shows the dependence of growth rate and resistivity on the $Ru(EtCp)_2$ pulse time for Ru films (1000 cycles) deposited on Al_2O_3/Si at 250 ℃. No saturation behavior was observed. Moreover, the resistivity of the films deposited with a $Ru(EtCp)_2$ pulse time of 0.5 s and 1 s was around six times higher compared to that of the Ru films
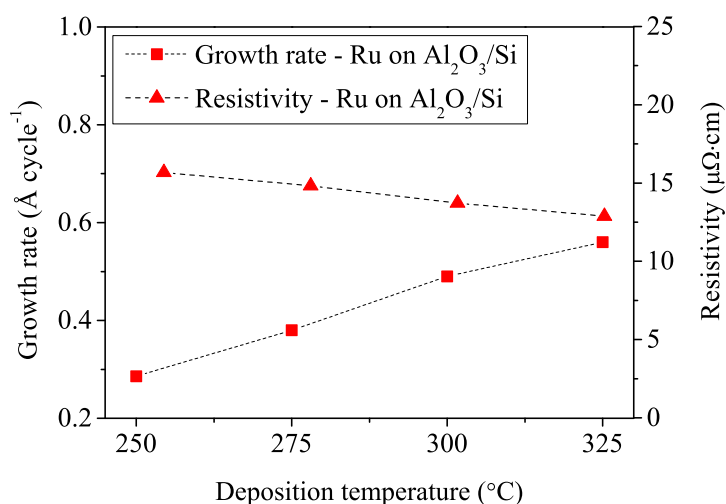
FIGURE 3.10: Growth rate and resistivity as a function of deposition temperature for Ru films (1000 cycles) deposited on Al_2O_3/Si. The $Ru(EtCp)_2$ pulse time was 3 s.
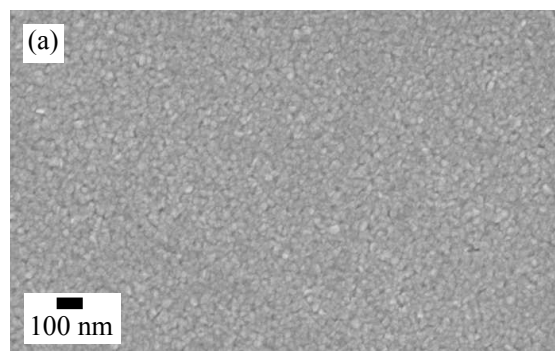
FIGURE 3.11: SEM image showing the morphology of the Ru film (1000 cycles) deposited at 250 ℃.

deposited with a Ru precursor pulse time of 3 s and 6 s. XPS depth profiling was performed in order to understand the difference in resistivity. The XPS depth profile in Fig. 3.14 depicts the atomic percentage of ruthenium (Ru 3d), oxygen (O 1s), aluminium (Al 2s) and silicon (Si 2p) versus etch time for the film deposited with a $Ru(EtCp)_2$ pulse time of 6 s. The XPS depth profile reveals that the surface was oxidized, but no oxygen was incorporated in the bulk of the film. Carbon impurities, on the other hand, could not be determined directly since carbon (as C 1s) has the same binding energy as the Ru $3d_{3/2}$ orbital. The area ratio of Ru $3d_{5/2}$ to Ru $3d_{3/2}$ was 1.3-1.4 before Ar^+ sputtering. After sputtering for 30 s, the ratio was close to 1.5, corresponding to the theoretical value due to spin-orbit interactions of d electrons [82]. This ratio remained virtually constant throughout the film and indicated that the carbon concentration in the bulk of the film was negligible. Similar results were obtained for the Ru film deposited at 300 ℃.
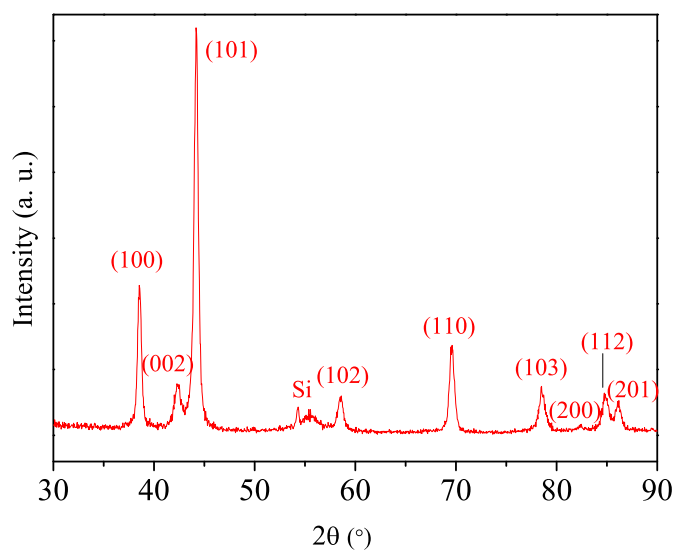
FIGURE 3.12: GIXRD of a Ru film deposited on Si at 250 ℃, revealing a polycrystalline film. The Ru precursor pulse time during deposition was 3 s.
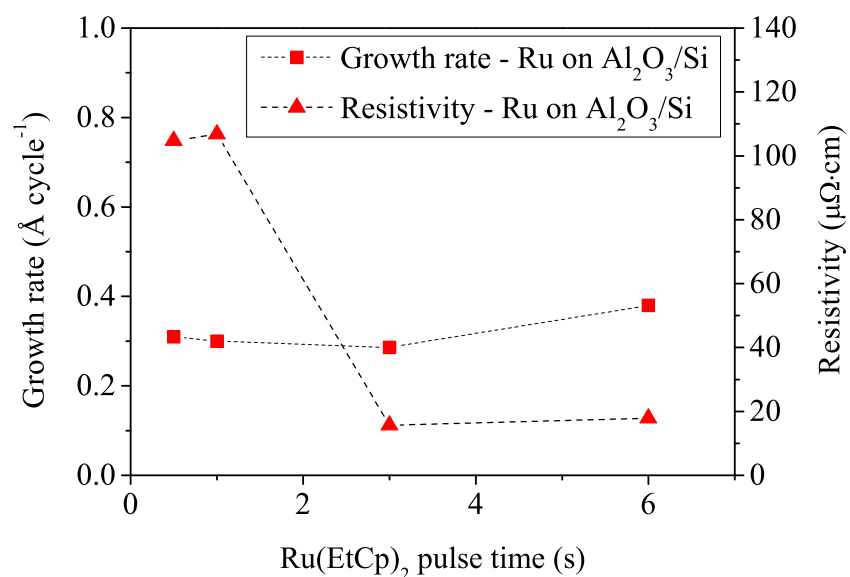
FIGURE 3.13: The dependence of growth rate and resistivity on the $Ru(EtCp)_2$ pulse time for Ru films (1000 cycles) deposited on Al_2O_3/Si at 250 ℃.
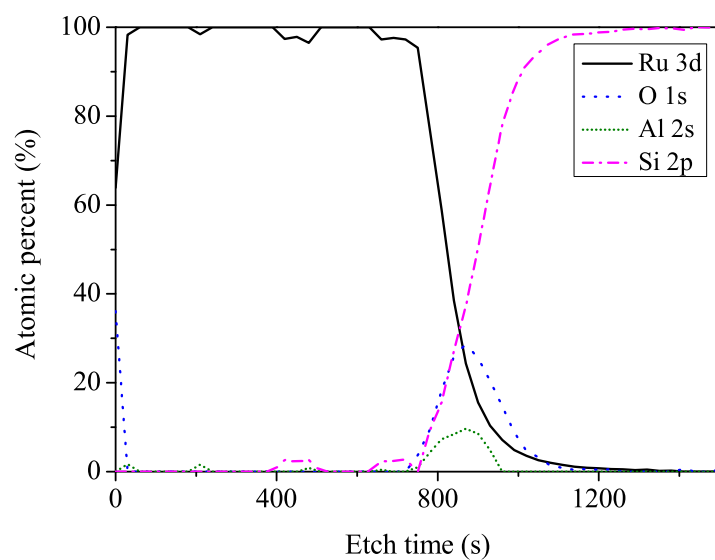
FIGURE 3.14: XPS depth profile of a Ru film (1000 cycles) deposited on Al_2O_3/Si at 250 ℃ with a Ru precursors pulse time of 6 s.
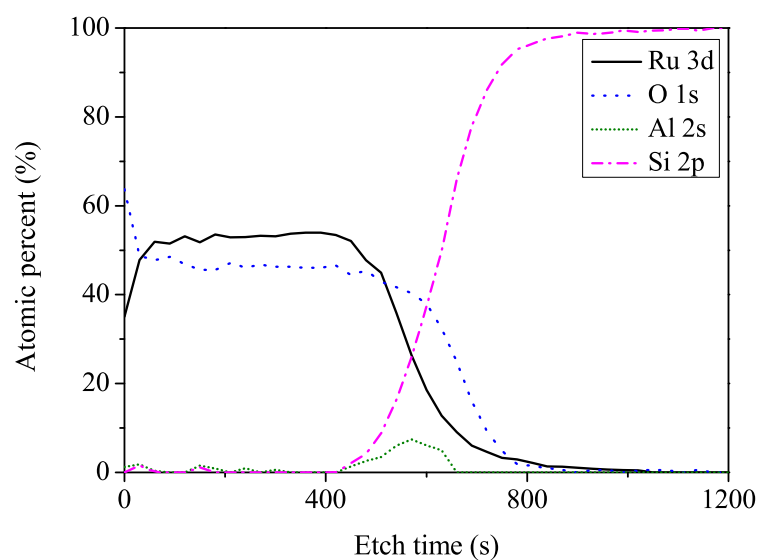
FIGURE 3.15: XPS depth profile of a Ru film (1000 cycles) deposited on Al_2O_3/Si at 250 ℃ with a Ru(EtCp)$_2$ pulse time of 0.5 s.

	Pt	Ru
Deposition temperature (℃)	250	250
Metal precursor	MeCpPtMe$_3$	Ru(EtCp)$_2$
Precursor temperature (℃)	55	95
Pulse/purge times of metal precursors (s)	1/6	3/6
Pulse/purge times of O$_2$ (s)	5/8	5/8

TABLE 3.1: ALD parameters

The XPS depth profile for the film grown with a Ru precursor pulse time of 0.5 s (Fig. 3.15), shows a Ru:O atomic ratio close to 1:1 throughout the deposited film. Thus, the higher resistivity was explained by the incorporation of oxygen. Similar XPS depth profile was obtained for the Pt film deposited with a Ru(EtCp)$_2$ pulse time of 1 s.

3.6   ALD parameters

Based on this study, the parameters used for all Pt and Ru depositions for fuel cell applications are summarized in Table 3.1. Using these parameters the growth rate for Pt was 0.46 Å/cycle and that of Ru was 0.29 Å/cycle. The Ru study in this chapter was performed using a Ru precursor temperature of 80 ℃. This temperature was later increased to 95 ℃ in order to ensure saturated growth over a larger area in the ALD reactor. For convenience the chosen deposition temperature for both processes was set to 250 ℃.

3.7   Summary

Pt and Ru ALD processes have been investigated, using MeCpPtMe$_3$ and Ru(EtCp)$_2$ as precursors, respectively, and O$_2$ as reactant in both processes. The growth rate at 250 ℃ was 0.46 Å/cycle for the Pt process and 0.29 Å/cycle for the Ru process. The noble metal films had a low resistivity, around 15 μΩ·cm. Moreover, they were pure and polycrystalline. At low pulse time of Ru precursor the film had a Ru:O atomic ratio close to 1:1.

The now established Pt and Ru ALD processes are used for the synthesis of N-CNT supported ALD catalysts in the following two chapters.

Chapter 4

Pt-Ru Catalysts on N-CNTs by ALD

This chapter introduces carbon nanotubes, and nitrogen-doped CNTs (N-CNTs) in particular. A nucleation study of Pt and Ru ALD onto N-CNTs will be presented, followed by the results from accelerated degradation tests (ADTs) on Pt ALD catalysts of various particle sizes. The rest of the chapter covers the work about Pt-Ru ALD catalysts of various compositions, supported on N-CNTs [83]. Properties of the catalysts including particle size, dispersion, composition and crystalline phases are presented, as well as their catalytic activity toward CO oxidation and methanol oxidation reaction (MOR).

4.1 N-doped carbon nanotubes (N-CNTs)

Multi-walled carbon nanotubes are hollow cylinders of multiple sheets of graphene. Boron and nitrogen are direct neighbors to carbon in the periodic table. They have therefore similar size and are among the most effective dopants for CNTs. In particular, N-doping has received attention. Each carbon atom in the hexagonal carbon framework of graphene is associated with one mobile electron, called π-electron. For each replacement of a C atom with a N atom, an additional electron is added, resulting in enhanced electrical conductivity. N-CNTs are found to be exclusively metallic unlike undoped ones, which can be either metallic or semiconducting [84]. In addition, it has been demonstrated that better catalyst dispersion, higher activity and durability are obtained using N-doped CNTs as support material [20, 85–91].
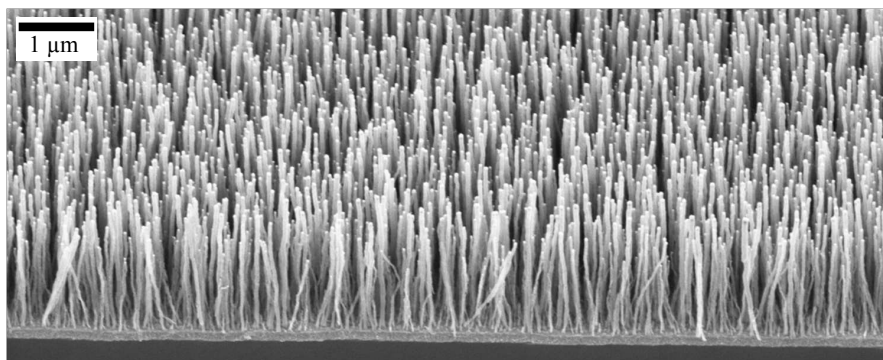
FIGURE 4.1: SEM image of as-grown, vertically aligned N-CNTs.

4.1.1 PECVD growth of N-CNTs

Chemical vapor deposition (CVD) is the most popular and widely used technique for CNT synthesis [92]. The N-CNTs used in this project were grown in an AIXTRON Black Magic plasma-enhanced CVD (PECVD) system, with a direct current plasma source. The plasma is created between two parallel plate electrodes by applying a voltage across them, causing gas breakdown. The growth substrate, placed onto one of the electrodes, was flat Si(100) 4" wafer, coated with 100 nm of sputtered TiW (Wordentec QCL 800) and 3 nm of E-beam evaporated Ni (Wordentec QCL 800), serving as the diffusion barrier and CNT growth catalysts, respectively. The CNTs were grown at 850 ℃ at a pressure of 6 mbar with 100 W of plasma power. The flows of nitrogen, acetylene and ammonia during growth were 100, 40 and 160 sccm, respectively.

Fig. 4.1 shows a SEM image of as-grown, vertically standing N-CNTs. The applied voltage bias induces an electric field, forcing the N-CNTs to align to the direction of the electric field as they grow [93]. The growth mode is tip growth, as the Ni catalysts are observed to be at the tip of the CNTs. The dark structure in e.g., Fig. 4.2a, pointed out by the arrow, is the Ni particle.

The N-doping was confirmed by XPS, by acquiring the elemental composition of the N-CNTs grown on the Ni/TiW/Si substrate. The atomic percentage of each identified element is summarized in Table 4.1. A total of 5.3 at.% of N was detected. High-resolution XPS spectra of O 1s showed that most of the oxygen originated from metal oxides. Besides that, smaller amounts of oxygen were incorporated in the CNTs as C-O and C=O. Ni was from the CNT growth catalysts, and Ti and W originated from the TiW diffusion barrier film. The tiny amount of F was due to contamination.

In most cases, CNTs doped with N exhibit a bamboo-like structure with regularly arranged compartments [84, 94]. This structure is not well pronounced in the tubes, see e.g., Fig. 4.2a, which could be explained by the high doping level of nitrogen [89, 91].

Element	at.%
C	83.2
N	5.3
O	6.7
Ni	2.3
Ti	1.4
W	0.8
F	0.4

TABLE 4.1: Elemental composition of the N-doped CNTs grown on Ni/TiW/Si wafer.
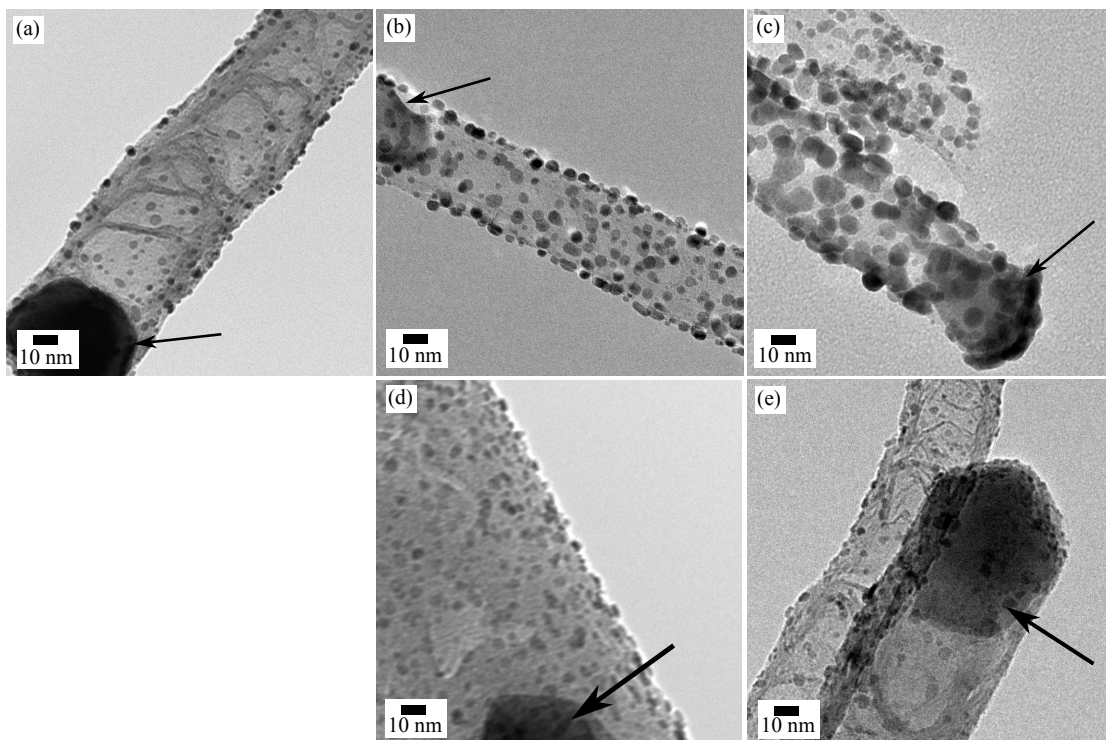
FIGURE 4.2: TEM images of N-doped CNTs coated with (a) 50, (b) 100 and (c) 150 ALD cycles of Pt, and (d) 100 and (e) 150 ALD cycles of Ru. The CNT growth catalysts are pointed out by the arrows.

Moreover, in the same figure the thick tube wall reveals that the CNT was made up of multi-walls.

4.2 Pt and Ru ALD onto N-CNTs

Pristine CNTs are chemically inert [16] and must therefore be functionalized by e.g., acid or plasma prior to ALD [8, 26, 95–98], but as a consequence the electrical and chemical properties of the CNTs are affected [84]. Doping with nitrogen is a benign approach of making the CNTs chemically active [84, 94, 99]. Without any pre-treatment, Pt and Ru were deposited onto the N-CNTs. TEM images of N-CNTs coated with 50, 100 and
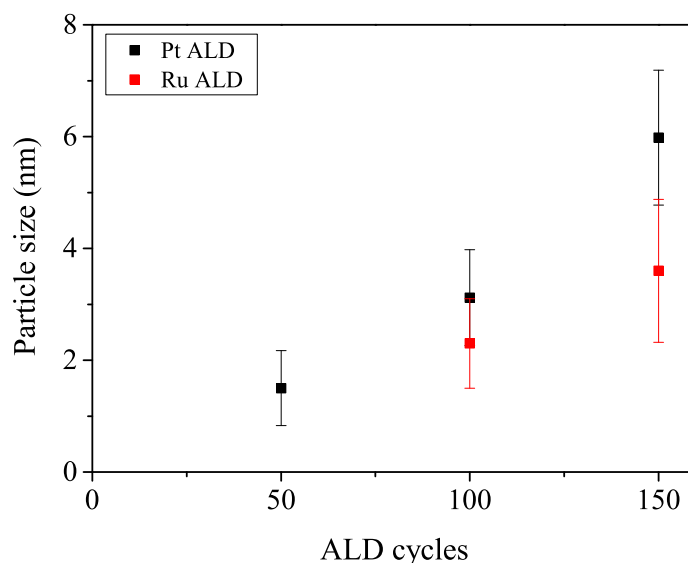
FIGURE 4.3: Dependence of Pt and Ru particle size on the number of ALD cycles.

150 cycles of Pt, and 100 and 150 cycles of Ru are shown in Fig. 4.2a, b, c, d and e, respectively. These images show that the Pt and Ru particles were well dispersed onto the surface of the carbon support, as a result of the introduction of nucleation sites with the N-doping [90].

The relationship between the average particle size of catalysts on N-CNTs and the number of ALD cycles of Pt and Ru, see Fig. 4.3, was determined from TEM images by measuring the size of around 50 particles for each data point. The particles were measured at the top of the CNTs. There was an uncertainty in the measurements due to difficulties in observing particles smaller than 1 nm. In addition, due to the fact that TEM is a see-through technique, there was also the problem of separating particles at opposite sides of the N-CNT that appeared to be a single particle of a larger size due to overlapping in the TEM images. Thus, the calculated average particle sizes were probably slightly higher than the actual values. Nevertheless, as expected, the average particle size increased with the number of ALD cycles. Furthermore, a nucleation delay of the first few tens of cycles was observed, which is common for noble metal ALD processes [6]. The mean particle size of Pt catalysts (150 cycles) was 6.0±1.1 nm and Ru catalysts (150 cycles) was 2.7±1.4 nm.

A particle size gradient along the N-CNTs was observed, with larger particles at the top. The flow-type ALD reactor used in this study is not optimal for depositing onto high aspect-ratio structures. By increasing the pulse time of precursors one might be able to reduce the particle size distribution, but at the cost of wastage of expensive precursors. Christensen et al. [32] deposited Pt-Ru catalysts onto alumina support, also
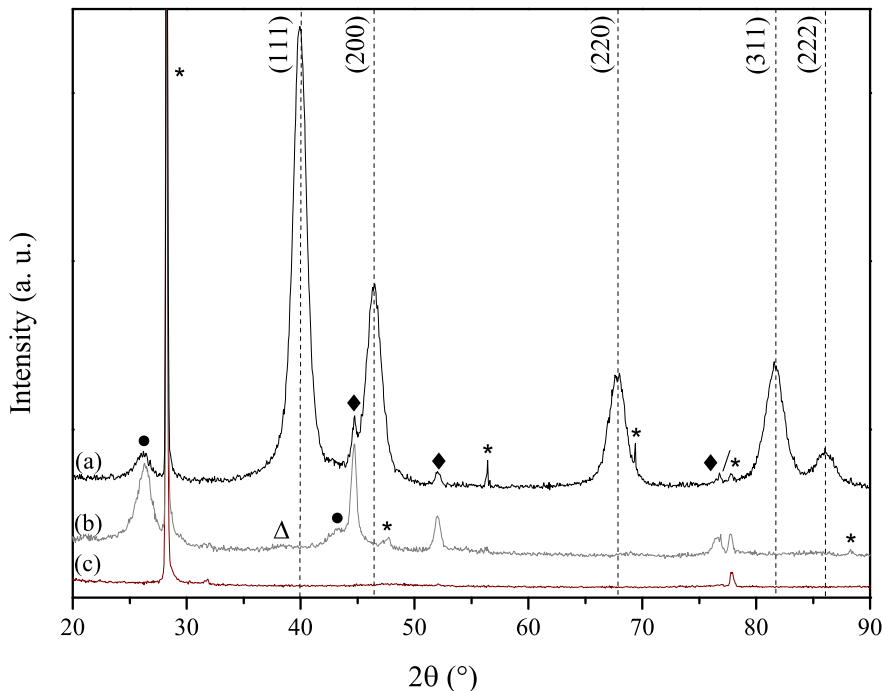
FIGURE 4.4: Pseudo-GIXRD of (a) Pt150/N-CNT, (b) Ru150/N-CNT and (c) zero-background Si plate. The vertical dashed lines mark the Pt intensity peaks, from left: (111), (200), (220), (311) and (222). Ru, C, Ni and Si intensity peaks are labeled by the symbols Δ, •, ♦ and ∗, respectively.

in a flow-type ALD reactor. Precursors' pulse time of 200 s and purge time of 50 s resulted in no nucleation delay and narrow particle size distribution. However, the more ideal way to deposit onto high aspect-ratio or porous structures would be to have an exposure (or dwelling) duration between the pulse and purging steps where the pump is isolated from the deposition chamber. This would allow more time for the precursor vapors to penetrate and react on the surface of the structure before being removed from the chamber [100].

XRD was performed on decorated N-CNTs using a Panalytical Empyrean diffractometer. Materials to be characterized were scraped off onto a zero-background Si plate and the powder was gently compressed to get a smooth surface. Due to the small amount of catalyst material, GIXRD was performed with an incident angle of 2 °. It was denoted pseudo-GIXRD due to the lack of a parallel plate collimator for the diffracted beam, which means the measurements were sensitive to errors associated with the instrument and sample, such as sample displacement, surface roughness and axial divergence. This could result in minor distortion of the peak positions and intensities. The data were scaled to the background Si peak at $2\theta = 28.2$ °. Any slight shift in 2θ due to measurement errors was also corrected.

The XRD spectra for Pt150/N-CNT, Ru150/N-CNT and the zero-background Si plate are plotted in Fig. 4.4a, b and c, respectively. The intensity peaks associated with

Si are labeled by ∗. The peaks at around 26 ° and 43 °, each marked by •, were related to the carbon support material. Three intensity peaks corresponding to Ni, the CNT growth catalyst, were also detected, each marked by ♦. Fig. 4.4a is the XRD spectrum for Pt150/N-CNT. The vertical dashed lines mark the characteristic peaks of the face-centered cubic (fcc) crystalline Pt, namely (111), (200), (220), (311) and (222). Fig. 4.4b is the XRD spectrum for Ru150/N-CNT. The intensity of reflections from Ru were much smaller than those of Pt. A possible Ru peak at around 38 ° is labeled by Δ. The strongest Ru peak was supposed to be located at 44 °, thus overlapping with Ni. The reason for the weaker signal from Ru could be due to lack of crystallinity.

The mean size of the catalysts, L, was determined from the diffractograms, using the Scherrer equation [101]:

$$L = \frac{K\lambda}{\beta cos\theta} \tag{4.1}$$

K is a dimensionless shape factor, commonly set to 0.9, but it varies with the actual shape of the crystallite [102]. λ is the X-ray wavelength. Here Cu K-alpha was used, which has a wavelength of 1.5418 Å. β is the line broadening at full width at half maximum (FWHM) of the peak of interest and θ is the Bragg angle, both values in radians.

The average particle size of the Pt150/N-CNT electrocatalysts was calculated from the X-ray diffractogram using the Pt diffraction peak at 40 °. The FWHM was determined by fitting the peak to a Gaussian function. The mean particle size for Pt150/N-CNT was 5.4 nm. It is an average value over complete N-CNTs and therefore expected to be smaller than that estimated at the top of N-CNTs in TEM images, which was also the case. The XRD result will furthermore only show the size of the crystalline part, whereas TEM will show the entire particle with a potential amorphous shell.

4.3 Preparation of working electrode

ALD catalysts supported on N-CNTs were characterized using a glassy carbon electrode (PINE Instruments) as working electrode in the three-electrode electrochemical set-up. Before usage the glassy carbon was polished with Buehler MicroPolish Alumina Powder 0.05 micron on cloth and rinsed in water. The cleanliness of the electrode was also tested using cyclic voltammetry (CV) in 0.5 M H_2SO_4. A catalyst ink for each type of catalyst was prepared as follows: Vertically grown CNTs coated with ALD catalysts on Si wafer pieces were dispersed in ethanol using an ultrasonic bath. The ethanol was then evaporated in a vacuum desiccator and the remaining catalyst powder was dispersed in Millipore H_2O (18 MΩ·cm), ethanol and 5 wt.% Nafion solution (DE 520, DuPont) for
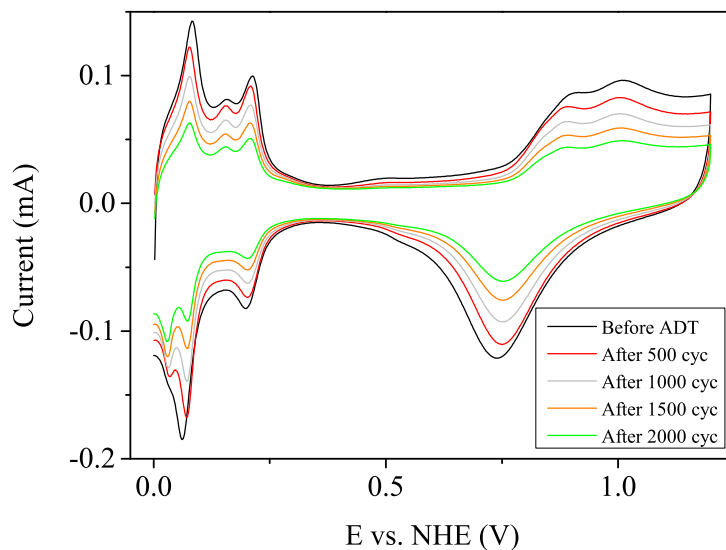
FIGURE 4.5: CV of Pt150/N-CNT at 20 mV/s, obtained before and after every 500 accelerated degradation cycles in 0.5 M H_2SO_4.

10 min using a horn sonicator to obtain a well-dispersed ink. An aliquot of the catalyst ink was pipetted onto the glassy carbon disk electrode, followed by drying in an air oven at 80 ℃ for 15 min or in a fume hood at room temperature.

4.4   ADT on Pt ALD catalysts of various sizes

Accelerated degradation tests (ADT) on N-CNT supported Pt ALD catalysts of various sizes (100, 150 and 200 ALD cycles) and commercial Pt/KB (HiSPEC 13100, Johnson Matthey Fuel Cells) were conducted. The procedure was as follows. Each test was performed by applying a potential from 0.6 to 1.2 V at a scan rate of 50 mV/s for 2000 CV cycles. Before, as well as during the run-time, 10 CVs from 0 to 1.2 V at a scan rate of 20 mV/s were measured after 500, 1000, 1500 and 2000 cycles to determine the electrochemically active surface area (ECSA) of Pt. The ECSA was calculated from the H_{upd} region[1] from the 10th CV cycle. The area in the H_{upd} region (and consequently the ECSA) was reduced with increasing number of CV cycles. This is illustrated for the Pt150/N-CNT catalyst in Fig. 4.5.

Normalized ECSA as a function of number of ADT cycles are plotted in Fig. 4.6 for Pt-KB, Pt100/N-CNT, Pt150/N-CNT and Pt200/N-CNT catalysts. A particle size relation to the normalized ECSA was observed for the ALD catalysts, i.e., the larger the particles the higher the durability. The particle size of the Pt100/N-CNT catalyst was

---

[1]See region I in Fig. 2.3 on page 16.
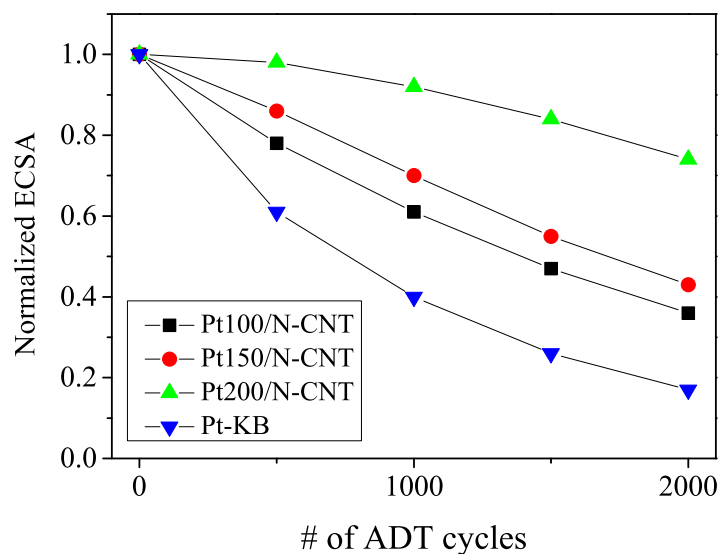
FIGURE 4.6: Normalized ECSA versus number of ADT cycles for Pt ALD catalysts of various sizes (100, 150 and 200 ALD cycles) deposited on N-doped CNTs and compared with commercial Pt-KB (HiSPEC 13100, Johnson Matthey Fuel Cells).

around 3 nm. They were smaller than the Pt-KB, which had a maximum crystallite size of 4.6 nm according to the catalyst provider. Despite the smaller size of Pt100/N-CNT, it exhibited higher durability, which could be due to the difference in carbon support. Chen et al. [89] investigated the stability of Pt catalysts supported on carbon black, undoped CNTs and CNTs of various nitrogen doping levels. All catalysts supported on CNTs exhibited higher durability. Moreover, they also found that the higher the N-doping level the higher the catalyst durability. The higher durability of catalysts on undoped CNTs were associated with the interaction between the nanoparticles and the π bond, originating from the unpaired electrons in the hexagonal carbon structure. The durability of the catalysts was further improved on N-doped CNTs due to enhanced π-bonding, contributed by the lone electron pair in nitrogen and the basic property of the N-CNTs [20].

4.5   ALD of Pt-Ru catalytsts

The first approach to evaluate ALD as a technique for the synthesis of catalysts was by depositing Pt-Ru catalysts of various compositions onto N-doped CNTs. The Pt-Ru system presented here could be used in a conventional fuel cell as well as in a miniaturized Si-based DMFC.

Catalyst	at.% Pt	at.% Ru	Average particle size (nm) TEM/STEM	XRD
Pt-Ru16-4/N-CNT	71	29	N/A	5.0
Pt-Ru8-4/N-CNT	61	39	4.3±0.9/3.3±0.7/2.4±0.5	3.5
Pt-Ru4-4/N-CNT	44	56	4.6±1.1	3.2
Pt-Ru4-8/N-CNT	32	68	2.9±0.9	2.9
Pt-Ru4-16/N-CNT	17	83	3.0±0.9	2.1

TABLE 4.2: Catalyst composition obtained using XPS and average particle size determined using TEM/STEM and XRD. The particles in the TEM images were measured at the top of the N-CNTs, except for Pt-Ru8-4/N-CNT, for which mean particle size was calculated at top/middle/bottom.
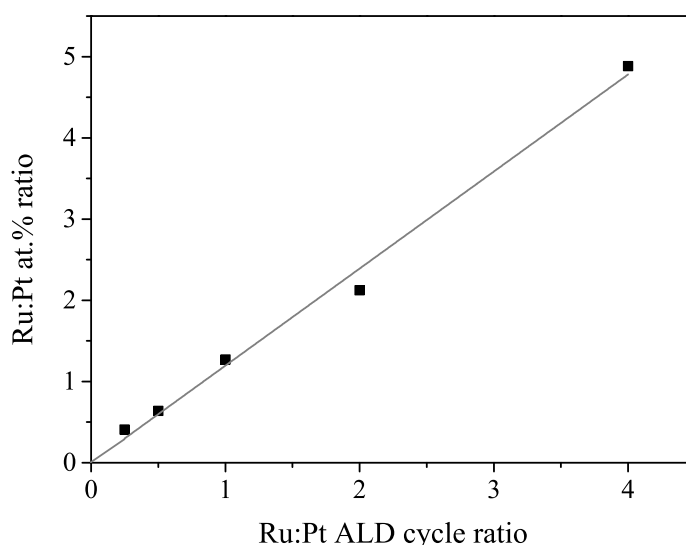
FIGURE 4.7: Linear correlation between the Ru:Pt at.% ratio and the Ru:Pt ALD cycle ratio.

The tested catalysts are listed in Table 4.2. They were prepared by depositing various amounts of "ALD supercycles" up to around 150 ALD cycles in total. As an example, for the Pt-Ru16-4/N-CNT catalyst one supercycle consisted of 16 cycles of Pt and 4 cycles of Ru. The supercycle was repeated until the total number of cycles was 150. The composition of the catalysts with respect to platinum and ruthenium was determined using XPS from high resolution scans of Pt 4f and Ru $3d_{5/2}$, and the results are summarized in Table 4.2. The relation between the Ru:Pt ALD cycle ratio and Ru:Pt at.% ratio has been further investigated, Fig. 4.7. A linear correlation was observed, revealing that the composition could be easily tuned. Comparison of the atomic percentage of Pt and Ru for e.g., Pt-Ru16-4/N-CNT and Pt-Ru4-16/N-CNT, reveals that more Ru atoms were deposited per Ru cycle than Pt atoms during a Pt cycle.

Fig. 4.8a shows a high-angle annular dark field (HAADF) scanning TEM (STEM) image
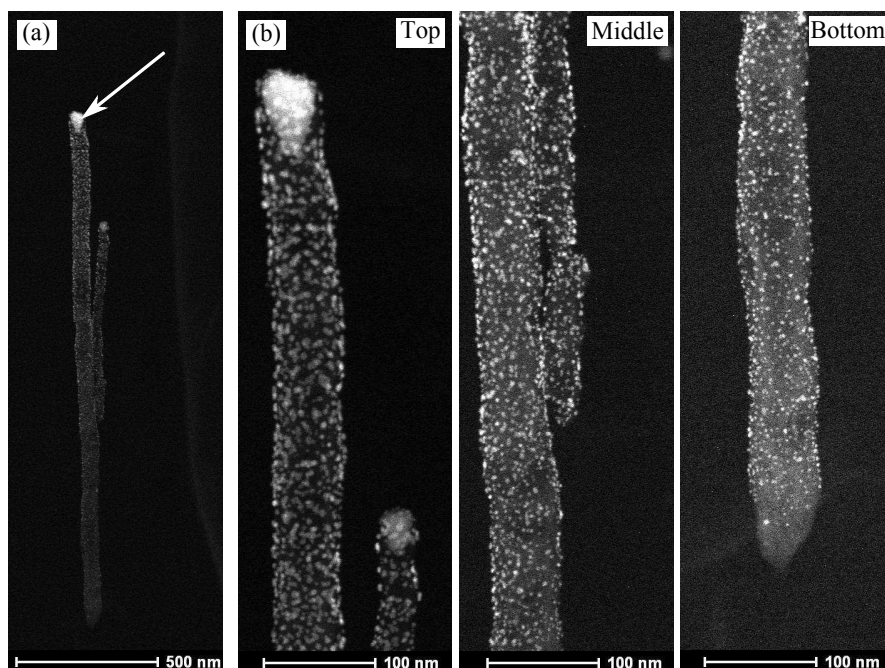
FIGURE 4.8: (a) HAADF STEM image of a 1.8 µm long N-CNT coated with Pt-Ru8-4 catalysts and (b) close-up STEM images of the N-CNT in (a), showing top, middle and bottom part of the N-CNT. The arrow points at the CNT growth catalyst.

of a 1.8 µm long N-CNT coated with Pt-Ru8-4 catalysts, acquired using a FEI Tecnai F30ST, operated at 300 kV. The STEM images in Fig. 4.8b are close-up images of the N-CNT in Fig. 4.8a, showing top, middle and bottom segment of the N-CNT. The particles are well distributed along the tube wall, but slightly smaller particles are observed at the bottom of the tube for the Pt-Ru catalysts as well. The average particle size at the top, middle and bottom was estimated and the values are listed in Table 4.2, together with mean particle size values for the other Pt-Ru catalysts acquired at the top. It is noted that the particle size was reduced with increasing content of Ru.

XRD was performed on the catalysts using pseudo-GIXRD mode, by applying same sample preparation and set-up as for the Pt and Ru catalysts in section 4.2. The results are plotted in Fig. 4.9b-f. XRD for Pt150/N-CNT and zero-background Si plate are again plotted for comparison, Fig. 4.9a and g, respectively. The vertical dashed lines mark the location of the Pt intensity peaks, whereas the C, Ni and Si intensity peaks are labeled by •, ♦ and ∗, respectively. The diffraction peaks associated with Pt were slightly shifted to higher 2θ angles with respect to those of pure Pt, as a function of increasing amount of Ru in the electrocatalysts. The shift is related to a reduction of the unit cell. The Ru atom is smaller than the Pt atom, suggesting the formation of an alloy with Ru substituted in the fcc structure of Pt [103, 104]. Therefore, it seems that bimetallic Pt-Ru of high Ru content could crystallize in a fcc structure, as has also been reported earlier [105]. Recently, it has been shown that even pure Ru can
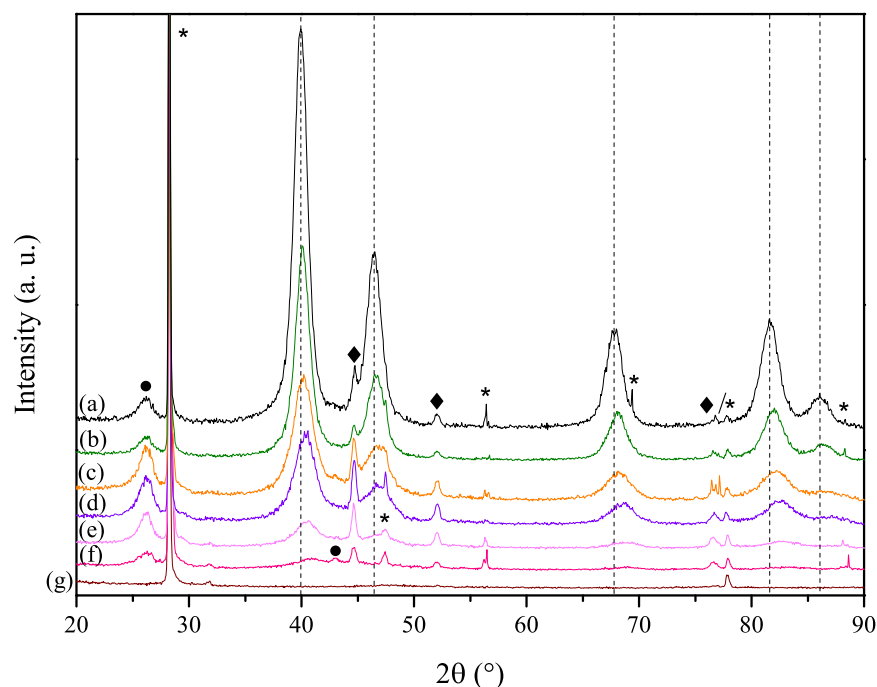
FIGURE 4.9: Pseudo-GIXRD of (a) Pt150/N-CNT, (b) Pt-Ru16-4/N-CNT, (c) Pt-Ru8-4/N-CNT, (d) Pt-Ru4-4/N-CNT, (e) Pt-Ru4-8/N-CNT, (f) Pt-Ru4-16/N-CNT and (g) zero-background Si plate. The vertical dashed lines mark the Pt intensity peaks. C, Ni and Si intensity peaks are marked by ●, ◆ and ∗, respectively.

form a fcc structure [106]. As visible in Fig. 4.9, the intensity of the Pt peaks was systematically decreased in intensity with increasing amount of Ru. This is most likely due to decreasing crystallinity and/or crystalline perfection of the alloy particles, i.e., due to a higher density of defects in the crystalline particles. Furthermore, broadening of the Pt peaks with increased Ru content was observed, revealing there was also a particle size dependence. However, no peak corresponding to Ru was observed. Using the Scherrer Equation (Eq. 4.1) the average particle size of the Pt-Ru catalysts was estimated and the results are summarized in Table 4.2. Again, these values were smaller than those calculated by measuring in TEM/STEM images.

4.5.1 Electrochemical procedures

The electrochemical procedures of the ALD catalysts supported onto N-CNTS were as follows:

1. The CVs were first performed in 0.5 M H_2SO_4 solution at 50 mV/s for 60 cycles between 0 and 1.0 V for the Pt catalysts and up to 0.8 V for the Ru catalysts. This was

followed by 10 cycles at 20 mV/s, using the same potential window and the 10th cycle was plotted.

2. CO-stripping was performed next. Adsorption of CO on the electrode catalyst was conducted by bubbling the electrolyte with CO gas (5% CO in Ar, 99%) for 45 min, followed by purging with N_2 for 30 min. During CO and N_2 purging the working electrode potential was set to 50 mV and the electrolyte was magnetically stirred. The CO-stripping and blank CV curves were obtained from two consecutive scan cycles at 20 mV/s in the potential window of 50 mV and 1.0 V for the Pt catalyst and up to 0.8 V for the Ru-containing catalysts [60].

3. The methanol electro-oxidation study on the N-CNT supported catalysts was performed by CV measurements in 1.0 M CH_3OH + 0.5 M H_2SO_4 solution. The CV curves were recorded from 0 to 0.8 V at a sweep rate of 10 mV/s for 10 cycles and the anodic sweep of the 1st cycle was plotted for comparison.

4. Chronoamperometry was performed in 1.0 M CH_3OH + 0.5 M H_2SO_4 by holding the potential at 0.4 V for 1 h.

Specific activity of the catalysts was used to compare the various catalysts. The ECSA was calculated from the CO-stripping voltammograms.

4.5.2 Electrochemical characterization of Pt-Ru ALD catalysts

Fig. 4.10b shows the CVs of the various Pt-Ru catalysts, obtained in 0.5 M H_2SO_4 at 20 mV/s. The Pt150/N-CNT and Ru150/N-CNT catalysts are used as references and their corresponding CVs are plotted in Fig. 4.10a and b, respectively. The three characteristic potential regions for the Pt150/N-CNT catalyst are well defined: The hydrogen underpotential deposition (H_{upd}) region between ∼0-0.3 V, the double layer charging/discharging region up to about 0.6 V, and adsorption/desorption of oxygenated species on the surface of Pt. The peaks in the H_{upd} region are due to the presence of different Pt crystalline facets. The origin of the hump at around 0.48 V is not completely clear. It has been observed by others [96, 107, 108] and is probably associated with oxygenated species on the carbon support. The CVs in Fig. 4.10b for the Pt-Ru and Ru catalysts display completely different, but among themselves similar features. The effect of Ru is clear in the CVs. The peaks in the H_{upd} region are not visible due to the significantly less activity of Ru toward H adsorption/desorption [59] and Ru oxide formation, commencing already at around 0.2 V [12]. As a consequence of the latter, the current density of the double layer region increases with the atomic percentage of Ru in the catalysts.
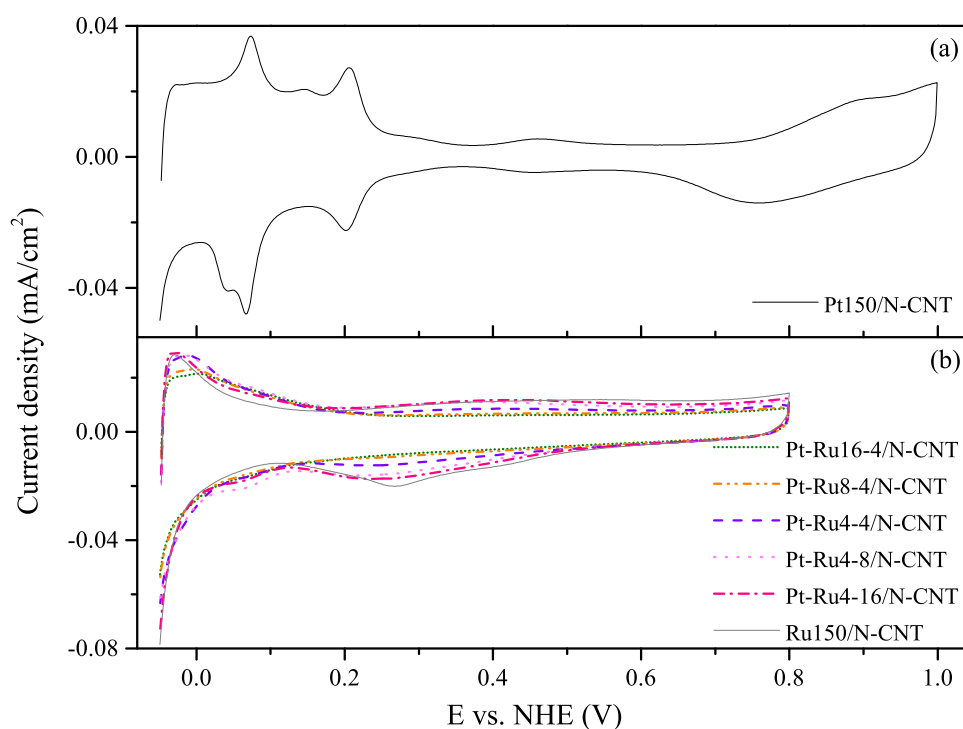
FIGURE 4.10: CVs of (a) Pt150/N-CNT and (b) N-CNT supported Pt-Ru and Ru ALD catalysts, obtained in 0.5 M H_2SO_4 at 20 mV/s: Pt-Ru16-4/N-CNT (short dot), Pt-Ru8-4/N-CNT (dash dot dot), Pt-Ru4-4/N-CNT (dash), Pt-Ru4-8/N-CNT (dot), Pt-Ru4-16/N-CNT (dash dot) and Ru150/N-CNT (solid).

The tolerance toward CO poisoning was evaluated from CO-stripping experiments in 0.5 M H_2SO_4. Fig. 4.11 displays the CVs recorded for the different ALD catalysts. The solid and the dashed lines are the first and the second cycles, respectively, measured after CO adsorption at 50 mV. The CO-stripping peak for the Pt150/N-CNT catalyst in Fig. 4.11a has a shoulder before the main oxidation peak, suggesting that the electrocatalyst had two types of reaction sites or crystallites with different activities that were resolvable in the CO oxidation measurement [58]. The onset potential of CO oxidation for the Pt-Ru and Ru catalysts are marked by the vertical dotted line in the figure. It is shifted around -0.2 V with respect to that for the Pt catalyst. As suggested in connection with Fig. 4.10, Ru adsorbed oxygen-containing species at more negative potentials than Pt, thereby enabling CO oxidation at lower potentials.

The vertical solid line in Fig. 4.11 is a visual guide for comparison of the CO oxidation peak potential for the Pt-Ru and Ru catalysts. It can be noted from the figure that the peak potentials are similar, with Pt-Ru4-8/N-CNT deviating from the others. There is no trend between peak potential and catalyst composition, as was observed by Gasteiger et al. [60]. They also noted a narrower peak width for Pt-Ru electrodes compared to pure Ru, which was explained by an intrinsically higher rate constant for the oxidation
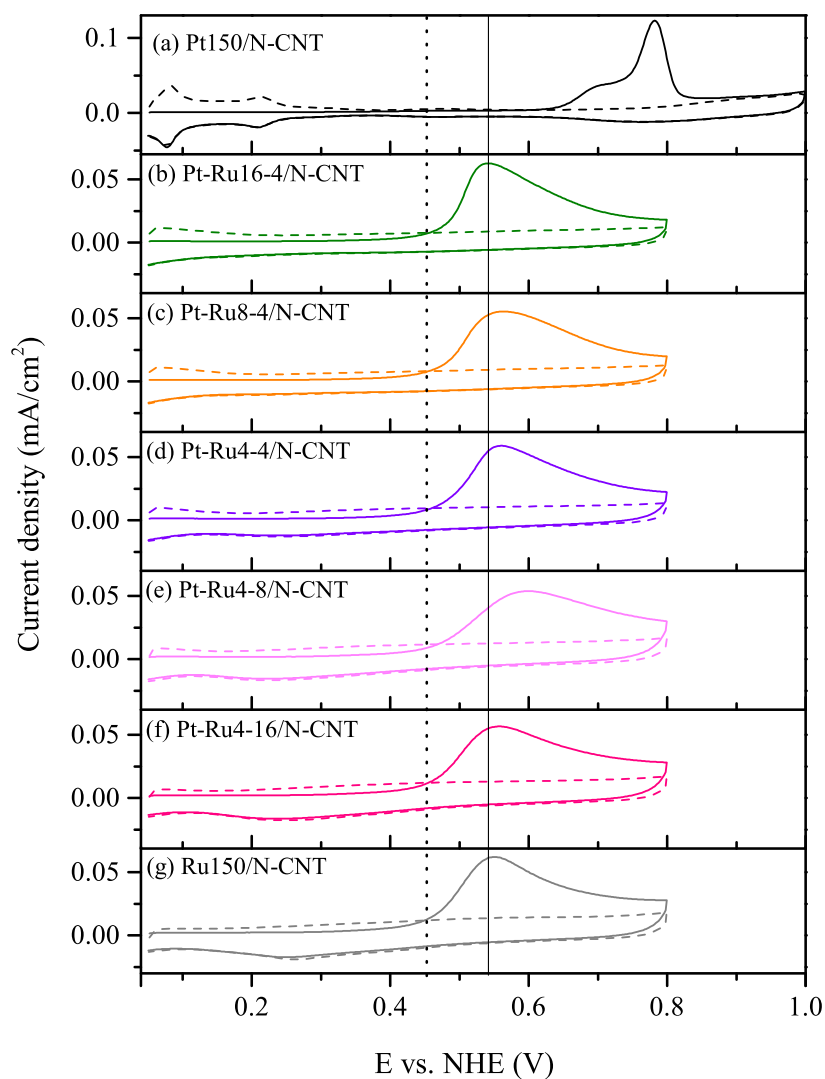
FIGURE 4.11: CO-stripping voltammograms of the Pt, Pt-Ru and Ru catalysts, obtained in 0.5 M H_2SO_4 at 20 mV/s after CO adsorption at 50 mV: (a) Pt150/N-CNT, (b) Pt-Ru16-4/N-CNT, (c) Pt-Ru8-4/N-CNT, (d) Pt-Ru4-4/N-CNT, (e) Pt-Ru4-8/N-CNT, (f) Pt-Ru4-16/N-CNT and (g) Ru150/N-CNT. The vertical dotted line marks the onset potential of CO oxidation for the Pt-Ru and Ru catalysts. The vertical solid line is a visual guide for comparison of the CO oxidation peak potential for the Pt-Ru and Ru catalysts.
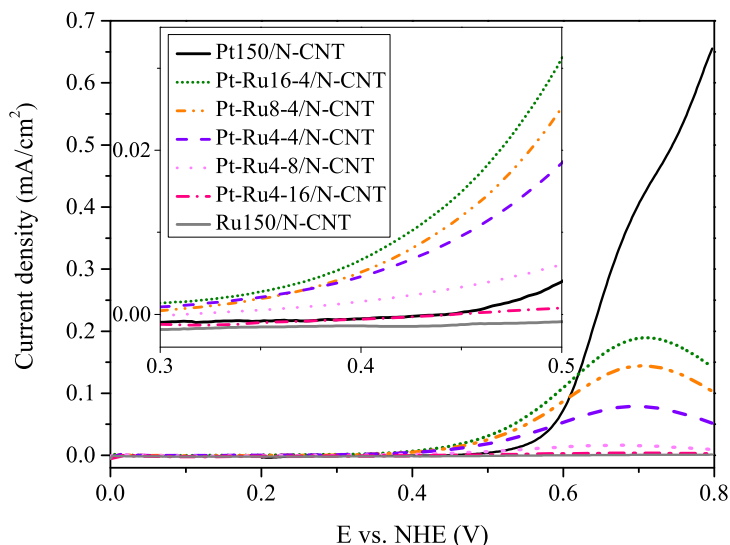
FIGURE 4.12: Anodic scans of the N-CNT supported Pt and Pt-Ru ALD catalysts, obtained in 1.0 M CH_3OH + 0.5 M H_2SO_4 at 20 mV/s: Pt150/N-CNT (solid), Pt-Ru16-4/N-CNT (short dot), Pt-Ru8-4/N-CNT (dash dot dot), Pt-Ru4-4/N-CNT (dash), Pt-Ru4-8/N-CNT (dot), and Pt-Ru4-16/N-CNT (dash dot).

of surface-bound CO with oxygen species on alloy electrodes compared to pure Ru. In our study the width of the CO oxidation peak for the Pt-Ru and Ru ALD catalysts is similar. Thus, it seems that the CO was inefficiently removed from the Pt-Ru catalysts. The reason could be related to non-ideal mixtures of Pt and Ru at the catalyst surface and that surface migration of CO bound to Pt atoms was needed.

Catalytic activity of the Pt, Pt-Ru and Ru ALD catalysts for the electro-oxidation of methanol was investigated using cyclic voltammetry and chronoamperometry in 1.0 M CH_3OH + 0.5 M H_2SO_4. Fig. 4.12 presents the anodic scans of the 1st CV cycle at 10 mV/s. The insert displays a magnification at low potentials, where methanol oxidation commences. The background in 0.5 M H_2SO_4 at 10 mV/s was subtracted from the CVs. Methanol was dehydrogenated at low potentials, but the Pt sites was blocked, mainly by CO. The anodic scans of the Pt-Ru catalysts show that the promotional effect of Ru is most pronounced at low overpotentials, which is also the potentials of technological interest in a DMFC [12].

The current density for Pt150/N-CNT is similar to that for Pt-Ru4-16/N-CNT at 0.4 V, and increases rapidly from 0.6 V, at which potential Pt alone could dissociate water with a reasonable rate to form -OH groups and oxidize the poisoning carbon species. Moreover, as expected, Ru150/N-CNT was inactive toward the methanol oxidation reaction (MOR) [109].
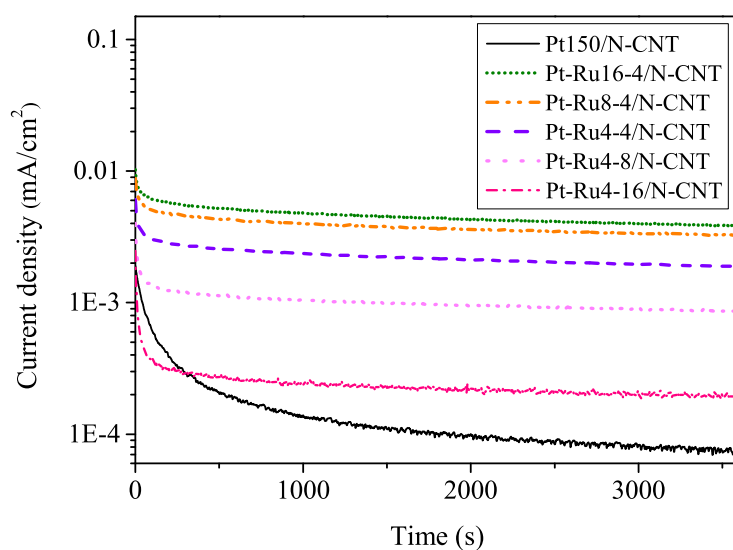
FIGURE 4.13: Chronoamperograms of the various N-CNT supported Pt, Pt-Ru and Ru ALD catalysts, obtained in 1.0 M CH_3OH + 0.5 M H_2SO_4 at 0.4 V: Pt150/N-CNT (solid, black), Pt-Ru16-4/N-CNT (short dot), Pt-Ru8-4/N-CNT (dash dot dot), Pt-Ru4-4/N-CNT (dash), Pt-Ru4-8/N-CNT (dot), Pt-Ru4-16/N-CNT (dash dot) and Ru150/N-CNT (solid, gray).
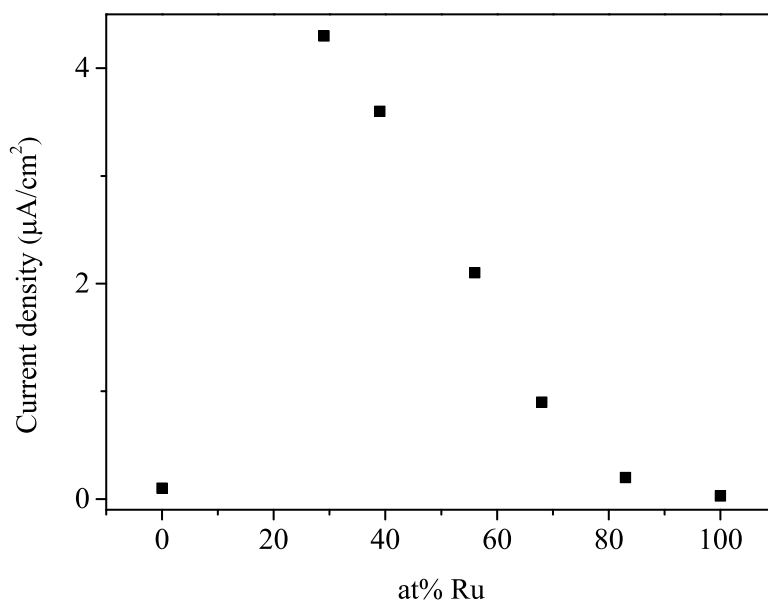
FIGURE 4.14: Current density at 2000 s as a function of Ru composition. For the compositions investigated, maximum current density was obtained for the catalyst with a Ru content of 29 at.%.

Chronoamperometry was performed on the catalysts at 0.4 V for 1 h in the methanol containing solution to investigate the steady-state behavior, and the results are plotted in Fig. 4.13. Apart from the first 250 s, all Pt-Ru catalysts deliver higher current densities than Pt150/N-CNT. The current density at 2000 s is plotted as a function of atomic percentage of Ru in Fig. 4.14. The highest catalytic activity was obtained for Pt-Ru16-4/N-CNT, having a Ru content of 29 at.%. The plot clearly shows that the activity is significantly lower for pure Pt and that it is gradually reduced with increasing Ru content from 29 at.% and up to 100 at.%. There was a clear improvement for the Pt-Ru catalysts, in correspondence to the bifunctional mechanism [12]. There might also be a ligand effect, but it is typically less effective [110].

4.6 Summary

Vertically aligned, N-CNTs were grown in a PECVD reactor. The nitrogen doping was confirmed using XPS. Highly dispersed Pt and Ru ALD nanoparticles were deposited onto the N-CNT support without pre-treatment. The dependence of particle size on the number of ALD cycles was determined. XRD showed that the Pt particles were polycrystalline. The intensities of reflections from the Ru particles were very low, indicating the lack of crystallinity.

The durability of the CNT-supported Pt ALD particles of various particle sizes was investigated and compared with commercial Pt/KB (HiSPEC 13100, Johnson Matthey Fuel Cells). The improvement in durability was attributed to the N-CNT support.

Pt-Ru ALD catalysts of various compositions were deposited onto N-CNTs. The composition was easily controlled by changing the ratio of Pt ALD cycles to Ru ALD cycles. The composition of the catalysts was determined using XPS. All catalysts were evaluated toward CO oxidation and MOR using cyclic voltammetry and chronoamperometry. Based on the electrochemical measurements it was concluded that the specific catalytic activity was highly related to the composition of Ru, and for the compositions investigated, the best catalyst was made up of 29 at.% of Ru. The results were explained by the bifunctional and ligand models.

In the next chapter another series of ALD catalysts is evaluated, i.e., Ru-decorated Pt catalysts, and the best catalyst out of the two series will be compared with commercial Pt-Ru/KB.

Chapter 5

Ru-Decorated Pt Catalysts on N-CNTs by ALD

This chapter covers the electrochemical results about the second ALD catalyst series, i.e., Ru-decorated Pt catalysts, published in [69]. The best ALD catalyst among the two catalyst series (presented in this and previous chapters) is then compared with commercial Pt-Ru/KB (HiSPEC 12100, Johnson Matthey Fuel Cells). The procedures for preparation of working electrode and electrochemical testing are the same here as in preceding chapter, and described in section 4.3 and 4.5.1, respectively. The carbon support is also the same, i.e., nitrogen-doped multi-walled carbon nanotubes (N-CNTs).

5.1 Ru-decorated Pt catalysts

Ru-decorated Pt electrocatalysts have been studied since the 1970s [11]. It has been shown that an alloy is not a prerequisite, but Pt and Ru atoms have to be in close proximity [21, 111–113]. Ru has been added to the Pt surface using several methods, e.g., spontaneous deposition, electrochemical deposition and chemical vapor deposition [23]. The choice of method influences the resulting surface structure and the catalytic activity.

In this chapter, ALD is applied to synthesize Ru-decorated Pt catalysts for the first time. The catalysts were prepared by depositing various Ru ALD cycles (1, 2, 5, 10 and 20) on top of N-CNT supported Pt ALD nanoparticles (150 cycles), labeled Ru1Pt150/N-CNT, Ru2Pt150/N-CNT, Ru5Pt150/N-CNT, Ru10Pt150/N-CNT and Ru20Pt150/N-CNT, respectively. Similar to the previous chapter, undecorated Pt catalysts, Pt150/N-CNT, were used as the reference.
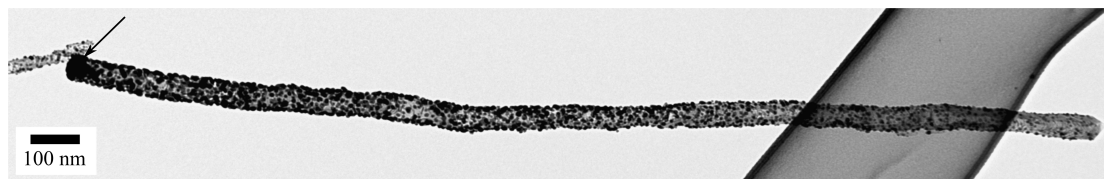
FIGURE 5.1: TEM image of a 2 μm long N-CNT with ALD catalysts (Ru10Pt150/N-CNT). The arrow points at the Ni catalyst particle.

In prior chapter the mean particle size for Pt150/CNT was determined from XRD data, and was found to be around 5.4 nm. Due to the small amount of Ru deposited, the particle size for these catalysts has not been determined. Ru has higher surface energy than Pt, ∼3.1 versus ∼2.5 J/m^2 [114]. Therefore, Ru is expected to nucleate as islands on Pt. Fig. 5.1 shows a TEM image of a 2 μm long CNT with well-dispersed ALD catalysts (Ru10Pt150/N-CNT) along the tube wall.

The CVs for the Pt and Ru-decorated Pt catalysts in Fig. 5.2 were acquired in 0.5 M H$_2$SO$_4$ at 20 mV/s and the 10th cycle is plotted. The features in the CV for Pt150/N-CNT in Fig. 5.2a are typically observed for Pt catalysts. The three distinct regions are addressed to hydrogen underpotential deposition (H$_{upd}$) (∼0-0.3 V), charging/discharging of the double layer (up to about 0.6 V) and adsorption/desorption of oxygenated species on the surface of Pt, commencing at about 0.6 V.

The CVs for Ru1Pt150/N-CNT and Ru2Pt150/N-CNT are plotted in Fig. 5.2b. The features in the H$_{upd}$ region are less pronounced compared to those for Pt150/N-CNT. For comparison, the CVs for the catalysts with higher Ru content (Ru5Pt150/N-CNT, Ru10Pt150/N-CNT and Ru20Pt150/N-CNT) are plotted in Fig. 5.2c. The effect of Ru is clear in the CVs. The peaks in the H$_{upd}$ region are not visible due to the significantly less activity of Ru toward H adsorption/desorption [59] and Ru oxide formation, commencing already at around 0.2 V. As a consequence of the latter, the current density of the double layer region is increased with the number of Ru ALD cycles.

Fig. 5.3 depicts the CO-stripping voltammograms recorded for the different ALD catalysts after CO adsorption at 50 mV. The solid and the dashed lines are the first and the second cycles, respectively. The vertical dotted line marks the location of onset potential of CO oxidation for Ru2Pt150/N-CNT, whereas the vertical solid line marks the peak potential for the same catalyst. The CO stripping and background voltammograms for Pt150/N-CNT are plotted in Fig. 5.3a. The CO-stripping peaks obtained for the catalysts with added Ru, Fig. 5.3b-f, are shifted around -0.2 V. As mentioned in connection with Fig. 5.2c, Ru dissociates water at more negative potentials than Pt, thereby enabling CO oxidation at lower potentials. Moreover, the CO stripping voltammogram for
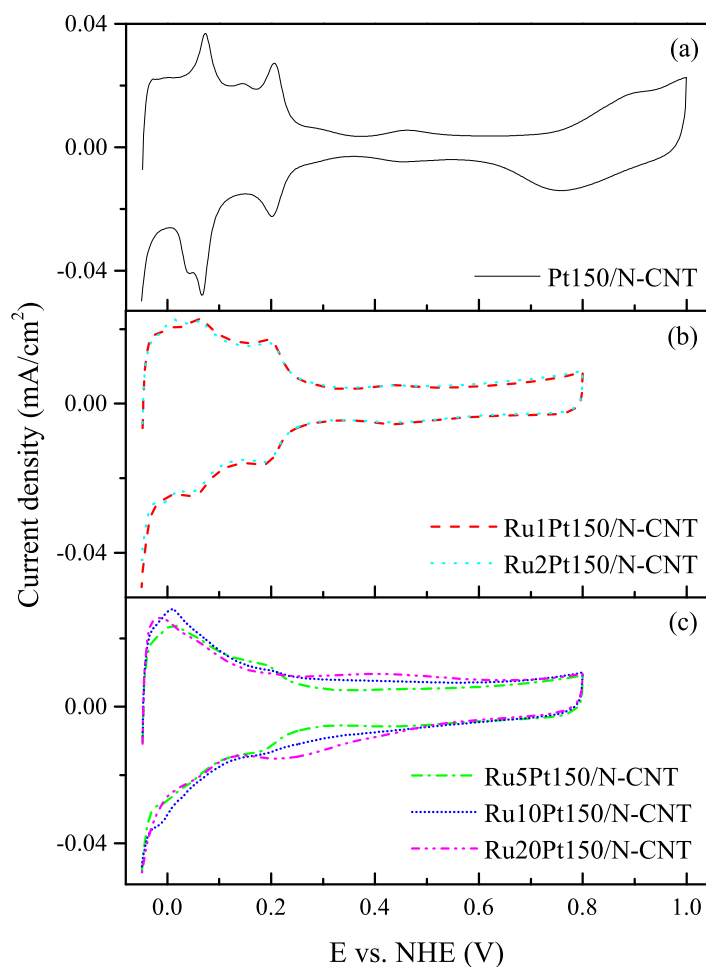
FIGURE 5.2: CVs of (a) Pt150/N-CNT, (b) Ru1Pt150/N-CNT and Ru2Pt150/N-CNT, and (c) Ru5Pt150/N-CNT, Ru10Pt150/N-CNT and Ru20Pt150/N-CNT catalysts, obtained in 0.5 M H_2SO_4 at 20 mV/s.

Ru1Pt150/N-CNT in Fig. 5.3b reveals that Ru was deposited onto Pt already during the first ALD cycle, meaning there was no nucleation delay in this ALD process.

The peak acquired for Ru2Pt150-CNT is located at lowest potential. Thus, two Ru ALD cycles seem sufficient for the preparation of a CO oxidation tolerant catalyst. However, similar to the Pt-Ru ALD catalysts in previous chapter, the oxidation peaks are relatively wide. The reason here could be limited contact area of Pt and Ru atoms, resulting in migration of CO on Pt sites to OH-groups on Ru [60].

Catalytic activity of the Pt and Ru-decorated Pt catalysts for methanol oxidation was measured using cyclic voltammetry and chronoamperometry in 1.0 M CH_3OH + 0.5 M H_2SO_4. Fig. 5.4 presents the anodic scans of the 1st CV cycle at 10 mV/s. The
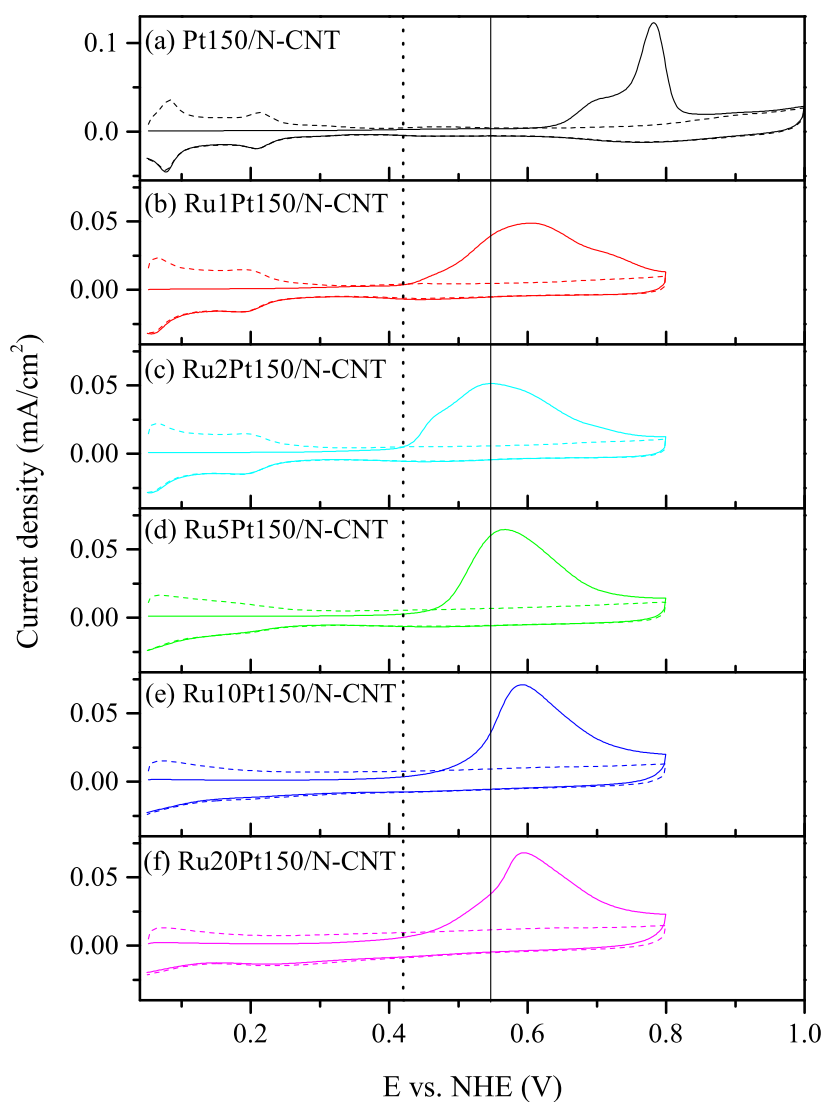
FIGURE 5.3: CO-stripping voltammograms of (a) Pt150/N-CNT, (b) Ru1Pt150/N-CNT, (c) Ru2Pt150/N-CNT, (d) Ru5Pt150/N-CNT, (e) Ru10Pt150/N-CNT and (f) Ru20Pt150/N-CNT catalysts in 0.5 M H_2SO_4 solution at 20 mV/s. The solid and the dashed lines are the first and the second CVs after CO adsorption at 50 mV, respectively. The vertical dotted line marks the onset potential of CO oxidation for Ru2Pt150/N-CNT, whereas the vertical solid line marks the peak potential for the same catalyst.
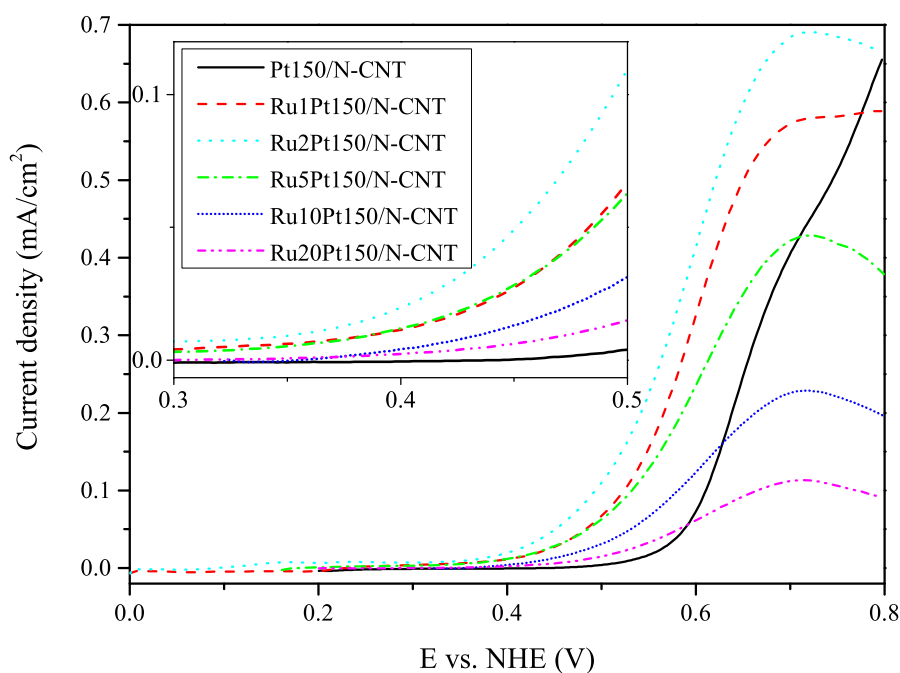
FIGURE 5.4: Anodic scans of the 1st CV cycle at 10 mV/s, obtained in 1.0 M CH$_3$OH + 0.5 M H$_2$SO$_4$ for the Pt and Ru-decorated Pt electrocatalysts. The inset is a magnification at low potentials where the electro-oxidation of methanol commences.

insert displays a magnification at low potentials, where the electro-oxidation of methanol commences. The background in 0.5 M H$_2$SO$_4$ at 10 mV/s was subtracted from the CVs. Methanol dehydrogenation commences at low potentials, but the sites get blocked mainly by adsorbed CO. The anodic scans show that the promotional effect of Ru is most pronounced at low overpotentials. At 0.4 V the Pt catalyst with 2 Ru ALD cycles added (Ru2Pt150/N-CNT) exhibits highest catalytic activity, followed by the Ru5Pt150/N-CNT, Ru1Pt150/N-CNT, Ru10Pt150/N-CNT, Ru20Pt150/N-CNT and Pt150/N-CNT catalysts. Furthermore, the oxidation current for the Pt150/N-CNT catalyst increases rapidly from 0.6 V and onwards, at which potential Pt alone can dissociate water with a reasonable rate to form OH-groups and oxidize poisoning carbon species. Despite this, Ru2Pt150/N-CNT delivers higher current densities at all potentials.

Chronoamperometry was performed on the catalysts at 0.4 V for 1 h in the methanol containing solution to investigate the steady-state behavior, see Fig. 5.5. The Ru-decorated Pt catalysts deliver higher current densities and get poisoned at lower rates, indicating that all of them are better catalysts toward the MOR. The current densities after 2000 s for the Pt150/N-CNT, Ru1Pt150/N-CNT, Ru2Pt150/N-CNT, Ru5Pt150/N-CNTs, Ru10Pt150/N-CNTs and Ru20Pt150/N-CNTs were 0.3, 3.1, 7.7, 5.1, 3.4 and 1.5 µA/cm^2, respectively.
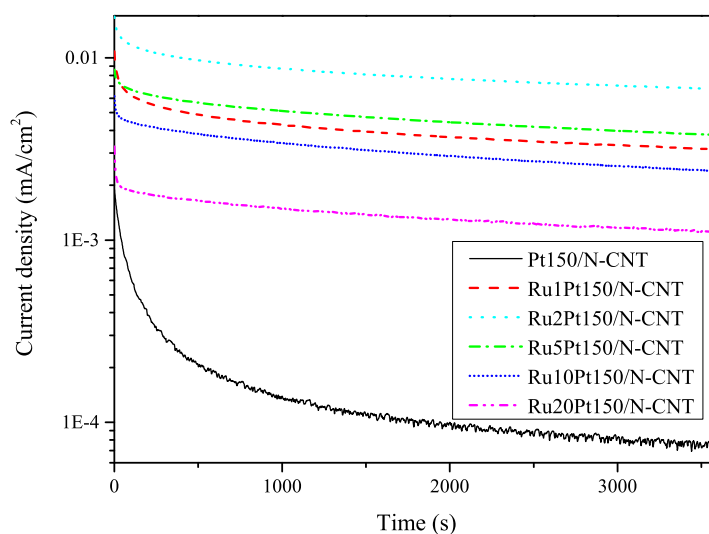
FIGURE 5.5: Chronoamperograms of the Pt and Ru-decorated Pt catalysts in 1.0 M CH$_3$OH + 0.5 M H$_2$SO$_4$ at 0.4 V.

According to the bifunctional mechanism, both Pt and Ru sites are needed at the surface of the catalyst in order to oxidize methanol at low potentials. Furthermore, three neighbouring Pt sites are required in order to dehydrogenate methanol at room temperature [115]. The best catalytic activity was measured for the catalyst with only 2 Ru ALD cycles. By depositing more Ru a dilution effect of Pt is probably observed, meaning there are fewer locations fulfilling the requirement of Pt ensembles. However, since Ru is inert toward methanol adsorption at room temperature [116] and that the Ru20Pt150/N-CNT catalyst is active toward MOR, the surface of the Ru20Pt150/N-CNT catalyst cannot be completely coated with Ru. There is probably also a ligand effect, but it is typically less effective [117]. The ligand effect is only for the Pt atoms in close proximity of the Ru islands.

5.2 Best ALD catalyst versus commercial Pt-Ru/KB

The best catalysts from the two series presented in this and previous chapters were Pt-Ru16-4/N-CNT and Ru2Pt150/N-CNT. By comparing those two the Ru2Pt150/N-CNT was the best, with an almost twice as high current density at 2000 s in the chronoamperometry experiment. In this section the catalytic activity of Ru2Pt150/N-CNT will therefore be compared with that of commercial Pt-Ru/KB (HiSPEC 12100, Johnson Matthey Fuel Cells).
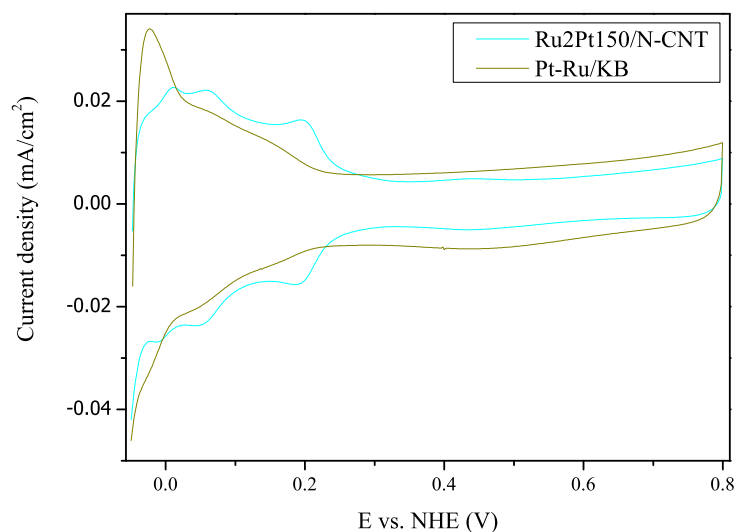
FIGURE 5.6: CVs of Ru2Pt150/N-CNT and Pt-Ru/KB in 0.5 M H_2SO_4 at 20 mV/s.
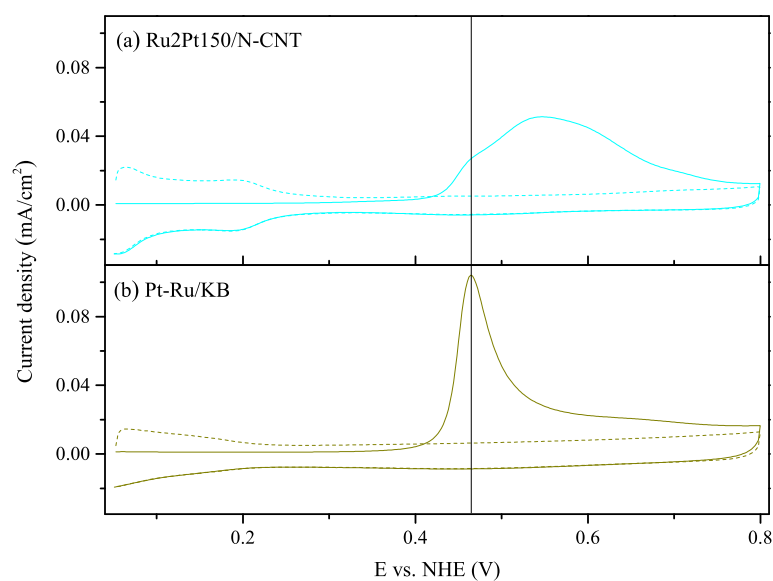
FIGURE 5.7: CO-stripping voltammograms of (a) Ru2Pt150/N-CNT and (b) Pt-Ru/KB, recorded in 0.5 M H_2SO_4 at 20 mV/s. The solid and the dashed lines are the first and the second CV cycles, respectively. The vertical solid line marks the CO oxidation peak potential for Pt-Ru/KB.

Fig. 5.6 shows CVs of Ru2Pt150/N-CNT and Pt-Ru/KB recorded in 0.5 M H_2SO_4 at 20 mV/s and the 10th cycle is plotted. The features in the H_{upd} region are different for the two catalysts. In contrast to the commercial Pt-Ru catalyst, the ALD catalyst displays peaks associated with hydrogen adsorption and desorption. The explanation could simply be that the Pt surface composition of Ru2Pt150/N-CNT is higher.
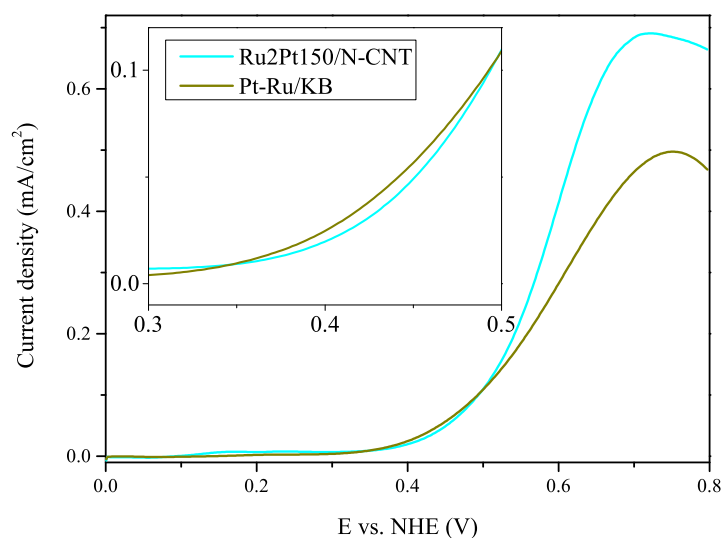
FIGURE 5.8: Anodic scans of first CV cycle for Ru2Pt150/N-CNT and Pt-Ru/KB, obtained in 1.0 M CH_3OH + 0.5 M H_2SO_4 at 10 mV/s.

The CO-stripping voltammograms for Ru2Pt150/N-CNT and Pt-Ru/KB are plotted in Fig. 5.7a and b, respectively. It is clear that the commercial catalyst is far more efficient in removing the adsorbed CO monolayer than the ALD catalyst. This is revealed by the smaller width of the peak, suggesting a good mixture of Pt and Ru on the surface of the catalyst.

First anodic sweeps in 1.0 M CH_3OH + 0.5 M H_2SO_4 at 10 mV/s for Ru2Pt150/N-CNT and Pt-Ru/KB are plotted in Fig. 5.8, with the inset showing a magnification at low potentials. At 0.4 V the current density for the Pt-Ru/KB is slightly higher than that for Ru2Pt150/N-CNT. At higher potentials the opposite is observed, again suggesting a high atomic percentage of Pt on the surface of the ALD catalyst.

Fig. 5.9 shows the chronoamperograms for the catalysts at 0.4 V for 1 h. The current density for Pt-Ru/KB is higher than that for the ALD catalyst. The commercial electrocatalyst probably has a good fraction of arrangements of three neighbor Pt sites, resulting in high electrochemical activity.

5.3   Summary

Ru-decorated Pt catalysts supported on N-doped CNTs were prepared and evaluated electrochemically toward CO oxidation and MOR. The loading was adjusted by varying the number of Ru ALD cycles (1, 2, 5, 10 and 20). Undecorated Pt catalysts were
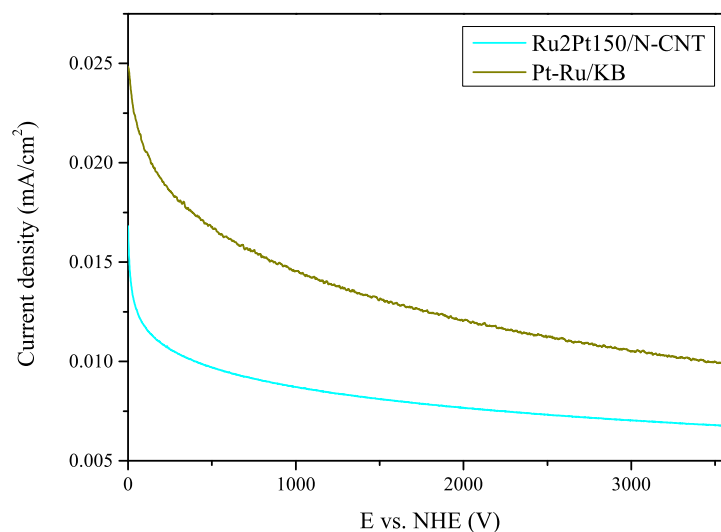
FIGURE 5.9: Chronoamperograms of Ru2Pt150/N-CNT and Pt-Ru/KB at 0.4 V for 1 h.

included in the study as a reference. Compared to the undecorated Pt catalyst, there was a significant enhancement in catalytic activity for the catalyst decorated with 1 Ru ALD cycle. This also shows that there was no nucleation delay of Ru deposition onto Pt.

Among the catalysts investigated, Ru2Pt150/N-CNT exhibited highest catalytic activity. It was also better than the Pt-Ru ALD catalysts presented in the preceding chapter. The activity of Ru2Pt150/N-CNT catalyst was compared with commercial Pt-Ru/KB (HiSPEC 12100, Johnson Matthey Fuel Cells). Pt-Ru/KB had the highest catalytic activity toward both CO oxidation and MOR. Pt-Ru/KB removed the adsorbed CO monolayer more efficiently and delivered higher methanol oxidation current density at 0.4 V than the ALD catalyst. The commercial catalyst had probably better distribution of Pt site ensembles and Ru sites, required for methanol dehydrogenation at room temperature and CO oxidation, respectively.

The following chapter deals with ALD catalysts for fuel cell applications in a Si-based DMFC.

Chapter 6

ALD Catalysts for Si-Based DMFC Applications

A passive, miniature and monolithic Si-based direct methanol fuel cell (DMFC) with porous Si as membrane support and ALD catalysts is being developed at the Department of Micro- and Nanotechnology at the Technical University of Denmark (DTU Nanotech). In this chapter the fuel cell design is presented, followed by fabrication and characterization of the anode using the three-electrode electrochemical set-up. The results have been published in [118].

6.1 DMFC design

Silicon (Si) technology has been proposed as a route for the fabrication of miniature DMFCs [43, 119–122]. In the literature the flow field plate/current collector or catalyst support is typically made of structured Si that is combined with conventional fuel cell components to make a complete fuel cell [123–128].
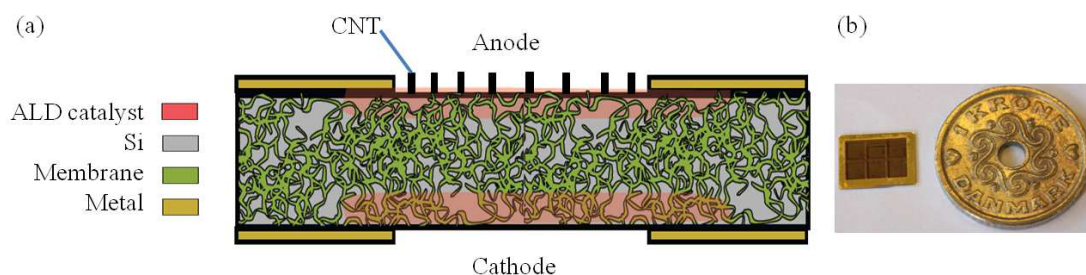
FIGURE 6.1: (a) Schematic of the Si-based DMFC. (b) Top-view photo of the Si chip beside a Danish coin with a diameter of 1 cm.
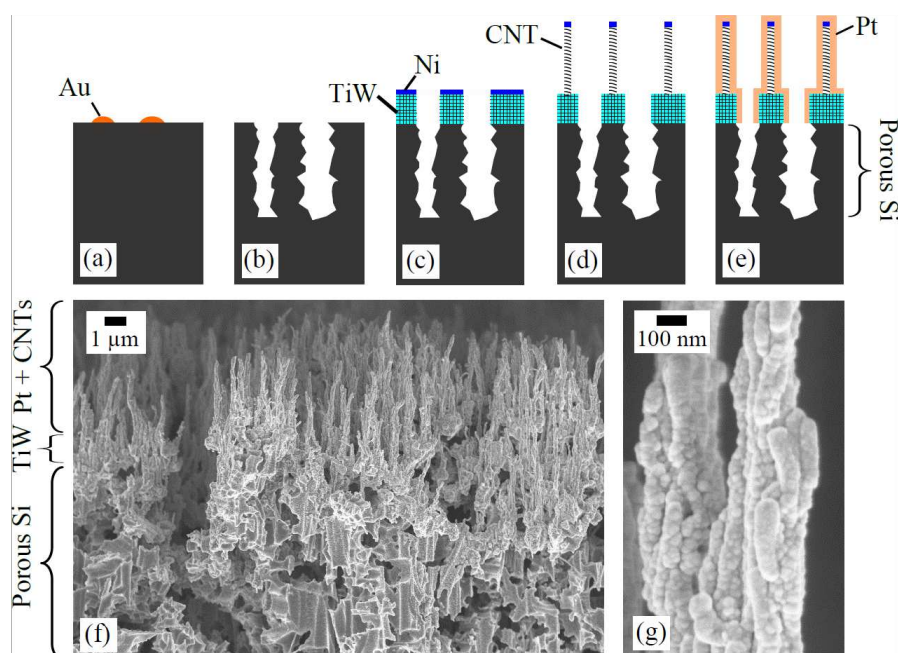
FIGURE 6.2: Fabrication of the anode: (a) 0.5 nm of Au was deposited onto Si. (b) The Si was etched, (c) followed by TiW and Ni deposition, and (d) CNT growth. (e) Pt (600 cycles) was deposited on the anode structure. (f) Cross-sectional SEM image of the top part of the anode structure, and (g) close-up SEM image of the Pt coating on the CNTs.

The fuel cell design of the DMFC being developed in this project is shown schematically in Fig. 6.1a. The Si is porous and infiltrated with Nafion, possibly having higher mechanical stability than the Nafion membrane alone [129–133]. Vertically aligned, multi-walled carbon nanotubes (CNTs) are grown directly onto the porous Si of the anode. Highly organized carbon support structures are needed in order to increase the utilization of the expensive noble metals, as well as the mass transport and electron transport within the catalyst layer [43], and vertically standing CNTs have been demonstrated as a possible approach [134–136]. ALD catalysts are deposited directly onto the anode and cathode. In this way a monolithic fuel cell can be realized [121], where all essential components are integrated into a single Si chip. Fig. 6.1b is a top-view photo of the Si chip beside a Danish coin with a diameter of 1 cm.

6.2   Fabrication of the anode

The fabrication steps of the anode are illustrated in Fig. 6.2a-e. The starting material was a single-side polished Si (100) wafer (p-doped, 1-20 $\Omega\cdot$cm, 525 µm thick). The top part of the Si (about 50 µm) was made porous by metal-assisted chemical etching (MACE) [137–139] using Au as an etch mask. 0.5 nm of Au was deposited on Si by

FIGURE 6.3: Custom-made sample holder used for electrochemical characterization of the anode in the three-electrode electrochemical set-up. (a) The stainless steel rod, (b) cover and (c) teflon mask.

electron-beam physical vapor deposition (EBPVD) through a shadow mask with rectangular openings of 0.38 cm^2, Fig. 6.2a. The Si wafer was etched at room temperature for 4 h in a solution of 400 ml of 40 wt.% HF, 400 ml of 99 wt.% C$_2$H$_5$OH and 400 ml of 30 wt.% H$_2$O$_2$, Fig. 6.2b. Vertically aligned CNTs were grown in AIXTRONs Black Magic plasma-enhanced chemical vapor deposition (PECVD) system, Fig. 6.2d. The CNTs were grown using the same recipe as those used as carbon support in Chapters 4 and 5, except for the growth temperature. Here the temperature was 750 ℃, whereas it was previously 850 ℃. Before CNT growth, the porous Si was coated with 200 nm of sputtered TiW and 7 nm of E-beam evaporated Ni, serving as the diffusion barrier and catalyst film, respectively, Fig. 6.2c. TiW and Ni were deposited onto the porous Si through the same shadow mask with rectangular openings. The wafer was diced into Si chips, followed by Pt ALD (600 cycles) onto the CNTs using the standard ALD recipe, see Table 3.1 on page 35. The final structure is shown in Fig. 6.2e and a close-up SEM image of the top part in Fig. 6.2f. The CNT bundles were approximately 3 µm long. Fig. 6.2g reveals a SEM image of the conformal Pt coating on the CNTs. 67 chips in total could be fabricated from one 4" wafer.

6.3 Electrochemical characterization

The anode, labeled Pt-CNT-TiW-pSi, was electrochemically characterized using the three-electrode electrochemical set-up, see page 13, and compared with a flat Si sample coated with Pt ALD (also 600 cycles), Pt-Si. The custom-made sample holder in Fig. 6.3 was used for the electrochemical tests. The sample to be characterized was placed onto the circular end of the stainless steel rod, Fig. 6.3a, and on top a sealing and teflon mask, Fig. 6.3c, defining the area of the Si chip to be exposed to the electrolyte. The cover, Fig. 6.3b, was then screwed on to keep the chip in place.
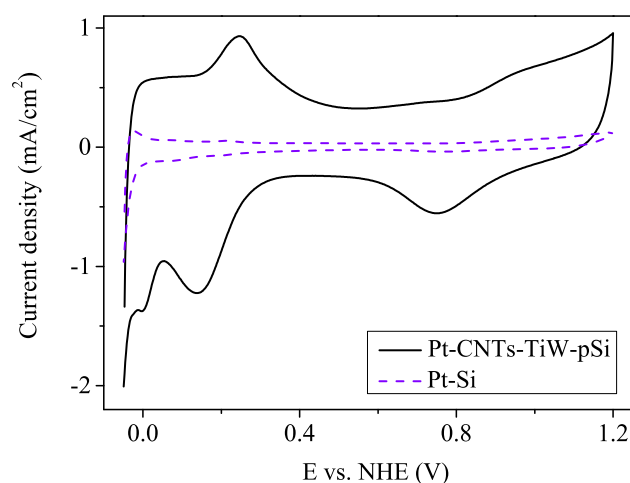
FIGURE 6.4: CVs of Pt-CNTs-TiW-pSi (solid line) and Pt-Si (dashed line) in 0.5 M H$_2$SO$_4$ at 20 mV/s. Current densities are given per geometric surface area.
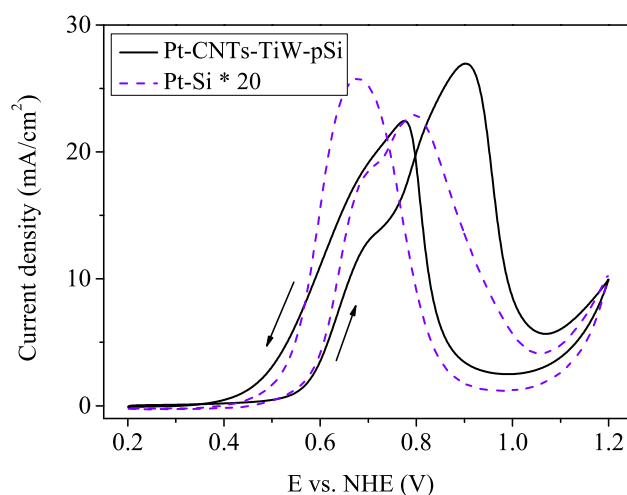
FIGURE 6.5: CVs of Pt-CNT-TiW-pSi (solid) and Pt-Si (dashed) recorded in 1.0 M CH$_3$OH + 0.5 M H$_2$SO$_4$ at 10 mV/s. The 10th cycle is plotted. Current densities are given per geometric surface area. Notice that the current density for the Pt-Si sample has been multiplied by 20.

The CVs were run first in 0.5 M H$_2$SO$_4$ from -0.05 to 1.2 V at 20 mV/s for 10 cycles. Fig. 6.4 presents CVs of Pt-CNTs-TiW-pSi and Pt-Si. In contrast to the CV plots in Chapters 4 and 5, the current here is divided by the geometric surface area of the sample. The three characteristic regions were observed for the Pt anode, i.e., the hydrogen underpotential deposition (H$_{upd}$) region, double layer region and oxidation/reduction region.

The samples were then characterized in 1.0 M CH$_3$OH + 0.5 M H$_2$SO$_4$ by conducting CV from 0.2 to 1.2 V at 10 mV/s and the 10th cycle is plotted, see Fig. 6.5. The current

Sample	Sheet resistance ($\Omega\square$)
TiW-Si	14.2
TiW-pSi	Not measurable
Pt-Si	5.7
Pt-TiW-pSi	17.1

TABLE 6.1: Sheet resistance measurements of TiW deposited on flat Si (TiW-Si) and porous Si (TiW-pSi), and Pt ALD (600 cycles) deposited on flat Si (Pt-Si) and TiW-pSi (Pt-TiW-pSi).

was divided by the geometric surface area. Due to the low activity of the Pt-Si sample, the current density has been multiplied by 20 (for illustrative purposes only), revealing that the activity of the Pt-CNTs-TiW-pSi sample is approximately 20 times higher. The two typical methanol oxidation peaks for each sample were obtained, showing that they are electrochemically active toward the MOR.

Table 6.1 summarizes sheet resistance measurements of four samples: TiW deposited on flat Si and porous Si, and Pt ALD (600 cycles) deposited on flat Si and TiW-pSi. The sheet resistance of TiW-Si was 14.2 $\Omega\square$, but the sheet resistance of TiW-pSi could not be measured, implying the coverage of the sputtered TiW film was not continuous. The same structure with Pt (Pt-TiW-pSi) was measurable and had a sheet resistance of 17.1 $\Omega\square$, which was, as expected, higher than the sheet resistance of flat Pt-Si (5.7 $\Omega\square$). The sheet resistance of the anode Pt-CNTs-TiW-pSi was not measured. However, it is expected that the anode had a somewhat higher resistance than the sample without CNTs. This statement is based on investigations in SEM where it was noticed that the Pt precursors were not able to penetrate very deep into the porous Si with CNTs. In any case, the results suggest a high active surface area and activity per geometric area for the proposed anode structure.

The Pt film in this study also functioned as the current collector. For further improvement it is suggested that a more inexpensive current collector, such as a conducting metal oxide could be used. It can then be deposited before CNT growth and also be used as the diffusion barrier during growth. Accordingly, the Pt loading could be reduced significantly. However, on the other hand, as an alternative route, the company 3M has developed a nanostructured thin film (NSTF) catalyst, consisting of a sputter-coated Pt or Pt-based thin film on organic whiskers [140–142], showing highly promising results in terms of both activity and durability. As the sheet resistance measurements indicate, film deposition onto porous Si requires excellent step coverage, and thus, ALD could be a suitable coating technique.

6.4   Summary

The nanostructured anode for the Si-based DMFC has been presented. It consists of CNTs grown on porous Si and coated with a thin Pt ALD film, functioning as the catalyst layer and current collector. The anode structure was tested electrochemically in 0.5 M H_2SO_4 and 1.0 M CH_3OH + 0.5 M H_2SO_4 and it showed 20 times higher catalytic activity compared to a Pt ALD film deposited on flat Si. There are potential advantages of the anode structure compared to conventional catalysts, such as improved Pt utilization and durability, as well as lower catalyst layer resistance. However, there is a need to find a more inexpensive current collector.

In the next chapter the Pt ALD is tested on the cathode for low-temperature solid oxide fuel cells (SOFCs).

Chapter 7

ALD of Pt on Cathodes for Low Temperature SOFCs

This chapter covers the preparation and characterization of symmetrical solid oxide fuel cell (SOFC) cathodes with Pt ALD for low temperature SOFCs (<500 ℃). Two types of cathodes were tested: $La_{0.6}Sr_{0.4}CoO_{3-\delta}$ (LSC) and LSC-infiltrated $Ce_{0.9}Gd_{0.1}O_{1.95}$ (CGO) cathodes. All cathodes had CGO as electrolyte. The work was carried out together with the Department of Energy Conversion and Storage at the Technical University of Denmark.

7.1 The SOFC cathode

There are two types of cathodes, pure electronic conductors and mixed ionic and electronic conductors (MIEC). The reaction mechanism is related to the electrode type. For pure electronic conductors oxygen is adsorbed onto the cathode and diffuses along the surface to triple-phase boundaries (TPB), where it is ionized and transferred into the electrolyte. For MIECs oxygen ions can also be incorporated into the electrode material and diffuse toward the electrode/electrolyte boundary, resulting in extended electrochemical reaction zone and reduced electrode polarization resistance.

The most commonly used cathode for SOFCs operating at temperatures higher than 800 ℃ is strontium-doped $LaMnO_3$ (LSM), an electronic conductor, and it is typically used together with an yttria-stabilized zirconia (YSZ) electrolyte. The performance of the LSM and YSZ falls quickly as the operating temperature is lowered, and they must therefore be replaced. The cathode should preferably be a MIEC and the electrolyte
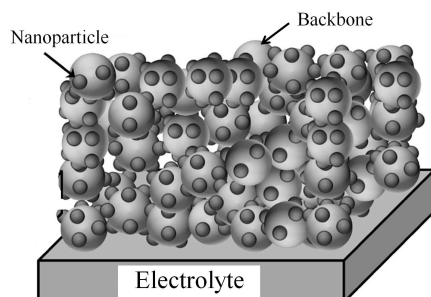
FIGURE 7.1: Schematic of the LSC-infiltrated CGO composite, adapted from [67].

should have higher ionic conductivity, as e.g., Gd-doped ceria (CGO). Further requirements have to be met in terms of catalytic activity, chemical stability and component compatibility.

Typically, MIECs have a higher ionic conductivity compared to common solid oxide electrolytes, but the conductivity drops more sharply with decreasing temperature. Therefore, composite cathodes of MIEC and high ionic conductivity phases are favored.

In this chapter Pt is deposited by ALD onto two types of cathodes, LSC and LSC-infiltrated CGO cathodes. The first is a MIEC while the second is a composite cathode. The objective is to investigate whether the electrode polarization resistance, R_p, of the various cathodes is reduced with the addition of Pt. It is tested by conducting electrochemical impedance spectroscopy (EIS) on symmetrical cathode cells.

7.2   Preparation of the symmetrical cathodes

The symmetrical LSC cathodes were prepared by screen printing an in-house LSC ink onto both sides of a dense, 300 μm thick CGO (KERAFOL, Germany), followed by firing at 930 ℃ for 24 h in air. After firing, the piece was cut into 6 x 6 mm^2 samples and Pt of various ALD cycles (20, 50, 100, and 200 cycles) was deposited onto the LSC cathodes, and one was kept uncoated as a reference.

For the symmetrical LSC-infiltrated cathodes the backbones of CGO were first prepared by screen printing an in-house CGO ink onto both sides of a CGO electrolyte. The screen-printed sample was then fired at 1150 ℃, followed by cutting in squares of 6 x 6 mm^2. The infiltration procedure is described in [67]. In short, the LSC precursor solution used for infiltration was prepared by mixing individual aqueous stock solutions of La, Sr, and Co nitrates in precise amounts to obtain the nominal composition $La_{0.6}Sr_{0.4}Co_{1.05}O_{3-\delta}$. The nitrate solution was then pipetted onto the backbones of CGO and placed under rough vacuum. This was repeated 6 times and after each infiltration
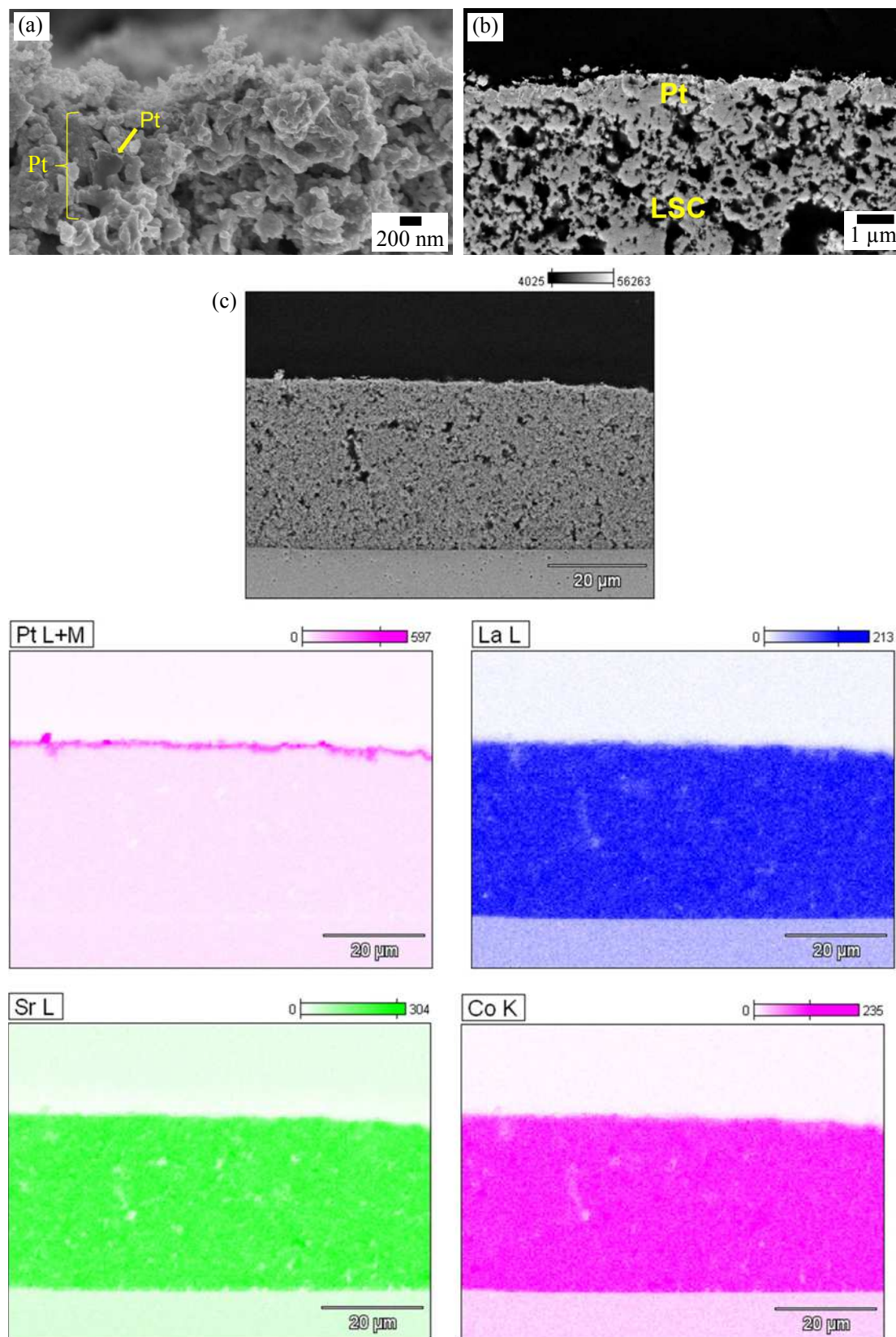
FIGURE 7.2: (a) Fractured and (b) polished cross-sectional SEM images of the top part of the LSC cathode coated with 200 cycles of Pt. (c) EDX elemental mapping images of Pt, La, Sr and Co for the LSC cathode deposited with Pt (200 cycles), revealing that Pt is deposited onto the uppermost part.
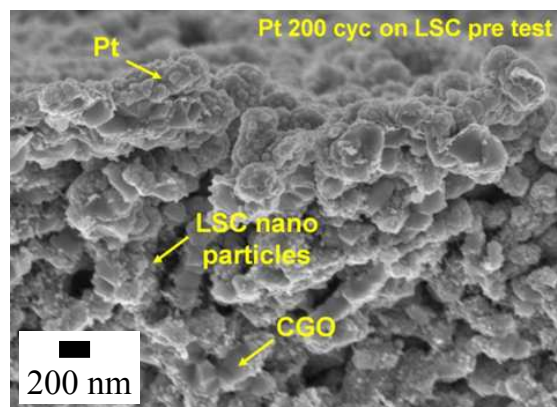
FIGURE 7.3: Fractured cross-sectional SEM image of the top part of the LSC-infiltrated CGO cathode after Pt deposition (200 cycles).

the samples were pre-calcined at 350 ℃ for 1 h. A schematic of the LSC-infiltrated CGO cathode on electrolyte is shown in Fig. 7.1. The LSC-infiltrated samples were then fired at 600 ℃, as this temperature resulted in cathodes with lowest electrode polarization resistance, R_p, [67]. 200 cycles of Pt was subsequently deposited onto the symmetric cells, and one was kept uncoated as a reference. For comparison, porous CGO backbone samples without LSC infiltration, with and without 200 cycles of Pt, were also prepared and tested as references.

7.3   Physical characterization

Fractured and polished cross-sectional SEM images of the LSC cathode coated with 200 cycles of Pt are shown in Fig. 7.2a and b, respectively. It appears that the top 0.5-1.0 µm layer has been coated. The observation is further supported by energy dispersive spectroscopy (EDX) of the polished cathode. Fig. 7.2c shows the EDX elemental mapping images for Pt, La, Sr and Co. Pt is only acquired at the uppermost part, whereas La, Sr, and Co are detected throughout the entire volume.

SEM image of the LSC-infiltrated CGO cathode after Pt deposition is shown in Fig. 7.3. Similar to the LSC cathode, this structure is also relatively dense and it can be assumed that Pt is deposited at the uppermost part of the cathode, although it is not clear in the SEM image.

FIGURE 7.4: Complex plane plots in air at 400 ℃ under varying maximum firing temperatures, T_{max}, and varying Pt ALD cycles. (a) LSC reference, LSC cathode with (b) 20 cycles of Pt, (c) 50 cycles of Pt, (d) 100 cycles of Pt and (e) 200 cycles of Pt.
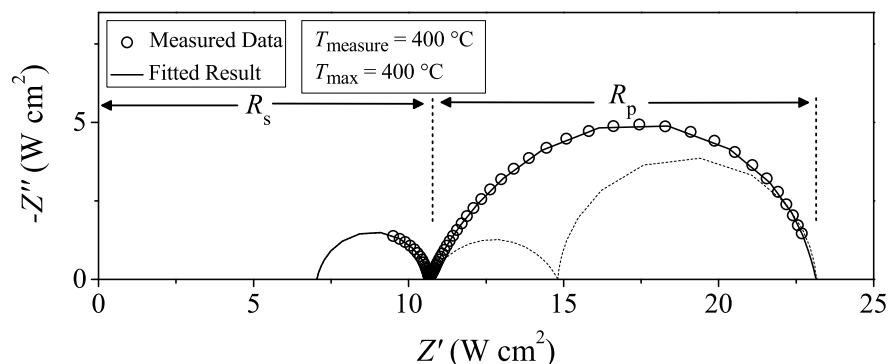
FIGURE 7.5: Impedance spectrum of the LSC cathode with 200 cycles of Pt measured at 400 ℃ ($T_{max} = 400$ ℃) together with the fit.
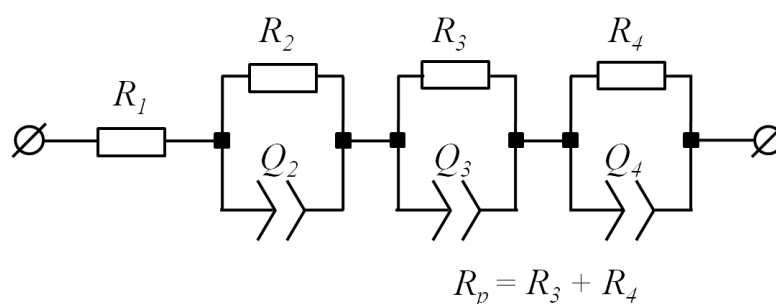
FIGURE 7.6: The equivalent-circuit model used to fit the impedance data. Polarization resistance R_p is equivalent to the sum of R_3 and R_4.

7.4   EIS

For the EIS measurements a Hioki 3522-50 impedance analyzer was used. The frequency range was set from 60 mHz to 100 kHz under open circuit conditions with a 50 mV amplitude AC signal. The performance with varying firing temperatures was investigated by heating the samples *in-situ* at different maximum temperatures, T_{max}, starting from either 400 or 600 to 900 ℃, increasing each time by 100 ℃. Impedance measurements were acquired at 400 or 600 ℃ in between and were divided by two to account for two electrodes in series and normalized by the geometrical area of the sample. Furthermore, the data were corrected for the series inductance of the measurement rig, determined by measurements of the set-up without any samples.

The complex plane plots at 400 ℃ of the LSC cathodes under varying T_{max}, and varying ALD cycles of Pt deposited are shown in Fig. 7.4. R_p can be obtained by fitting the impedance spectra using the equivalent-circuit model as shown in Fig. 7.6. R represents the resistance and Q is a constant phase element. Fig. 7.5 shows the impedance spectra of the cathode with 200 cycles of Pt measured at 400 ℃ ($T_{max} = 400$ ℃) together with the fit. No attempt was made to interpret the processes associated with each RQ
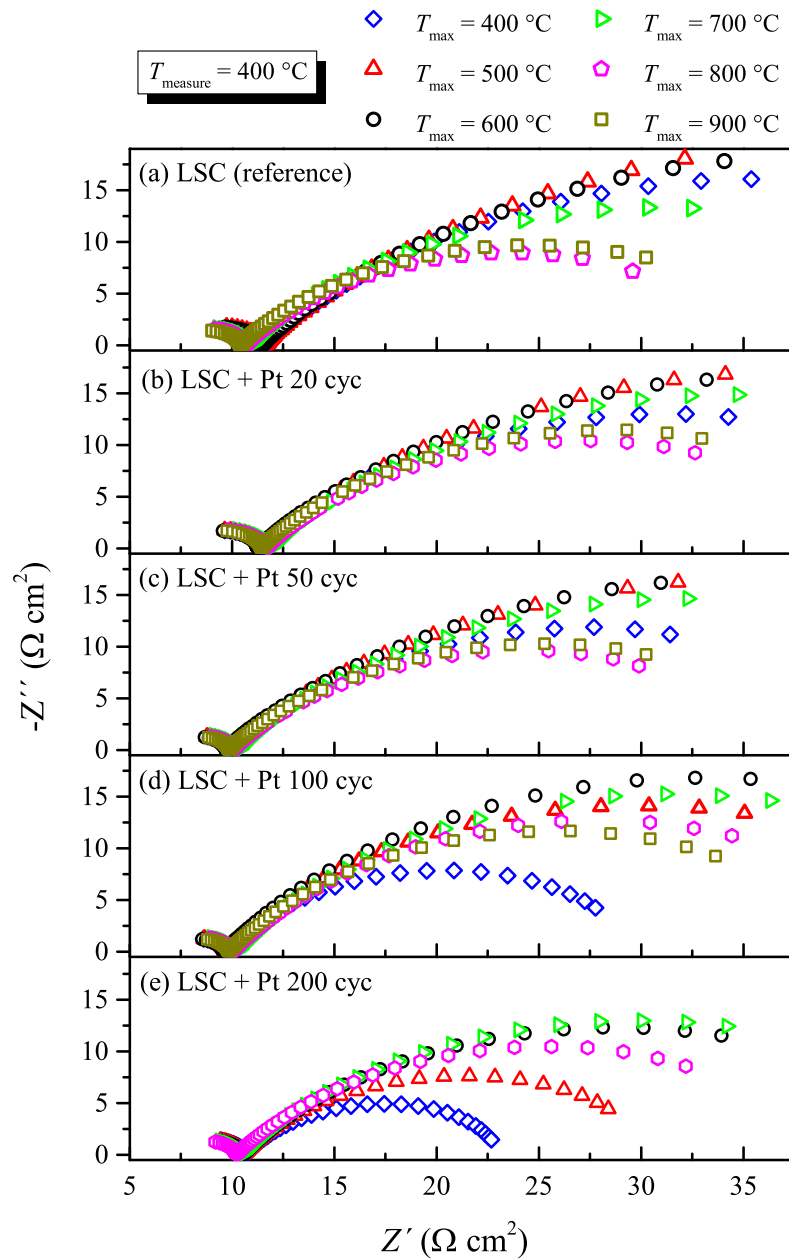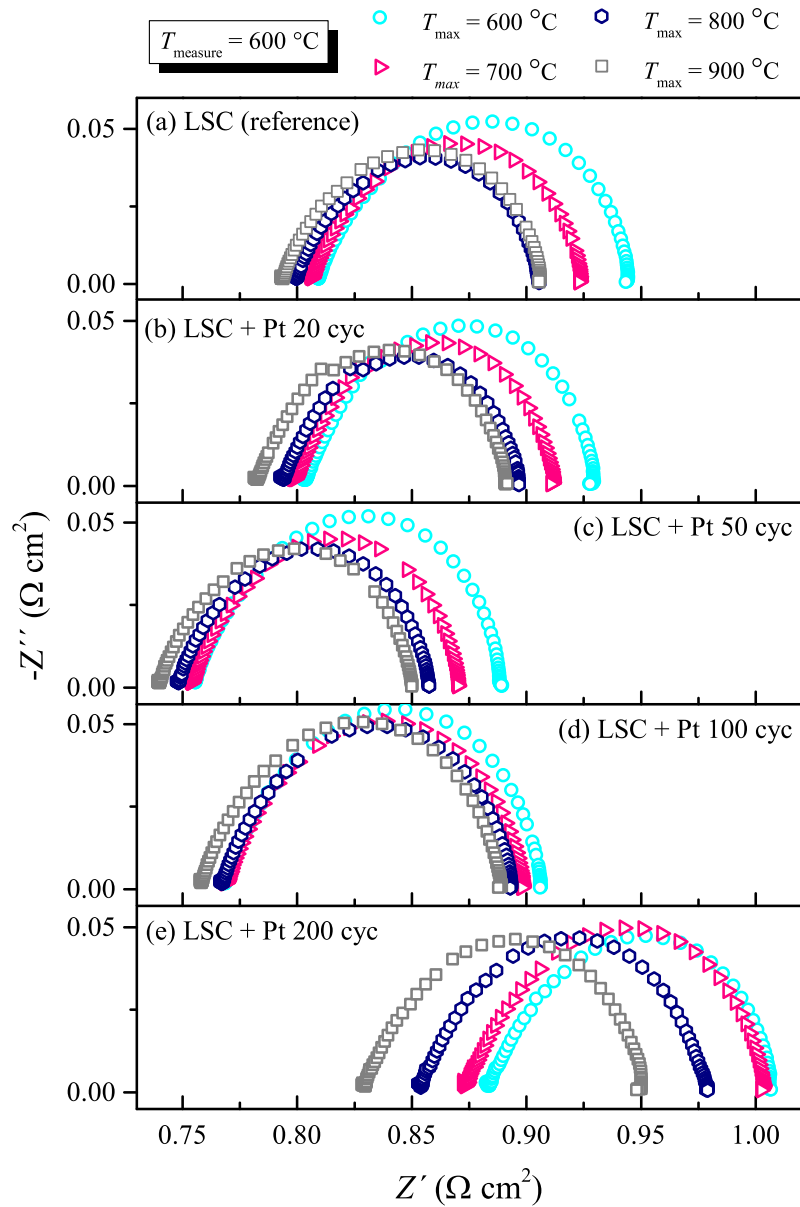
FIGURE 7.7: Complex plane plots in air at 600 ℃ under varying maximum firing temperatures, T_{max}, and varying Pt ALD cycles. (a) LSC reference, LSC cathode with (b) 20 cycles of Pt, (c) 50 cycles of Pt, (d) 100 cycles of Pt and (e) 200 cycles of Pt.
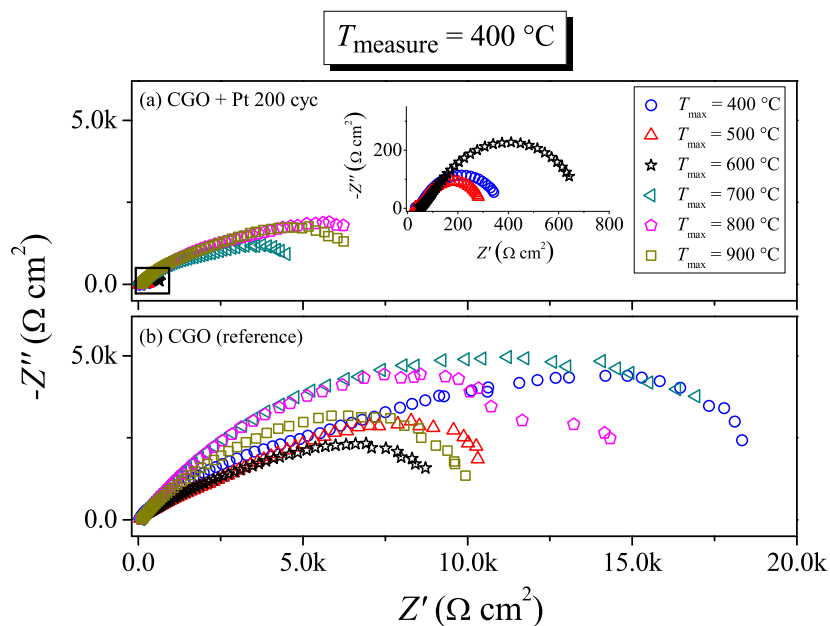
FIGURE 7.8: Complex plane plots in air at 400 ℃ under varying maximum Pt firing temperatures, T_{max}, for CGO samples (a) with 200 cycles of Pt and (b) without. Plots acquired after $T_{max} = 400$, 500 and 600 ℃ for CGO + Pt 200 cycles are plotted in the inset.
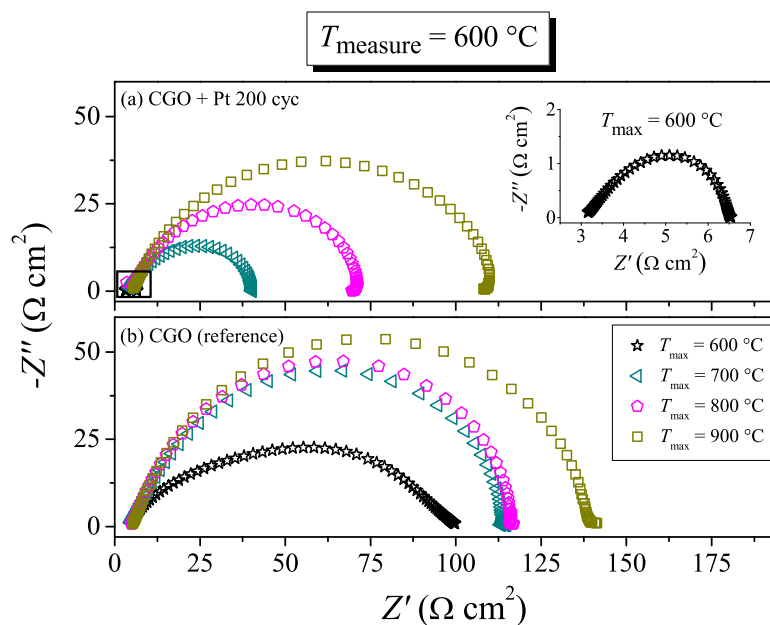
FIGURE 7.9: Complex plane plots in air at 600 ℃ under varying maximum Pt firing temperatures, T_{max}, for CGO samples (a) with 200 cycles of Pt and (b) without. Plot acquired after $T_{max} = 600$ ℃ for CGO + Pt 200 cycles is plotted in the inset.
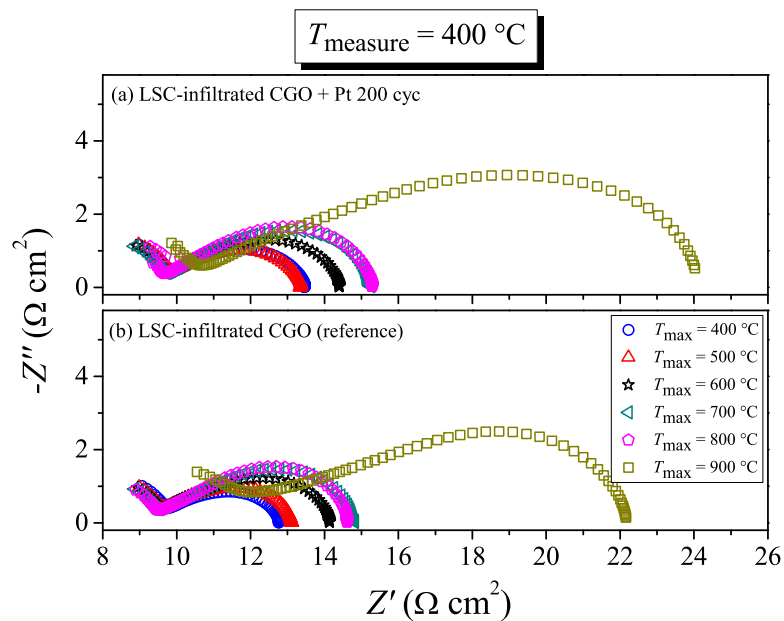
FIGURE 7.10: Complex plane plots in air at 400 ℃ under varying maximum firing temperatures, T_{max}, for LSC-infiltrated CGO cathodes (a) with 200 cycles of Pt and (b) without.
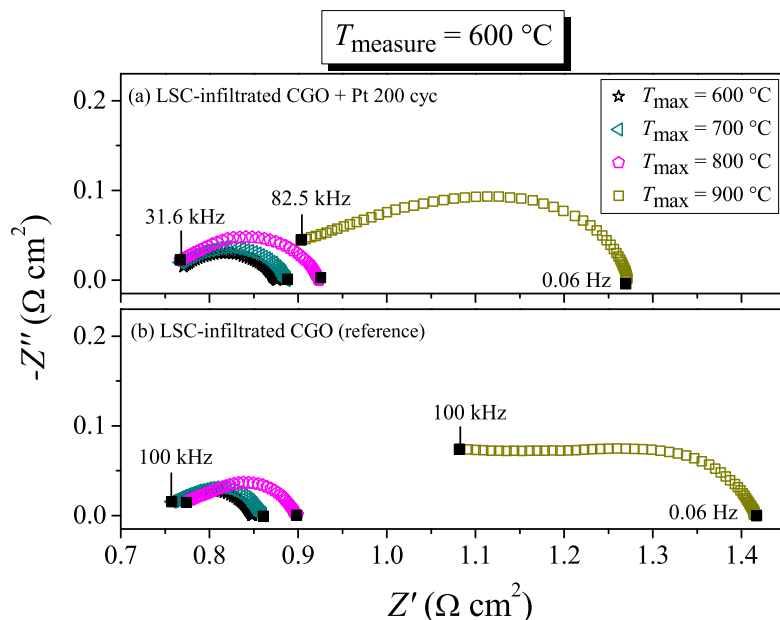
FIGURE 7.11: Complex plane plots in air at 600 ℃ under varying maximum Pt firing temperatures, T_{max}, for LSC-infiltrated CGO cathodes (a) with 200 cycles of Pt and (b) without.

	R_p (Ω cm^2) $T_{\text{measure}} = 400$ ℃ $T_{\text{max}} = 400$ ℃	R_p (Ω cm^2) $T_{\text{measure}} = 600$ ℃ $T_{\text{max}} = 600$ ℃
LSC reference	47	0.14
LSC + Pt 200 cyc	12	0.13
CGO reference	22574	88
CGO + Pt 200 cyc	329	3.4
LSC-inf. CGO reference	3.2	0.13
LSC-inf. CGO + Pt 200 cyc	4.5	0.12

TABLE 7.1: Summary of the electrode polarization resistance, R_p, values for the LSC and LSC-infiltrated cathodes and CGO electrolyte, both with and without 200 cycles of Pt.

elements. However, it can be said that $R_3 Q_3$ and $R_4 Q_4$ represent electrode processes as also discussed in [143]. Thus, the sum of R_3 and R_4 is R_p.

As seen in Fig. 7.4, R_p is reduced with increasing number of Pt ALD cycles, and the trend is most pronounced for low T_{max}. It is not clear why R_p is reduced, considering that Pt is located on the topmost part of the cathode. The Pt particles must be very catalytically active. The transport of oxide ions is not clear as the resistance associated with the ionic transport in LSC would be high at 400 ℃. It can be speculated that transport via surface diffusion is a possibility. At $T_{\text{measure}} = 600$ ℃, Fig. 7.7, no significant difference in R_p was observed for any of the samples.

Shown in Fig. 7.8 and 7.9 are the Nyquist plots at 400 and 600 ℃, respectively, of non-infiltrated CGO with and without Pt deposition (200 cycles). A considerable decrease in resistance was found with the addition of Pt, and especially at low T_{max}. In this case, Pt functioned solely as the cathode.

The complex plane plots at 400 and 600 ℃ of the LSC-infiltrated CGO cathodes with and without 200 cycles of Pt are plotted in Fig. 7.10 and 7.11, respectively. The performance was not improved by the addition of Pt. The cathode was probably good enough that the Pt had negligible effect. Modifications on either or both the backbone structure and the Pt deposition could be performed to optimize the penetration of Pt.

The R_p values for the various cathodes and electrolyte with and without 200 cycles of Pt are summarized in Table 7.1. The data were extracted for $T_{\text{measure}} = T_{\text{max}} = 400$ ℃ and $T_{\text{measure}} = T_{\text{max}} = 600$ ℃.

7.5   Summary

Pt of various ALD cycle numbers (20, 50, 100 and 200) was deposited onto symmetrical LSC cathodes, and 200 cycles of Pt were deposited onto symmetrical LSC-infiltrated CGO cathodes, as well as on CGO backbone cells. The structure of all cathodes was dense, not allowing Pt precursor vapors to penetrate deep into the structure using the standard ALD recipe. The symmetrical cells were tested using EIS. The CGO backbone cells with added Pt showed enhanced performance at firing temperatures up to 800 ℃ as Pt functioned as the electronic conductor in those configurations. The LSC cathodes with Pt had reduced polarization resistance at low firing temperatures, and the resistance was reduced with increased Pt loading. The polarization resistance of the best cathode, the LSC-infiltrated CGO cathode, was not lowered by the addition of Pt at any firing temperatures.

Chapter 8

Conclusion and Outlook

The PhD dissertation is a contribution to the relatively unexplored research field of atomic layer deposited (ALD) catalysts for use in e.g., miniature fuel cells.

Pt and Ru ALD processes were first established using a hot-wall, flow-type ALD reactor from Picosun (Sunale R-150). The Pt and Ru precursors were MeCpPtMe$_3$ and Ru(EtCp)$_2$, respectively, and O$_2$ the reactant in both processes. The noble metal films were pure, polycrystalline and had low resistivity.

Nitrogen-doped multi-walled carbon nanotubes (N-CNTs), grown in a PECVD, were used as the carbon support material for the ALD catalysts. The N-CNTs were chemically active, i.e., no pre-treatment was necessary prior to ALD. Both Pt and Ru growth initiate as particles onto the carbon support. The particles were highly dispersed and their size was easily adjusted by the number of ALD cycles applied. The Pt particles were polycrystalline, confirmed using XRD. However, the XRD peak intensities from the Ru particles were low, indicating a lack of crystallinity.

Accelerated durability tests were performed on N-CNT supported Pt particles using a three-electrode electrochemical set-up. Pt ALD catalysts of similar size to commercial Pt/KB (HiSPEC 13100, Johnson Matthey Fuel Cells) exhibited higher durability. The enhancement was addressed to the carbon support and its nitrogen doping.

Two ALD catalyst/N-CNT series were evaluated toward the CO oxidation and the methanol oxidation reaction (MOR). The first series consisted of five Pt-Ru catalysts of various Ru compositions between 0 and 100 at.%. For the compositions investigated, the catalyst containing 29 at.% Ru showed highest catalytic activity. The second series was Pt particles decorated with various loadings of Ru, i.e., various Ru ALD cycles (1, 2, 5, 10 and 20). The Pt catalyst decorated with 2 Ru ALD cycles exhibited highest catalytic activity, which was also higher than that for the best catalyst in the first series.

It is clear from the measurements carried out that Ru enhances the activity significantly via the bifunctional mechanism, and maybe also via the ligand effect. Further investigations to optimize and improve the performance of the ALD catalysts are needed in order to compete with commercially available ones (Pt-Ru/KB, HiSPEC 12100, Johnson Matthey Fuel Cells). For future work, it would be interesting to investigate the effect on the catalytic activity of catalysts deposited at higher temperatures or with post-deposition annealing.

Very little research has been conducted on fuel cell performance that utilizes ALD synthesized catalysts, and no reports on direct methanol fuel cell (DMFC) tests have been found in the literature. Highly organized catalyst support structures have been suggested in order to increase the utilization of the expensive noble metals, as well as the mass transport and electron transport within the catalyst layer. One approach could be to grow vertically-aligned carbon nanotubes on carbon paper, followed by catalyst deposition using ALD.

The compatibility of ALD in Si technology makes it a suitable catalyst deposition technique, e.g., in the fabrication of a micro DMFC for portable applications. ALD may also be useful in solid oxide fuel cells (SOFCs) in order to lower the cathode polarization resistance by depositing Pt onto the cathode. The cathodes that were investigated in this thesis were too dense, not allowing Pt precursors to penetrate deep into the structure. For future experiments it would be interesting to modify either or both the porosity of the cathode or the Pt ALD procedures.

Bibliography

[1] R. L. Puurunen. Surface chemistry of atomic layer deposition: A case study for the trimethylaluminum/water process. *J Appl Phys*, 97(12):121301, 2005.

[2] R. B. Yang. *Gas-phase synthesis of bismuth and antimony chalcogenide nanostructures*. PhD thesis, Ruhr-University Bochum, 2010.

[3] D. Gu, H. Baumgart, K. Tapily, P. Shrestha, G. Namkoong, X. Ao, and F. Müller. Precise control of highly ordered arrays of nested semiconductor/metal nanotubes. *Nano Res*, 4(2):164–170, 2011.

[4] C. F. Herrmann, F. H. Fabreguette, D. S. Finch, R. Geiss, and S. M. George. Multilayer and functional coatings on carbon nanotubes using atomic layer deposition. *Appl Phys Lett*, 87(12):1–3, 2005.

[5] M. J. Weber, A. J. M. Mackus, M. A. Verheijen, C. van der Marel, and W. M. M. Kessels. Supported core/shell bimetallic nanoparticles synthesis by atomic layer deposition. *Chem Mater*, 24(15):2973–2977, 2012.

[6] V. Miikkulainen, M. Leskelä, M. Ritala, and R. L. Puurunen. Crystallinity of inorganic films grown by atomic layer deposition: Overview and general trends. *J Appl Phys*, 113(2):021301, 2013.

[7] P. Poodt, D. C. Cameron, E. Dickey, S. M. George, V. Kuznetsov, G. N. Parsons, F. Roozeboom, G. Sundaram, and A. Vermeer. Spatial atomic layer deposition: A route towards further industrialization of atomic layer deposition. *J Vac Sci Technol A*, 30(1):010802, 2012.

[8] N. Pinna and M. Knez, editors. *Atomic Layer Deposition of Nanostructured Materials*. Wiley-VCH, Weinheim, 2012.

[9] F. Wu, J. Wu, S. Banerjee, P. Banerjee, and O. Blank. Frontiers in applied atomic layer deposition (ALD) research. *Mater Sci Forum*, 736:147–182, 2013.

[10] J. Zhang, editor. *PEM Fuel Cell Electrocatalysts and Catalyst Layers - Fundamentals and Applications.* Springer, London, 2010.

[11] O. A. Petrii. Pt-Ru electrocatalysts for fuel cells: A representative review. *J Solid State Electrochem*, 12(5):609–642, 2008.

[12] S. Rojas, M. V. Martinez-Huerta, and M. A. Pena. Supported metals for application in fuel cells. *Catal Sci Ser*, 11:407–492, 2012.

[13] H. Liu, C. Song, L. Zhang, J. Zhang, H. Wang, and D. P. Wilkinson. A review of anode catalysis in the direct methanol fuel cell. *J Power Sources*, 155(2):95–110, 2006.

[14] E. Antolini. Carbon supports for low-temperature fuel cell catalysts. *Appl Catal B: Environ*, 88(1-2):1–24, 2009.

[15] S. D. Thompson, L. R. Jordan, and M. Forsyth. Platinum electrodeposition for polymer electrolyte membrane fuel cells. *Electrochim Acta*, 46(10-11):1657–1663, 2001.

[16] S. Sharma and B. G. Pollet. Support materials for PEMFC and DMFC electrocatalysts - A review. *J Power Sources*, 208:96–119, 2012.

[17] S. Basri, S. K. Kamarudin, W. R. W. Daud, and Z. Yaakub. Nanocatalyst for direct methanol fuel cell (DMFC). *Int J Hydrogen Energy*, 35(15):7957–7970, 2010.

[18] X. Wang, W. Li, Z. Chen, M. Waje, and Y. Yan. Durability investigation of carbon nanotube as catalyst support for proton exchange membrane fuel cell. *J Power Sources*, 158(1):154–159, 2006.

[19] Y. Shao, G. Yin, Y. Gao, and P. Shi. Durability study of Pt/C and Pt/CNTs catalysts under simulated PEM fuel cell conditions. *J Electrochem Soc*, 153(6): A1093–A1097, 2006.

[20] Y. Shao, G. Yin, and Y. Gao. Understanding and approaches for the durability issues of Pt-based catalysts for PEM fuel cell. *J Power Sources*, 171(2):558–566, 2007.

[21] M. Watanabe and S. Motoo. Electrocatalysis by ad-atoms. 2. Enhancement of oxidation of methanol on platinum by ruthenium ad-atoms. *J Electroanal Chem*, 60(3):267–273, 1975.

[22] T. Iwasita, F. C. Nart, and W. Vielstich. An FTIR study of the catalytic activity of a 85:15 Pt:Ru alloy for methanol oxidation. *Ber. Bunsenges. Phys. Chem.*, 94 (9):1030–1034, 1990.

[23] J. S. Spendelow, P. K. Babu, and A. Wieckowski. Electrocatalytic oxidation of carbon monoxide and methanol on platinum surfaces decorated with ruthenium. *Curr Op in Solid State Mater Sci*, 9(1-2):37–48, 2005.

[24] J. S. King, A. Wittstock, J. Biener, S. O. Kucheyev, Y. M. Wang, T. F. Baumann, S. K. Giri, A. V. Hamza, M. Baeumer, and S. F. Bent. Ultralow loading Pt nanocatalysts prepared by atomic layer deposition on carbon aerogels. *Nano Lett*, 8(8):2405–2409, 2008.

[25] S. Sun, G. Zhang, N. Gauquelin, N. Chen, J. Zhou, S. Yang, W. Chen, X. Meng, D. Geng, M. N. Banis, R. Li, S. Ye, S. Knights, G. A. Botton, T.-K. Sham, and X. Sun. Single-atom catalysis using Pt/graphene achieved through atomic layer deposition. *Sci Rep*, 3:1775, 2013.

[26] A. A. Dameron, S. Pylypenko, J. B. Bult, K. C. Neyerlin, C. Engtrakul, C. Bochert, G. J. Leong, S. L. Frisco, L. Simpson, H. N. Dinh, and B. Pivovar. Aligned carbon nanotube array functionalization for enhanced atomic layer deposition of platinum electrocatalysts. *Appl Surf Sci*, 258(13):5212–5221, 2012.

[27] J. Li, X. Liang, D. M. King, Y.-B. Jiang, and A. W. Weimer. Highly dispersed Pt nanoparticle catalyst prepared by atomic layer deposition. *Appl Catal B: Environ*, 97:220–226, 2010.

[28] C.-Y. Su, Y.-C. Hsueh, C.-C. Kei, C.-T. Lin, and T.-P. Perng. Fabrication of high-activity hybrid Pt@ZnO catalyst on carbon cloth by atomic layer deposition for photoassisted electro-oxidation of methanol. *J Phys Chem C*, 117(22):11610–11618, 2013.

[29] J. Xie, X. Yang, B. Han, Y. Shao-Horn, and D. Wang. Site-selective deposition of twinned platinum nanoparticles on TiSi$_2$ nanonets by atomic layer deposition and their oxygen reduction activities. *ACS Nano*, 2013. doi: 10.1021/nn402385f.

[30] I. J. Hsu, D. A. Hansgen, B. E. McCandless, B. G. Willis, and J. G. Chen. Atomic layer deposition of Pt on tungsten monocarbide (WC) for the oxygen reduction reaction. *J Phys Chem C*, 115(9):3709–3715, 2011.

[31] R. R. Hoover and Y. V. Tolmachev. Electrochemical properties of Pt coatings on Ni prepared by atomic layer deposition. *J Electrochem Soc*, 156(1):A37–A43, 2009.

[32] S. T. Christensen, H. Feng, J. L. Libera, N. Guo, J. T. Miller, P. C. Stair, and J. W. Elam. Supported Ru-Pt bimetallic nanoparticle catalysts prepared by atomic layer deposition. *Nano Lett*, 10(8):3047–3051, 2010.

[33] X. Jiang, T. M. Gür, F. B. Prinz, and S. F. Bent. Atomic layer deposition (ALD) co-deposited Pt-Ru binary and Pt skin catalysts for concentrated methanol oxidation. *Chem Mater*, 22(10):3024–3032, 2010.

[34] X. Meng, Y. Zhong, Y. Sun, M. N. Banis, R. Li, and X. Sun. Nitrogen-doped carbon nanotubes coated by atomic layer deposited SnO_2 with controlled morphology and phase. *Carbon*, 49(4):1133–1144, 2011.

[35] H.-B.-R. Lee and S. F. Bent. Microstructure-dependent nucleation in atomic layer deposition of Pt on TiO_2. *Chem Mater*, 24(2):279–286, 2012.

[36] L. F. Hakim, S. M. George, and A. W. Weimer. Conformal nanocoating of zirconia nanoparticles by atomic layer deposition in a fluidized bed reactor. *Nanotechnol*, 16(7):S375–S381, 2005.

[37] J. R. Wank, S. M. George, and A. W. Weimer. Nanocoating individual cohesive boron nitride particles in a fluidized bed by ALD. *Powder Technol*, 142(1):59–69, 2004.

[38] J. A. McCormick, B. L. Cloutier, A. W. Weimer, and S. M. George. Rotary reactor for atomic layer deposition on large quantities of nanoparticles. *J Vac Sci Technol A*, 25(1):67–74, 2007.

[39] J. A. McCormick, K. P. Rice, D. F. Paul, A. W. Weimer, and S. M. George. Analysis of Al_2O_3 atomic layer deposition on ZrO_2 nanoparticles in a rotary reactor. *Chem Vap Dep*, 13(9):491–498, 2007.

[40] A. S. Cavanagh, C. A. Wilson, A. W. Weimer, and S. M. George. Atomic layer deposition on gram quantities of multi-walled carbon nanotubes. *Nanotechnol*, 20 (25):255602, 2009.

[41] G.-D. Zhan, X. Du, D. M. King, L. F. Hakim, X. Liang, J. A. McCormick, and A. W. Weimer. Atomic layer deposition on bulk quantities of surfactant-modified single-walled carbon nanotubes. *J Am Ceram Soc*, 91(3):831–835, 2008.

[42] A. S. Aricò, S. Srinivasan, and V. Antonucci. DMFCs: From fundamental aspects to technology development. *Fuel Cells*, 1(2):133–161, 2001.

[43] S. Sundarrajan, S. I. Allakhverdiev, and S. Ramakrishna. Progress and perspectives in micro direct methanol fuel cell. *Int J Hydrogen Energy*, 37(10):8765–8786, 2012.

[44] J. H. Hales, C. Kallesøe, T. Lund-Olesen, A.-C. Johansson, H. C. Fanøe, Y. Yu, P. B. Lund, A. L. Vig, O Tynelius, and L. H. Christensen. Micro fuel cells power the hearing aids of the future. *Fuel Cells Bull*, 2012(12):12–16, 2012.

[45] T. S. Zhao, R. Chen, W. W. Yang, and C. Xu. Small direct methanol fuel cells with passive supply of reactants. *J Power Sources*, 191(2):185–202, 2009.

[46] A. Evans, A. Bieberle-Hütter, J. L. M. Rupp, and L. J. Gauckler. Review on microfabricated micro-solid oxide fuel cell membranes. *J Power Sources*, 194(1): 119–129, 2009.

[47] A. Bieberle-Hütter, D. Beckel, A. Infortuna, U. P. Muecke, J. L. M. Rupp, L. J. Gauckler, S. Rey-Mermet, P. Muralt, N. R. Bieri, N. Hotz, M. J. Stutz, D. Poulikakos, P. Heeb, P. Müller, A. Bernard, R. Gmür, and T. Hocker. A micro-solid oxide fuel cell system as battery replacement. *J Power Sources*, 177 (1):123–130, 2008.

[48] M. Cassir, A. Ringuedé, and L. Niinistö. Input of atomic layer deposition for solid oxide fuel cell applications. *J Mater Chem*, 20(41):8987–8993, 2010.

[49] J. W. Elam, N. P. Dasgupta, and F. B. Prinz. ALD for clean energy conversion, utilization, and storage. *MRS Bull*, 36(11):899–906, 2011.

[50] T. P. Holme, C. Lee, and F. B. Prinz. Atomic layer deposition of LSM cathodes for solid oxide fuel cells. *Solid State Ion*, 179(27-32):1540–1544, 2008.

[51] J. An, Y.-B. Kim, and F. B. Prinz. Ultra-thin platinum catalytic electrodes fabricated by atomic layer deposition. *Phys Chem*, 15(20):7520–7525, 2013.

[52] X. Jiang, H. Huang, F. B. Prinz, and S. F. Bent. Application of atomic layer deposition of platinum to solid oxide fuel cells. *Chem Mater*, 20(12):3897–3905, 2008.

[53] J. H. Shim, X. Jiang, S. F. Bent, and F. B. Prinz. Catalysts with Pt surface coating by atomic layer deposition for solid oxide fuel cells. *J Electrochem Soc*, 157(6):B793–B797, 2010.

[54] C.-C. Chao, M. Motoyama, and F. B. Prinz. Nanostructured platinum catalysts by atomic-layer deposition for solid-oxide fuel cells. *Adv Energy Mater*, 2(6):651–654, 2012.

[55] J. An, Y.-B. Kim, T. M. Gür, and F. B. Prinz. Enhancing charge transfer kinetics by nanoscale catalytic cermet interlayer. *ACS Appl Mater Interfaces*, 4(12):6789–6794, 2012.

[56] Southampton Electrochemistry Group. *Instrumental Methods in Electrochemistry*. Horwood Publishing, Chichester, 2001.

[57] V. Stamenković, B. B. Blizanac, B. Grgur, and N. M. Marković. Electrocatalysis of fuel cells reaction on Pt and Pt-bimetallic anode catalysts: A selective review. *Chem Ind*, 56(6):273–286, 2002.

[58] H. Liu and J. Zhang, editors. *Electrocatalysis of Direct Methanol Fuel Cells - From Fundamentals to Applications*. Wiley-VCH, Weinheim, 2009.

[59] H. A. Gasteiger, N. M. Marković, and P. N. Ross Jr. H_2 and CO electrooxidation on well-characterized Pt, Ru, and Pt-Ru. 1. Rotating disk electrode studies of the pure gases including temperature effects. *J Phys Chem*, 99(20):8290–8301, 1995.

[60] H. A. Gasteiger, N. Marković, P. N. Ross Jr., and E. J. Cairns. CO electrooxidation on well-characterized Pt-Ru alloys. *J Phys Chem*, 98(2):617–625, 1994.

[61] G. Siné, I. Duo, B. E. Roustom, G. Fóti, and C. Comninellis. Deposition of clusters and nanoparticles onto boron-doped diamond electrodes for electrocatalysis. *J Appl Electrochem*, 36(8):847–862, 2006.

[62] K. J. J. Mayrhofer, D. Strmcnik, B. B. Blizanac, V. Stamenkovic, M. Arenz, and N. M. Markovic. Measurement of oxygen reduction activities via the rotating disc electrode method: From Pt model surfaces to carbon-supported high surface area catalysts. *Electrochim Acta*, 53(7):3181–3188, 2008.

[63] A. Kabbabi, R. Faure, R. Durand, B. Beden, F. Hahn, J.-M. Léger, and C. Lamy. In situ FTIRS study of the electrocatalytic oxidation of carbon monoxide and methanol at platinum-ruthenium bulk alloy electrodes. *J Electroanal Chem*, 444 (1):41–53, 1998.

[64] S.-Y. Huang, P. Ganesan, and B. N. Popov. Electrocatalytic activity and stability of niobium-doped titanium oxide supported platinum catalyst for polymer electrolyte membrane fuel cells. *Appl Catal B: Environ*, 96(1-2):224–231, 2010.

[65] J. Wu, F. Xia, M. Pan, and X.-D. Zhou. Oxygen reduction reaction on active and stable nanoscale $TiSi_2$ supported electrocatalysts. *J Electrochem Soc*, 159(6): B654–B660, 2012.

[66] F. Hasche, M. Oezaslan, and P. Strasser. Activity, structure and degradation of dealloyed $PtNi_3$ nanoparticle electrocatalyst for the oxygen reduction reaction in PEMFC. *J Electrochem Soc*, 159(1):B25–B34, 2012.

[67] A. J. Samson. *Cathodes for solid oxide fuel cells operating at low temperatures*. PhD thesis, Technical University of Denmark, 2012.

[68] X.-Z. Yuan, C. Song, H. Wang, and J. Zhang. *Electrochemical Impedance Spectroscopy in PEM Fuel Cells - Fundamentals and Application.* Springer, London, 2010.

[69] A.-C. Johansson, R. B. Yang, K. B. Haugshøj, J. V. Larsen, L. H. Christensen, and E. V. Thomsen. Ru-decorated Pt nanoparticles on N-doped multi-walled carbon nanotubes by atomic layer deposition for direct methanol fuel cells. *Int J Hydrogen Energy*, 38(26):11406–11414, 2013.

[70] T. Aaltonen, M. Ritala, T. Sajavaara, J. Keinonen, and M. Leskelä. Atomic layer deposition of platinum thin films. *Chem Mater*, 15(9):1924–1928, 2003.

[71] T. Aaltonen, A. Rahtu, M. Ritala, M. Leskelä, and A. Rahtu. Reaction mechanism studies on atomic layer deposition of ruthenium and platinum. *Electrochem Solid-State Lett*, 6(9):C130–C133, 2003.

[72] T. Aaltonen, P. Alén, M. Ritala, and M. Leskelä. Ruthenium thin films grown by atomic layer deposition. *Adv Mater*, 15(1):45–49, 2003.

[73] T. Aaltonen, M. Ritala, M. Leskelä, K. Arstila, and J. Keinonen. Atomic layer deposition of ruthenium thin films from Ru(thd)$_3$ and oxygen. *Chem Vapor Dep*, 10(4):215–219, 2004.

[74] T. Aaltonen, M. Ritala, Y.-L. Tung, Y. Chi, K. Arstila, K. Meinander, and M. Leskelä. Atomic layer deposition of noble metals: Exploration of the low limit of the deposition temperature. *J Mater Res*, 19(11):3353–3358, 2004.

[75] W. M. M. Kessels, H. C. M. Knoops, S. A. F. Dielissen, A. J. M. Mackus, and M. C. M. van de Sanden. Surface reactions during atomic layer deposition of Pt derived from gas phase infrared spectroscopy. *Appl Phys Lett*, 95(1):013114, 2009.

[76] A. J. M. Mackus, N. Leick, L. Baker, and W. M. M. Kessels. Catalytic combustion and dehydrogenation reactions during atomic layer deposition of platinum. *Chem Mater*, 24(10):1752–1761, 2012.

[77] X. Jiang and S. F. Bent. Atomic layer deposition of platinum for solid oxide fuel cells. *ECS Trans*, 3(15):249–259, 2007.

[78] The International Centre for Diffraction Data (ICDD) PDF 00-001-11994. 2003.

[79] J. W. Elam, A. V. Zinovev, M. J. Pellin, D. J. Comstock, and M. C. Hersam. Nucleation and growth of noble metals on oxide surfaces using atomic layer deposition. *ECS Trans*, 3(15):271–278, 2007.

[80] S. Novak, B. Lee, X. Yang, and V. Misra. Platinum nanoparticles grown by atomic layer deposition for charge storage memory applications. *J Electrochem Soc*, 157 (6):H589–H592, 2010.

[81] The International Centre for Diffraction Data (ICDD) PDF 03-065-7645. 2003.

[82] W.-H. Kim, S.-J. Park, D. Y. Kim, and H. Kim. Atomic layer deposition of ruthenium and ruthenium-oxide thin films by using a Ru(EtCp)$_2$ precursor and oxygen gas. *J Korean Phys Soc*, 55(1):32–37, 2009.

[83] A.-C. Johansson, J. V. Larsen, M. A. Verheijen, K. B. Haugshøj, H. F. Clausen, W. M. M. Kessels, L. H. Christensen, and E. V. Thomsen. Electrocatalytic activity of atomic layer deposited Pt-Ru catalysts onto N-doped carbon nanotubes. *J Catal*, 311:481–486, 2014.

[84] L. F. Mabena, S. Sinha Ray, S. D. Mhlanga, and N. J. Coville. Nitrogen-doped carbon nanotubes as a metal catalyst support. *Appl Nanosci*, 1(2):67–77, 2011.

[85] T. Maiyalagan. Synthesis and electro-catalytic activity of methanol oxidation on nitrogen containing carbon nanotubes supported Pt electrodes. *Appl Catal B: Environ*, 80(3-4):286–295, 2008.

[86] R. Chetty, S. Kundu, W. Xia, M. Bron, W. Schuhmann, V. Chirila, W. Brandl, T. Reinecke, and M. Muhler. PtRu nanoparticles supported on nitrogen-doped multiwalled carbon nanotubes as catalyst for methanol electrooxidation. *Electrochim Acta*, 54(17):4208–4215, 2009.

[87] K. Gong, F. Du, Z. Xia, M. Durstock, and L. Dai. Nitrogen-doped carbon nanotube arrays with high electrocatalytic activity for oxygen reduction. *Science*, 323 (5915):760–764, 2009.

[88] M. S. Saha, R. Li, X. Sun, and S. Ye. 3-D composite electrodes for high performance PEM fuel cells composed of Pt supported on nitrogen-doped carbon nanotubes grown on carbon paper. *Electrochem Commun*, 11(2):438–441, 2009.

[89] Y. Chen, J. Wang, H. Liu, R. Li, X. Sun, S. Ye, and S. Knights. Enhanced stability of Pt electrocatalysts by nitrogen doping in CNTs for PEM fuel cells. *Electrochem Commun*, 11(10):2071–2076, 2009.

[90] Y. Chen, J. Wang, H. Liu, M. N. Banis, R. Li, X. Sun, T.-K. Sham, S. Ye, and S. Knights. Nitrogen doping effects on carbon nanotubes and the origin of the enhanced electrocatalytic activity of supported Pt for proton-exchange membrane fuel cells. *J Phys Chem C*, 115(9):3769–3776, 2011.

[91] D. Geng, H. Liu, Y. Chen, R. Li, X. Sun, S. Ye, and S. Knights. Non-noble metal oxygen reduction electrocatalysts based on carbon nanotubes with controlled nitrogen contents. *J Power Sources*, 196(4):1795–1801, 2011.

[92] M. Kumar and Y. Ando. Chemical vapor deposition of carbon nanotubes: A review on growth mechanism and mass production. *J Nanosci Nanotechnol*, 10 (6):3739–3758, 2010.

[93] C.-M. Seah, S.-P. Chai, and A. R. Mohamed. Synthesis of aligned carbon nanotubes. *Carbon*, 49(14):4613–4635, 2011.

[94] M. Terrones, A. Jorio, M. Endo, A. M. Rao, Y. A. Kim, T. Hayashi, H. Terrones, J.-C. Charlier, G. Dresselhaus, and M. S. Dresselhaus. New direction in nanotube science. *Mater Today*, 7(10):30–45, 2004.

[95] C. Liu, C.-C. Wang, C.-C. Kei, Y.-C. Hsueh, and T.-P. Perng. Atomic layer deposition of platinum nanoparticles on carbon nanotubes for application in proton-exchange membrane fuel cells. *Small*, 5(13):1535–1538, 2009.

[96] T. Shu, S.-J. Liao, C.-T. Hsieh, A. K. Roy, Y.-Y. Liu, D.-Y. Tzou, and W.-Y. Chen. Fabrication of platinum electrocatalysts on carbon nanotubes using atomic layer deposition for proton exchange membrane fuel cells. *Electrochim Acta*, 75: 101–107, 2012.

[97] Y.-C. Hsueh, C.-C. Wang, C.-C. Kei, Y.-H. Lin, C. Liu, and T.-P. Perng. Fabrication of catalyst by atomic layer deposition for high specific power density proton exchange membrane fuel cells. *J Catal*, 294:63–68, 2012.

[98] Y.-C. Hsueh, C.-C. Wang, C. Liu, C.-C. Kei, and T.-P. Perng. Deposition of platinum on oxygen plasma treated carbon nanotubes by atomic layer deposition. *Nanotechnol*, 23(40):405603, 2012.

[99] Y. Chen, J. Wang, X. Meng, Y. Zhong, R. Li, X. Sun, S. Ye, and S. Knights. Atomic layer deposition assisted Pt-SnO_2 hybrid catalysts on nitrogen-doped CNTs with enhanced electrocatalytic activities for low temperature fuel cells. *Int J Hydrogen Energy*, 36(17):11085–11092, 2011.

[100] R. G. Gordon, D. Hausmann, E. Kim, and J. Shepard. A kinetic model for step coverage by atomic layer deposition in narrow holes or trenches. *Adv Mater*, 15 (6):73–78, 2003.

[101] A. L. Patterson. Scherrer formula for X-ray particle size determination. *Phys Rev*, 56(10):978–982, 1939.

[102] J. I. Langford and A. J. C. Wilson. Scherrer after sixty years - Survey and some new results in determination of crystallite size. *J Appl Crystallogr*, 11:102–113, 1978.

[103] A. S. Aricò, P. Creti, H. Kim, R. Mantegna, N. Giordano, and V. Antonucci. Analysis of the electrochemical characteristics of a direct methanol fuel cell based on a Pt-Ru/C anode catalyst. *J Electrochem Soc*, 143(12):3950–3959, 1996.

[104] A. L. Ocampo, M. Miranda-Hernández, J. Morgado, J. A. Montoya, and P. J. Sebastian. Characterization and evaluation of Pt-Ru catalyst supported on multi-walled carbon nanotubes by electrochemical impedance. *J Power Sources*, 160(2): 915–924, 2006.

[105] M. S. Nashner, A. I. Frenkel, D. L. Adler, J. R. Shapley, and R. G. Nuzzo. Structural characterization of carbon-supported platinum-ruthenium nanoparticles from the molecular cluster precursor $PtRu_5C(CO)_{16}$. *J Am Chem Soc*, 119 (33):7760–7771, 1997.

[106] K. Kusada, H. Kobayashi, T. Yamamoto, S. Matsumura, N. Sumi, K. Sato, K. Nagaoka, Y. Kubota, and H. Kitagawa. Discovery of face-centered-cubic ruthenium nanoparticles: Facile size-controlled synthesis using the chemical reduction method. *J Am Chem Soc*, 135(15):5493–5496, 2013.

[107] Z. H. Zhou, W. S. Li, Z. Fu, and X. D. Xiang. Carbon nanotube-supported Pt-H_xMoO_3 as electrocatalyst for methanol oxidation. *Int J Hydrogen Energy*, 35(3): 936–941, 2010.

[108] P. Hernández-Fernández, M. Montiel, P. Ocón, J. L. G. de la Fuente, S. García-Rodríguez, S. Rojas, and J. L. G. Fierro. Functionalization of multi-walled carbon nanotubes and application as supports for electrocatalysts in proton-exchange membrane fuel cell. *Appl Catal B: Environ*, 99(1-2):343–352, 2010.

[109] J.-M. Léger. Mechanistic aspects of methanol oxidation on platinum-based electrocatalysts. *J Appl Electrochem*, 31(7):767–771, 2001.

[110] X. Zhao, M. Yin, L. Ma, L. Liang, C. Liu, J. Liao, T. Lu, and W. Xing. Recent advances in catalysts for direct methanol fuel cells. *Energy Environ Sci*, 4(8): 2736–2753, 2011.

[111] M. Watanabe and S. Motoo. Electrocatalysis by ad-atoms. 3. Enhancement of oxidation of carbon-monoxide on platinum by ruthenium ad-atoms. *J Electroanal Chem*, 60(3):275–283, 1975.

[112] F. Maillard, F. Gloaguen, and J.-M. Léger. Preparation of methanol oxidation electrocatalysts: Ruthenium deposition on carbon-supported platinum nanoparticles. *J Appl Electrochem*, 33(1):1–8, 2003.

[113] L. Dubau, F. Hahn, C. Coutanceau, J.-M. Léger, and C. Lamy. On the structure effects of bimetallic PtRu electrocatalysts towards methanol oxidation. *J Electroanal Chem*, 554-555:407–415, 2003.

[114] L. Vitos, A. V. Ruban, H. L. Skriver, and J. Kollár. The surface energy of metals. *Surf Sci*, 411:186–202, 1998.

[115] H. A. Gasteiger, N. Marković, P. N. Ross Jr., and E. J. Cairns. Electro-oxidation of small organic molecules on well-characterized Pt-Ru alloys. *Electrochim Acta*, 39(11-12):1825–1832, 1994.

[116] H. A. Gasteiger, N. Marković, P. N. Ross Jr., and E. J. Cairns. Methanol electrooxidation on well-characterized Pt-Ru alloys. *J Phys Chem*, 97(46):12020–12029, 1993.

[117] C. Lu, C. Rice, R. I. Masel, P. K. Babu, P. Waszczuk, H. S. Kim, E. Oldfield, and A. Wieckowski. UHV, electrochemical NMR, and electrochemical studies of platinum/ruthenium fuel cell catalysts. *J Phys Chem B*, 106(37):9581–9589, 2002.

[118] A.-C. Johansson, B. T. Dalslet, R. B. Yang, K. B. Haugshøj, M. J. G. Mølgaard, K. Christiansen, L. H. Christensen, and E. V. Thomsen. Electrocatalytic activity of Pt grown by ALD on carbon nanotubes for Si-based DMFC applications. *ECS Trans*, 50(13):117–125, 2012.

[119] G. Q. Lu, C. Y. Wang, T. J. Yen, and X. Zhang. Development and characterization of a silicon-based micro direct methanol fuel cell. *Electrochim Acta*, 49(5):821–828, 2004.

[120] S. Motokawa, M. Mohamedi, T. Momma, S. Shoji, and T. Osaka. MEMS-based design and fabrication of a new concept micro direct methanol fuel cell (μ-DMFC). *Electrochem Commun*, 6(6):562–565, 2004.

[121] T. Pichonat and B. Gauthier-Manuel. Recent developments in MEMS-based miniature fuel cells. *Microsyst Technol*, 13(11-12):1671–1678, 2007.

[122] S. K. Kamarudin, F. Achmad, and W. R. W. Daud. Overview on the application of direct methanol fuel cell (DMFC) for portable electronic devices. *Int J Hydrogen Energy*, 34(16):6902–6916, 2009.

[123] J. Yeom, G. Z. Mozsgai, B. R. Flachsbart, E. R. Choban, A. Asthana, M. A. Shannon, and P. J. A. Kenis. Microfabrication and characterization of a silicon-based millimeter scale, PEM fuel cell operating with hydrogen, methanol, or formic acid. *Sens Actuators B Chem*, 107(2):882–891, 2005.

[124] L. Xiaowei, S. Chunguang, Z. Yufeng, W. Wei, L. Xuebin, and T. Ding. Application of MEMS technology to micro direct methanol fuel cell. *Proc 1st IEEE Int Conf Nano/Micro Eng Mol Syst*, pages 699–702, 2006.

[125] Y. Zhang, J. Lu, H. Zhou, T Itoh, and R. Maeda. Application of nanoimprint technology in MEMS-based micro direct-methanol fuel cell (µ-DMFC). *J Microelectromech Syst*, 17(4):1020–1028, 2008.

[126] J. P. Esquivel, N. Sabaté, J. Santander, N. Torres, and C. Cané. Fabrication and characterization of a passive silicon-based direct methanol fuel cell. *Microsyst Technol*, 14(4-5):535–541, 2008.

[127] G. D'Arrigo, C Spinella, G Arena, and S. Lorenti. Fabrication of miniaturised Si-based electrocatalytic membranes. *Mater Sci Eng C*, C23(1-2):13–18, 2003.

[128] M. J. Riezenman. Mighty mites. *IEEE Spectr*, 40(6):30–33, 2003.

[129] L. Zhang, S.-R. Chae, Z. Hendren, J.-S. Park, and M. R. Wiesner. Recent advances in proton exchange membranes for fuel cell applications. *Chem Eng J*, 204-206: 87–97, 2012.

[130] S. Gold, K.-L. Chu, C. Lu, M. A. Shannon, and R. I. Masel. Acid loaded porous silicon as a proton exchange membrane for micro-fuel cells. *J Power Sources*, 135 (1-2):198–203, 2004.

[131] T. Pichonat, B. Gauthier-Manuel, and D. Hauden. A new proton-conducting porous silicon membrane for small fuel cells. *Chem Eng J*, 101(1-3):107–111, 2004.

[132] T. Pichonat and B. Gauthier-Manuel. A porous silicon-based ionomer-free membrane electrode assembly for miniature fuel cells. *Fuel Cells*, 6(5):323–325, 2006.

[133] M. Wang, X. Wang, S. Wu, Z. Tan, L. Liu, and X. Guo. Nano porous silicon membrane with channels for micro direct methanol fuel cells. *Proc 6th Int Conf Micro/Nano Eng Mol Syst*, pages 968–971, 2011.

[134] W. Li, X. Wang, Z. Chen, M. Waje, and Y. Yan. Carbon nanotube film by filtration as cathode catalyst support for proton-exchange membrane fuel cell. *Langmuir*, 21(21):9386–9389, 2005.

[135] J Wang, G. Yin, Y. Chen, R. Li, and X. Sun. Pd nanoparticles deposited on verti-cally aligned carbon nanotubes grown on carbon paper for formic acid oxidation. *Int J Hydrogen Energy*, 34(19):8270–8275, 2009.

[136] Z. Q. Tian, S. H. Lim, C. K. Poh, J. Lin, Z. Tang, D. Chua, Z. Xia, Z. Luo, Z. Shen, P. K. Shen, and Y. P. Feng. A highly order-structured membrane electrode assembly with vertically aligned carbon nanotubes for ultra-low Pt loading PEM fuel cells. *Adv Energy Mater*, 1(6):1205–1214, 2011.

[137] X. Li and P. W. Bohn. Metal-assisted chemical etching in HF/H_2O_2 produces porous silicon. *Appl Phys Lett*, 77(16):2572–2574, 2000.

[138] J. Teva, Z. J. Davis, and O. Hansen. Electroless porous silicon formation applied to fabrication of boron-silica-glass cantilevers. *J Micromech Microeng*, 20(1):015034, 2010.

[139] Z. Huang, N. Geyer, P. Werner, J. de Boor, and U. Gösele. Metal-assisted chemical etching of silicon: A review. *Adv Mater*, 23(2):285–308, 2011.

[140] M. K. Debe, A. K. Schmoeckel, G. D. Vernstrom, and R. Atanasoski. High voltage stability of nanostructured thin film catalysts for PEM fuel cells. *J Power Sources*, 161(2):1002–1011, 2006.

[141] D. van der Vliet, C. Wang, M. Debe, R. Atanasoski, N. M. Markovic, and V. R. Stamenkovic. Platinum-alloy nanostructured thin film catalysts for the oxygen reduction reaction. *Electrochim Acta*, 56(24):8695–8699, 2011.

[142] J. S. Spendelow and D. C. Papageorgopoulos. Progress in PEMFC MEA compo-nent R&D at the DOE fuel cell technologies program. *Fuel Cells*, 11(6):775–786, 2011.

[143] A. Samson, M. Søgaard, R. Knibbe, and N. Bonanos. High performance cathodes for solid oxide fuel cells prepared by infiltration of $La_{0.6}Sr_{0.4}CoO_{3-\delta}$ into Gd-doped ceria. *J Electrochem Soc*, 158(6):B650–B659, 2011.

Appendix A

List of Dissemination

Journal Publication List

I   A.-C. Johansson, B. T. Dalslet, R. B. Yang, K. B. Haugshøj, M. J. G. Mølgaard, K. Christiansen, L. H. Christensen, and E. V. Thomsen. Electrocatalytic activity of Pt grown by ALD on carbon nanotubes for Si-based DMFC Applications. *ECS Trans*, 50(13):117-125, 2012.

II J. H. Hales, C. Kallesøe, T. Lund-Olesen, A.-C. Johansson, H. C. Fanø, Y. Yu, P. B. Lund, A. L. Vig, O. Tynelius, and L. H. Christensen. Micro fuel cells power the hearing aids of the future. *Fuel Cells Bull*, 2012(12):12-16, 2012.

III A.-C. Johansson, R. B. Yang, K. B. Haugshøj, J. V. Larsen, L. H. Christensen, and E. V. Thomsen, Ru-decorated Pt nanoparticles on N-doped multi-walled carbon nanotubes by atomic layer deposition for direct methanol fuel cells. *Int J Hydrogen Energy*, 38(26):11406-11414, 2013.

IV A.-C. Johansson, J. V. Larsen, M. A. Verheijen, K. B. Haugshøj, H. F. Clausen, W. M. M. Kessels, L. H. Christensen, and E. V. Thomsen, Electrocatalytic activity of atomic layer deposited Pt-Ru catalysts onto N-doped carbon nanotubes. *Journal of Catalysis*, 311:481-386, 2014.

V   J. V. Larsen, B. T. Dalslet, A.-C. Johansson, C. Kallesøe, and E. V. Thomsen, Micro direct methanol fuel cell with perforated silicon-plate integrated ionomer membrane. *J Power Sources*, 257:237-245, 2014.

List of Presentations

- <u>A.-C. Johansson</u>, R. B. Yang, K. B. Haugshøj, C. Kallesøe, E. V. Thomsen, and L. H. Christensen. Atomic layer deposition of Pt for micro direct methanol fuel cells, 1st ENHANCE Winter School at Ruhr university Bochum, Jan 25-28, 2011, *poster presentation.*

- <u>A.-C. Johansson</u>, R. B. Yang, L. M. Borregaard, B. T. Dalslet, J. V. Larsen, E. V. Thomsen, and L. H. Christensen. Atomic layer deposition of noble metals for micro direct methanol fuel cell. 3rd German-French Summer School on Electrochemistry & Nanotechnology, Porquerolles, France, Sep 18-23, 2011, *poster presentation.*

- <u>A.-C. Johansson</u>, R. B. Yang, K. Haume, L. M. Borregaard, B. T. Dalslet, E. V. Thomsen, and L. H. Christensen. Application of ALD for silicon-based micro direct methanol fuel cells. 2nd ENHANCE Winter School at University of Helsinki, Finland, Jan 9-12, 2012, *oral presentation.*

- <u>A.-C. Johansson</u>, B. T. Dalslet, R. B. Yang, K. B. Haugshøj, M. J. G. Mølgaard, K. Christiansen, L. H. Christensen, and E. V. Thomsen. Electrocatalytic activity of Pt grown by ALD on carbon nanotubes for Si-based DMFC applications. PRiME 2012, Honolulu, USA, Oct 7-12, 2012, *oral presentation.*

List of Activities Within the ENHANCE Project

Winter Schools

Winter school consisted of two days of conferences and two days of soft-skill training about oral presentation, scientific writing, patents, job applications, CV, job interviews etc. and company visits.

- Ruhr University of Bochum, Jan 25-28, 2011.

- University of Helsinki, Jan 9-12, 2012.

- Eindhoven University of Technology, Jan 14-17, 2013.

Workshops

Workshop was four-five days with lectures, experiments, tours and visits in specific topics.

- Principles and theory of crystallography, NMR and thermal analysis. Ruhr University Bochum, Aug 30 - Sep 3, 2010.

- Characterization of thin films by X-ray scattering methods, ion beams and electron diffraction. University of Helsinki, Apr 4-8, 2011.

- Leading technologies for gas phase deposition of materials for compound, silicon and organic semiconductor device applications. AIXTRON, May 21-25, 2011.

- In-situ and real-time thin film and process diagnostics. Eindhoven University of Technology, Nov 21-25, 2011.

- Introduction to surface analysis techniques (TOF-SIMS, XPS, TEM, FIB-SEM), innovation strategy and lab visits in the Copenhagen area. Danish Technological Institute, Mar 26-30, 2012.